

Alma Mater Studiorum - Università di Bologna

DOTTORATO DI RICERCA IN
INGEGNERIA CIVILE, CHIMICA, AMBIENTALE E DEI MATERIALI

Ciclo 35

Settore Concorsuale: 08/A4 - GEOMATICA

Settore Scientifico Disciplinare: ICAR/06 - TOPOGRAFIA E CARTOGRAFIA

CROSS-SENSORS ANALYSIS OF MULTISPECTRAL EARTH OBSERVATION
DATA FOR ENVIRONMENTAL MONITORING

Presentata da: Francesca Trevisiol

Coordinatore Dottorato

Alessandro Tugnoli

Supervisore

Gabriele Bitelli

Co-supervisore

Emanuele Mandanici

Esame finale anno 2023

Declaration

I hereby declare that, the contents and organization of this dissertation constitute my own original work and does not compromise in any way the rights of third parties, including those relating to the security of personal data.

Francesca Trevisiol

2023

Contents

- 1. Multispectral satellite missions 11
 - 1.1. Landsat program 11
 - 1.1.1. Landsat-5 15
 - 1.1.2. Landsat-7 17
 - 1.1.3. Landsat-8 19
 - 1.1.4. Landsat-9 21
 - 1.2. Copernicus programme and its space component 22
 - 1.1.1. Sentinel-2 25
- 2. Data products..... 31
 - 2.1. Landsat collections and products..... 31
 - 2.2. Sentinel-2 products..... 39
- 3. New approaches in EO data analysis 45
 - 3.1. Change Detection Analysis traditional approaches and new perspectives... 46
 - 3.1.1. Open-access policy and cloud-based platforms 48
 - 3.2. Time series analysis and data harmonization 51
- 4. Cross-sensors comparison of popular vegetation indexes from Landsat TM, ETM+, OLI and Sentinel MSI for time series analysis..... 56
 - 4.1. Materials..... 57
 - 4.1.1. Landsat..... 57
 - 4.1.2. Sentinel-2 59
 - 4.1.3. Vegetation Indices 61

4.2.	Methodology	62
4.2.1.	Study area.....	63
4.2.2.	Data gathering	63
4.2.3.	Pixel masking.....	66
4.2.4.	Image coupling, co-registration and reprojection	66
4.2.5.	Sampling.....	67
4.2.6.	Cross-sensors analysis	68
4.3.	Results	70
4.3.1.	OLI and MSI.....	70
4.3.2.	ETM+ and MSI	72
4.3.3.	ETM+ and OLI	74
4.3.4.	TM and ETM+	77
4.3.5.	Time.....	79
4.4.	Discussion	80
5.	Preliminary assessment on Landsat-9 for a combined use	83
5.1.	Local comparison with in-field survey.....	84
5.1.1.	Survey design.....	84
5.1.2.	Spectroradiometer Survey.....	88
5.1.3.	Spectral signature processing	90
5.1.4.	Image-to-image preliminary assessment	91
5.2.	Cross-sensors comparison at continent level.....	92
5.2.1.	Materials	92
5.2.2.	Methodology	95
5.3.	Example of the impact of harmonization on time series analysis	99

5.4. Results	100
5.4.1. <i>In situ</i> survey and local analysis.....	100
5.4.2. European cross-sensors comparison	105
5.4.3. Harmonization example on selected sample	116
Conclusion.....	121
Bibliography.....	127

Introduction

Landsat and Sentinel-2 missions offer a unique and continuously updated archive of multispectral images capturing Earth's surface processes over time, ensuring global coverage and medium-to-high revisit time. On the one hand, Landsat mission, which has been capturing multispectral and thermal images from the 70s, represents a unique archive of information. On the other hand, the Copernicus Sentinel-2 mission, consisting of two satellites and collecting from June 2015 multispectral data with medium resolution, has been providing an unprecedented acquisition frequency.

The open access policy of both the missions, together with their effort in producing easy to use products supported by cloud computing platforms, such as Google Earth Engine, played a key role in broadening the exploitation of moderate resolution multispectral data and triggering technological advancements. Traditional change detection techniques have been progressively replaced by the now possible analysis of dense time series of remotely sensed images, especially for environmental monitoring applications, such as vegetation analyses.

Indeed, phenomena can be better identified when seen as sequence of different states over time, rather than considering few single states, helping deepen the knowledge of surface processes and changes; not only drastic changes but, more importantly, slight modification through time. This second case is particularly important when the purpose of the study is the monitoring of effects to land surface by climate drivers acting slowly.

This approach in vegetation monitoring related studies is well-documented. Furthermore, vegetation indexes, such as NDVI, are often used for their simplicity in summarizing and highlighting the information contained in the original multispectral datasets. However, while the observations frequency is crucial in an efficient time series analysis, cloud coverage might highly affect passive sensors acquisition, resulting in gaps in information in the Time Series. For this reason, the integration and harmonization of different sensors play a crucial role to minimize these possible gaps. The harmonization can be based on statistics on the images themselves, but can also be assisted by ground measurements of surface reflectance, to ensure sufficient and comparable quality among the different instruments.

Therefore, the present study addresses the issues related to the integration of different data sources for the analysis of long and dense time-series of multispectral images as well as their derived indexes. The possibility of using together Landsat and Sentinel-2 missions has been investigated through cross-sensors comparisons, performed on a huge amount of data to ensure statistical significance. For this purpose, dedicated procedures have been coded and implemented in Google Earth Engine.

Moreover, considering the ongoing Landsat and Sentinel-2 satellites, the analysis was supported with in situ spectroradiometer measurements, which can provide also an assessment of the recently launched Landsat-9 for a combined use.

The research is presented as follows.

Chapter 1 introduces the Landsat and Copernicus programs, their founding ideas and their programmatic development. The main characteristics

of satellites and sensors of Landsat-5, Landsat-7, Landsat-8, Landsat-9 and Sentinel-2 is given.

In Chapter 2 are presented the products available for every mission, in particular differences in the generation of Bottom of Atmosphere (BOA) datasets are provided.

Chapter 3 gives an overview on the novelties in the EO sector that led to the spread of time series analysis application using Landsat and Sentinel and presents the harmonization issues.

In Chapter 4 is presented the study conducted to harmonize Landsat and Sentinel Missions (TM, ETM, OLI and MSI) derived popular vegetation indexes (NDVI, EVI, SAVI and NDMI) for environmental monitoring applications. An assessment of the computed calibration coefficients that can be used to minimize differences in the combined use is given.

Finally, Chapter 5 provides a preliminary assessment of the Landsat-9 mission for a combined use with Landsat-8 and Sentinel-2, based on cross-sensor comparison of their common spectral bands. This analysis was supported by *in situ* measurements with a spectroradiometer.

Chapter 1

1. Multispectral satellite missions

The following chapter gives an overview of the two major international Earth Observation (EO) programs, Landsat and Copernicus. The programs' objectives, foundational ideas and programmatic developments, and their multispectral missions specifications are presented hereinafter. The basic concept of multispectral remote sensing and digital image processing are taken for granted and here omitted for the sake of brevity, nevertheless, these notions can be found in (Camps-Valls et al., 2012; Elmoataz et al., 2008; Richards, 2022).

1.1. Landsat program

The Landsat program is a series of EO satellites equipped with multispectral instruments, launched by the United State (U.S.) which provide the longest continuous archive of the Earth's surface (Teixeira Pinto et al., 2020).

In the late 1960s, the U.S. government set up the framework for the longest-running and first medium-resolution Earth observation mission (Lauer et al., 1997). By that time, scientific and technological efforts were intensively involved in space exploration, to pursue greatest achievements such as the

human land on the Moon. In this context, the potential for space-based observation of the Earth was emerging and appeared promising as well as more and more possible from a technological point of view. Moreover, at that time there was a convergence of needs of the scientific community, private sector and state administration led to the establishment of the Landsat program, the first international Earth Observation program. Among the different driving forces, the most impelling included the need for better information about the Earth's features, the national security concerns and new business opportunities (Lauer et al., 1997).

Firstly, the need to gather information about resources available on the globe to sustain the growing world population had already become clear. By that time the debate on sustainable development, sustainable management of renewable and not renewable resources was already open and felt to be vital (Simonett, 1969). It was recognized that only an improved understanding of the Earth's resources, processes and their geographic distribution would allow to take conscious action for wiser resources management. In this context, capturing images of the Earth from space was identified as the technology that would make it possible to collect information on Land and Water, with a certain frequency, ensuring local to global coverage.

Secondly, the opportunity to acquire images of portions of the Earth from cameras on board aircraft or satellites had already been experienced from the government for national security purposes during the Cold War, starting from the 1950s. Indeed, the successfully experience with reconnaissance systems, such as the aerial photographic mission U2 (Hammer and Ur, 2019) and the CORONA and ARGON imaging satellites (Casana and Cothren, 2013; McDonald, 1995), which provided the US government with valuable

information since 1956, has demonstrated the effectiveness of this technology for the security purpose. Hence, at that time the desire for new technological investments in the EO market for intelligence objectives. Moreover, private-sector investors started to see a commercial opportunity in the satellite remote sensing potential to provide a new insight on the Earth resources, opening up the EO market to industries.

In addition, international cooperation contributed to the launch of the Landsat programme: since that time there was the understanding that promoting of cooperation between national space agencies would lead to cost savings by sharing resources, facility and knowledge (The White House - National Science and Technology Council, 1996).

Driven by these forces, the Landsat Program officially started in 1967 from a partnership between the National Aeronautics and Space Administration (NASA), accounting the satellite construction and their launches, and U.S. Geological Survey (USGS) which manages the archive and distribution of data.

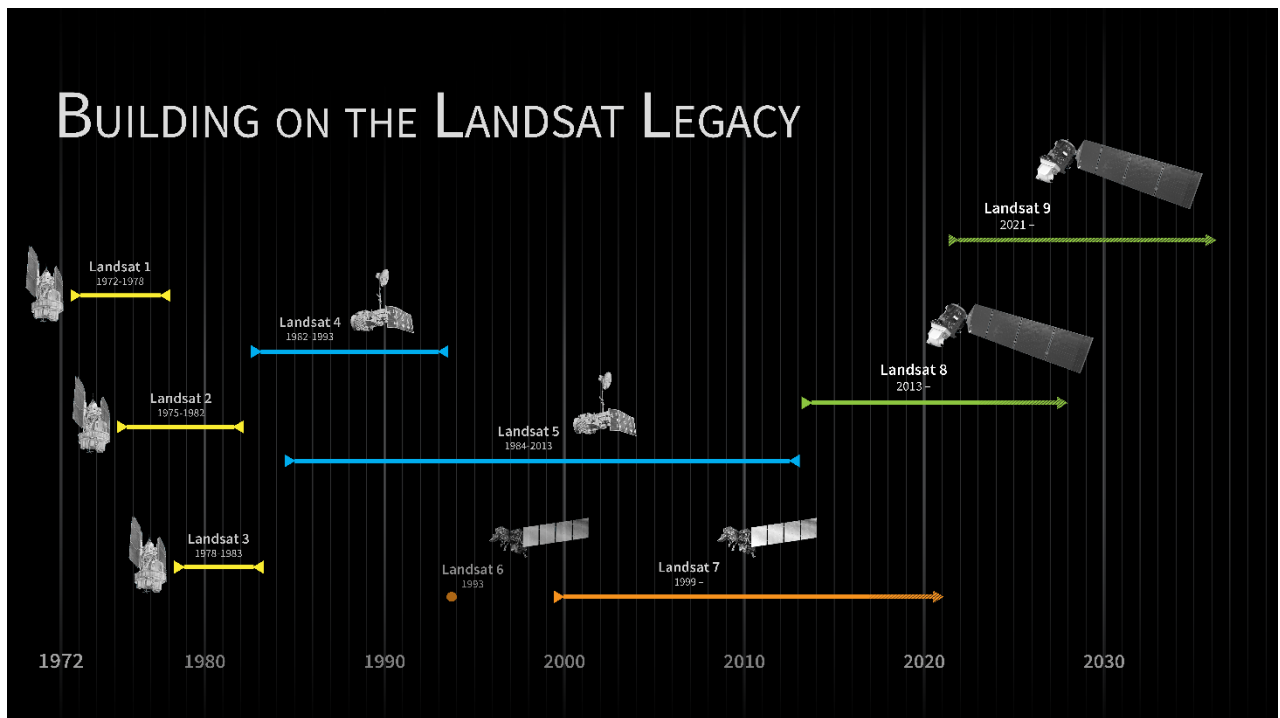


Figure 1 Landsat satellites timeline. Credits: NASA's Scientific Visualization Studio.

The first satellite of the Landsat family, the Landsat-1 (former Earth Resources Technology Satellite - ERTS-1), was launched in July 1972 starting a half-century legacy in data gathering and continuity (Kondratyev et al., 1971; Wulder et al., 2022). Indeed, the programmatic development of Landsat mission focuses on the continuity of the programme by providing high quality data without interruptions, thanks to a continuous turnover and update of satellites. The key parameter defining the Landsat missions and shared by all its satellites are the medium spatial resolution, the temporal and spectral coverage. The design of the missions was devoted to ensure global monitoring capacity, since the very beginning with Landsat-1. Figure 1 gives an overview on the timeline of the Landsat satellites showing their time-span operation from the launch of the first satellite, the Landsat-1 to the latest Landsat-9, providing an insight of these data availability. Every mission has a repeat cycle of 16 days on every point on Earth, and every new Landsat satellite has been designed to create a

pair constellation with the previous one still operating, resulting in an 8-day revisit coverage.

Despite the initial decade characterized by uncertainty (Waldrop, 1982), the program was able to keep improving itself and it has been devoted to meet the user needs, being a pioneer in many decisions about the program, for example in the data open access policy (Woodcock et al., 2008). The other Landsat key elements, the programmatic developments and the data products will be further discussed in Chapter 2.

In the following sections a description of the Landsat-5 to the newest Landsat-9 missions and data characteristics is given. The details of the first satellites of the program are here omitted (Landsat-1 – Landsat-4) because their instruments do not meet the spatial (80m/px) and spectral characteristics of the sensors used in the cross-sensors comparison performed to harmonize different instruments that is presented in Chapter 4 and 5 (Lauer et al., 1997).

1.1.1. Landsat-5

After its launch on the 1st March 1984, Landsat-5 was operated by USGS until January 2013. For more than 29 years it acquired over 2.5 million images of the Earth, exceeding its original three-year designed life. Being the longest running satellite made it earn a Guinness World Record: Landsat-5 represents the longest single satellite sensor archive of the Earth surface (Loveland and Dwyer, 2012; Roy et al., 2020).

The satellite was launched at 705 km of nominal altitude into a sun-synchronous polar orbit at with an inclination of 98.2 degrees. It completed every 99 minutes a circle around the Earth, resulting in a 14 orbit cycles in a day. The revisit time of Landsat-5 is 16 days, with a 9:45 a.m. mean sunlit equatorial

north to south crossing time. Despite the original plan, due to temporally sparse station keeping maneuvers, the satellite's orbit changed during the almost 30 years of life of the satellite, consequentially different overpass time up to 0.92 hours were registered, resulting in changes in the solar geometry at the time of Landsat acquisition (Johnson and Hassett, 1984; Roy et al., 2020; Zhang and Roy, 2016).

The satellite is equipped with two different sensors: the Multi Spectral Scanner (MSS), which was the camera onboard the Landsat satellite since Landsat-1, and the innovative Thematic Mapper (TM).

The Thematic Mapper sensor is a multispectral camera that captures the Earth surface spectral reflectance between 0.45 μm and 12.5 μm in seven different bands. In particular, Blue, Green, Red, NIR, SWIR-1 and SWIR-2 spectral bands (bands 1-5 and 7) have an Instantaneous Field Of View (IFOV) of 30m x 30m, and the thermal band (Band 6) is provided with 120m spatial resolution (IFOV of 120m x 120m) (Chander et al., 2007). In Table characteristics of TM spectral bands can be found. TM sensor failed in November 2011.

Band		Wavelength	Spatial resolution
Band 1	Blue	0.45-0.52 μm	30 m
Band 2	Green	0.52-0.60 μm	30 m
Band 3	Red	0.63-0.69 μm	30 m
Band 4	NIR	0.76-0.90 μm	30 m
Band 5	SWIR-1	1.55-1.75 μm	30 m
Band 6	TIR	10.41-12.5 μm	120 m
Band 7	SWIR-2	2.08-2.35 μm	30 m

Table 1. Spectral bands characteristics of Landsat-5 TM

1.1.2. Landsat-7

The next satellite in the series was supposed to be Landsat-6. It was designed and built to have a 15-meter panchromatic band and an Enhanced Thematic Mapper (ETM) sensor on board, the technological evolution of the L5 TM. Unfortunately, Landsat-6 was lost after its launch in 1993, failing to reach its designated orbit (Lauer et al., 1997; National Oceanic and Atmospheric Administration (NOAA), 1995a, 1995b).

Conversely, the Landsat-7 mission was launched on the 15th of April 1999 and successfully reached its orbit at a nominal altitude of 705 km (Figure 2). The satellite overpasses the equator at 10:00 a.m. (+/- 15 minutes) from north to south on the descending orbital node. As the Landsat-5 TM, the Landsat-7 ensures a revisit time of 16 days.

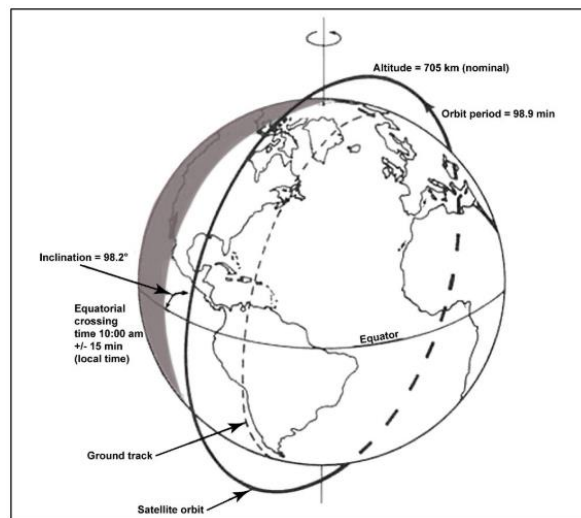


Figure 2 Landsat-7 orbit schema (U.S. Geological Survey, 2019a)

The satellite was equipped with an Enhanced Thematic Mapper + (ETM+) instrument. The design of the ETM+ introduces some technological advancement with respect to the TM sensor. A new panchromatic band with a spatial resolution of 15 (Band 8) was added. Moreover, the spatial resolution of

the thermal-IR band was improved, providing images at 60 m/px. In addition, two full-aperture calibration panels were added allowing better absolute radiometric calibration (U.S. Geological Survey, 2019a). Table provides an overview of the spectral characteristics of the ETM+ sensor.

Band		Wavelength	Spatial resolution
Band 1	Blue	0.45 - 0.52 μm	30 m
Band 2	Green	0.52 - 0.60 μm	30 m
Band 3	Red	0.63-0.69 μm	30 m
Band 4	NIR	0.77-0.90 μm	30 m
Band 5	SWIR-1	1.55-1.75 μm	30 m
Band 6	TIR	10.40-12.50 μm	60 m
Band 7	SWIR-2	2.08-2.35 μm	30 m
Band 8	Panchromatic	0.52 - 0.90 μm	15 m

Table 2 Spectral bands characteristics of Landsat-7 ETM+.

Unfortunately, some issues were experienced during Landsat-7 operational life. Beside the lately satellite orbit drifting started after August 2017, causing an earlier local acquisition time (Qiu et al., 2021), the biggest impact affecting the mission was caused by the failure of the Scan Line Corrector (SLC) on May 31, 2003. The SCL is an electro-optical mechanism which compensates for the along-track motion of the satellite that occurs when it is scanning across-track. As a result of this failure, the sensor line of sight traces a zig-zag pattern along the satellite ground track, as can be seen in Figure 3. As a consequence, from June 2003, when the Scan Line Corrector (SCL) failed, Landsat-7 images have been acquired and delivered with gaps, producing a loss of information up to the 22% (Andréfouët et al., 2003). The decommissioning of Landsat 7 began in mid-2021, leaving its orbit to the new Landsat-9.

Landsat 7 products are delivered as 8-bit images with 256 grey levels.

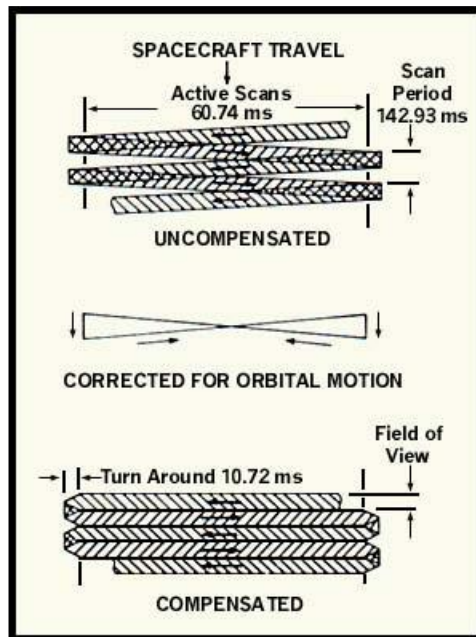


Figure 3 ETM+ SLC Effect (U.S. Geological Survey, 2019a)

1.1.3. Landsat-8

Landsat-8 satellite, originally known as the Landsat Data Continuity Mission (LDCM), was launched on February 11, 2013. It operates in a 705 km near-polar, sun-synchronous orbit, crossing the equator on the descending node at 10:00 (± 15 minutes) a.m. Mean Local Time (MLT). It ensures a 16-day ground track repeat cycle. Completing a single Earth orbit every 98.9 minutes, Landsat-8 has been acquiring more data than ever before, with an imaging capacity about 725 images per day (Loveland and Irons, 2016). Indeed, while maintaining the consistency requirement with previous series missions, Landsat-8 represents the greatest technological improvement over its predecessors in terms of image acquisition capability, radiometric and geometric data quality (Irons et al., 2012; Roy et al., 2014).

It is equipped with two different sensors: the Operational Land Imager (OLI) and the Thermal Infrared Sensor (TIRS). For the purposes of the study, only the OLI instrument is here considered and described. OLI measures the

visible, NIR and SWIR part of the electromagnetic spectrum, while TIRS operates in the thermal region, allowing to study the land surface temperature. Following the spectral improvements achieved with ETM+ instrument, OLI sensor was designed with a panchromatic 15m band (Band 9) and eight 30 m spectral bands. In OLI the new ultra-blue band (Band 1) and the Band 9 (1.36 - 1.38 μm) are introduced for the purposes of coastal/aerosol studies and cirrus cloud detection respectively (U.S. Geological Survey, 2019b). Spectral bands details are reported in Table .

Band		Wavelength	Spatial resolution
Band 1	Coastal Aerosol	0.43 - 0.45 μm	30 m
Band 2	Blue	0.45 - 0.51 μm	30 m
Band 3	Green	0.53 - 0.59 μm	30 m
Band 4	Red	0.64 - 0.67 μm	30 m
Band 5	NIR	0.85 - 0.88 μm	30 m
Band 6	SWIR-1	1.57 - 1.65 μm	30 m
Band 7	SWIR-2	2.11 – 2.29 μm	30 m
Band 8	Panchromatic	0.50 – 0.68 μm	15 m
Band 9	Cirrus	1.36 - 1.38 μm	30 m
Band 10	TIRS 1	10.6 - 11.19 μm	
Band 11	TIRS 2	11.5 - 12.51 μm	

Table 3 Spectral bands characteristics of Landsat-8 OLI/TIRS

Beside the addition of two spectral bands, the designers of the OLI were able to reduce the Signal to Noise Ratio (Barsi et al., 2014). Moreover, data are stored with a 12-bit quantization, which improves once again the radiometric precision, open up to a maximum range of 4096 grey levels. Previous Landsat data were delivered as 8-bit digital image, allowing only 256 grey levels. The enhancement of SNR, the increased quantization, together with the new coastal and cirrus bands, made Landsat-8 valuable for new applications, increasing its

ability in land and water characterization (Lymburner et al., 2016; Schott et al., 2016). Finally, the geometric and geodetic accuracy was estimated to be around 11.4 m, when referenced to ground control points, and ~37 m in absolute geodetic accuracy.

1.1.4. Landsat-9

Landsat-9, the latest satellite of the series, was launched on September 27, 2021. It took the Landsat-7 orbit, the near-polar, sun-synchronous orbit at a nominal altitude of 705 km. It completes an orbit cycle around the globe every 98.9 minutes, with an MLT equatorial crossing of the descending node at 10:00 a.m. (+15 minutes). As the previous satellites, it has a revisit time of 16 days (U.S. Geological Survey, 2022a).

Landsat-9 is equipped with an Operational Land Imager 2 (OLI-2) instrument, which is nearly identical to the Landsat-8 OLI still operating. As OLI, OLI-2 captures images through nine channels in the solar reflective part of the spectrum (0.43–2.29 μm) at 30 m resolution, except for the panchromatic band which is delivered within 15m/px (Markham et al., 2019). The spectral band specifics can be found in OLI table previously presented (Table 3). Overall, the most significant difference between OLI and OLI-2 regards their quantization: the data captured by OLI-2, indeed, are stored as 14 bits digital images, which represents an improvement respects the 12-bits OLI products (Gross et al., 2022; Masek et al., 2020).

In summary, the presented Landsat satellites, one after the other, acquiring digital images in the multispectral domain since 1984, provide a unique and continuous record of land and water surfaces of the globe. On the similarity of the multispectral instruments just described lays the chance of having consistency through data acquired by different sensors over different

periods. In Figure 4 a visual summary of spectral bands resemblance can be found. The main threats to the consistency of the archive are the orbit drifting of Landsat-5 and Landsat-7 together with the loss of information due to the SLC failure in Landsat-7 ETM+.

All the Landsat family satellites, sharing the presented characteristics, were designed and have demonstrated to provide valuable data for a wide range of applications, including land use and land cover mapping, natural resource management, urban and regional planning, and disaster response.

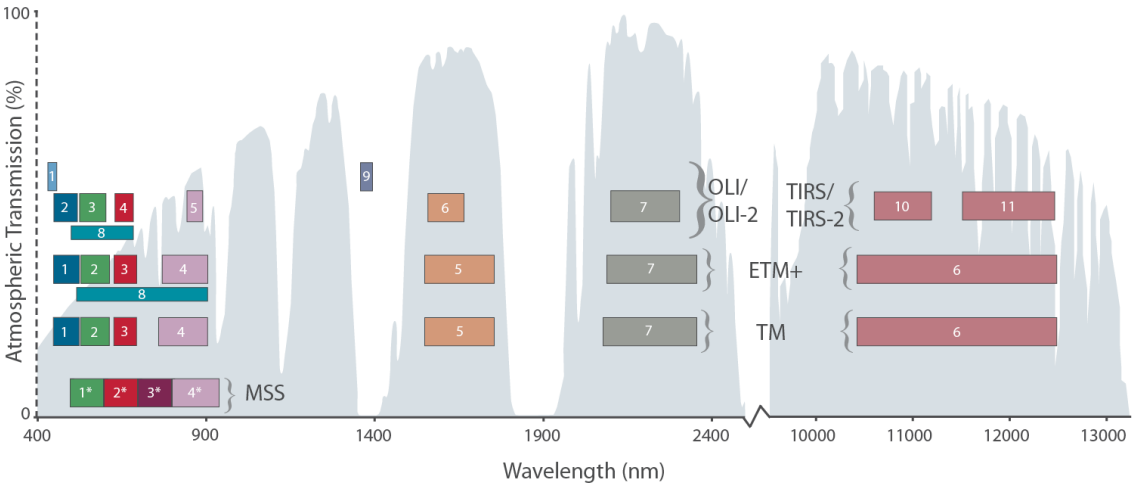


Figure 4 Comparison of the spectral bands of Landsat-1 to Landsat-9 missions. Source (NASA, 2023)

1.2.Copernicus programme and its space component

At the end of the XX century, the need of gathering information to support environmental, climate and security policies became a pan-European challenge (Aschbacher and Milagro-Pérez, 2012a). With this purpose, the Global Monitoring for Environment and Security (GMES) initiative was started in 1998, when the European Commission (EC), the European Organisation for the Exploitation of Meteorological Satellites (EUMETSAT), the European Space

Agency (ESA) and the main national space agencies of Member states signed the Baveno Manifesto. At that time, GMES was considered as the most ambitious operational Earth Observation programme, promoting a communitarian space-based environmental monitoring (Aschbacher and Milagro-Pérez, 2012b). In 2014 the EC established the Copernicus programme which formerly inherited all the activities achieved under the GMES initiative (Koch, 2015; The European parliament and The European council, 2014).

Copernicus is defined in the Regulation (EU) 2021/696 as an “operational, autonomous, user-driven, civil Earth observation system under civil control, building on the existing national and European capacities, offering geo-information data and services, comprising satellites, ground infrastructure, data and information processing facilities, and distribution infrastructure, based on a free, full and open data policy and, where appropriate, integrating the needs and requirements of security” (The European parliament and The European council, 2021).

The main objectives of the Copernicus program can be summarized as follows:

- a) gathering information of Earth system and keeping track of its resources to support environmental protection and sustainable management;
- b) providing information for European citizens’ security and emergency response through EO;
- c) maximizing socio-economic benefits of EO and supporting a sustainable development by promoting the use of the program data and derived services;
- d) promoting the development of the European space industries;

In order to achieve these objectives, Copernicus was organized into three different components: service, space and *in situ* components. The service component delivers ready to use/high added value information useful for application in the following areas: atmosphere monitoring, marine environment monitoring, land monitoring, climate change, emergency management and security. The space component is in charge to ensure sustainable spaceborne observations, vital for the service areas just mentioned. Finally, the *in situ* component with its airborne, seaborne and ground-based networks coordinates product validation as well as data access and supports the services (Jutz, 2015; Jutz and Milagro-Pérez, 2018).

The space component of the Copernicus Program, managed by ESA, includes a series of satellite missions, the Sentinels, specifically designed to pursue the program purposes. The space component also includes the missions from other space agencies, called Contributing Missions (Jutz and Milagro-Pérez, 2016). The Sentinels were created to ensure long-term performance, and the missions development was conducted according to user requirements, driving scientific and technological development to fill their needs. In particular, each mission was specifically designed to address a different application area, among Atmospheric, Oceanic, and Land monitoring. For this purpose, a specific instrument has been designed for each mission to provide data suitable for the target application. Indeed, the Sentinels provide several instruments observations in different spectral bands and spatial resolutions, with global coverage and high revisit times, addressing specific applications (Berger et al., 2012). The Sentinel missions consist of (CSC Mission Management Team, 2018; Jutz and Milagro-Pérez, 2016) (Figure 5):

- Sentinel-1: Moderate-resolution radar imaging;

- Sentinel-2: Moderate-resolution multispectral imaging;
- Sentinel-3: Medium-resolution multispectral imaging and altimetry;
- Sentinel-4: Atmospheric composition monitoring from geostationary orbit;
- Sentinel-5, and Sentinel-5 Precursor: Atmospheric composition monitoring from low- Earth orbit;
- Sentinel-6 (Jason-CS): High precision radar altimeter mission.



Figure 5 Copernicus satellite missions

Among the Sentinel family constellations, for the purpose of the study here is described only the Sentinel-2 mission, the Copernicus wide-swath, medium-resolution, multi-spectral imaging mission (ESA, 2015).

1.1.1. Sentinel-2

Sentinel-2 mission is a twin polar-orbiting satellite phased at 180° to each other: Sentinel-2A and Sentinel-2B (ESA, 2015). Sentinel-2A was launched in 2015, while Sentinel-2B was launched two years later in 2017. They are supposed to have a minimum lifetime of 7.25 years and they were provided with 12 years of consumables. To ensure long-term service, Sentinel-2C and D are under development (Toulemont et al., 2021).

After their launch, Sentinel-2A/B reached their orbit at an altitude of 786 km, angled of 98.62°, and acquire images over land and coastal areas with a 290 km width swath, covering the Earth surface between the latitudes 56° South and 83° North. Their orbit crosses the equator at 10:30 a.m. Mean Local Solar Time (MLST) at the descending node (ESA, 2015). The revisit frequency of each single satellite is 10 days, when considering the constellation 5 days revisit time is ensured. Moreover, the swath overlap between adjacent orbits increases even more the revisit frequency (Li and Roy, 2017).

The two satellites are equipped with the Multi-Spectral Instrument (MSI), a sensor that measures the Earth's reflected radiance in 13 spectral bands, in the visible, near-infrared and shortwave infrared regions of the electromagnetic spectrum, providing imagery at different spatial resolution, ranging between 10 m and 60 m (Drusch et al., 2012). Spectral and geometric resolution details can be found in Table 4.

Sentinel-2 MSI		
Bands	Wavelength (µm)	Resolution
B1 Coastal aerosol	0.433 – 0.453	60 m
B2 Blue	0.458 – 0.523	10 m
B3 Green	0.543 – 0.578	10 m
B4 Red	0.650 – 0.680	10 m
B5 Red Edge 1	0.698 – 0.713	20 m
B6 Red Edge 2	0.733 – 0.748	20 m
B7 Red Edge 3	0.773 – 0.793	20 m
B8 NIR	0.785 – 0.900	10 m
B8a NIRn	0.855 – 0.875	20 m
B9 Water Vapour	0.935 – 0.955	60 m

B10 Cirrus	1.360 – 1.390	60 m
B11 SWIR	1.565 – 1.655	20 m
B12 SWIR	2.100 – 2.280	20 m

Table 4. Spectral bands characteristics of Sentinel-2 MSI

The paired Sentinel-2 MSIs have been designed to provide continuity with Landsat-like heritage and ongoing missions. Indeed, Landsat instruments wavelengths basically defined the core of the new multispectral Copernicus sensors. Indeed, the MSI keeps a NIR band (10 m Band 8, 0.78 – 0.90 μm) similar to these of the Landsat TM and ETM+ instruments (30 m Band 4, 0.77 - 0.90 μm). However, the NIR band provided by TM and ETM+ was affected by the presence of water vapour (Li et al., 2017). Therefore, a NIR narrow band (20m B8A, 0.855 – 0.875 μm) was added, similar to the improved NIR band of the OLI sensor, as highlighted in (Mandanici and Bitelli, 2016) (Figure 6). Moreover, following the OLI improvements, S2 sensor also provide a Coastal aerosol (0.433 – 0.453 μm) and a Water vapour (0.935 – 0.955 μm) bands for atmospheric correction and cloud detection at a resolution of 60 m.

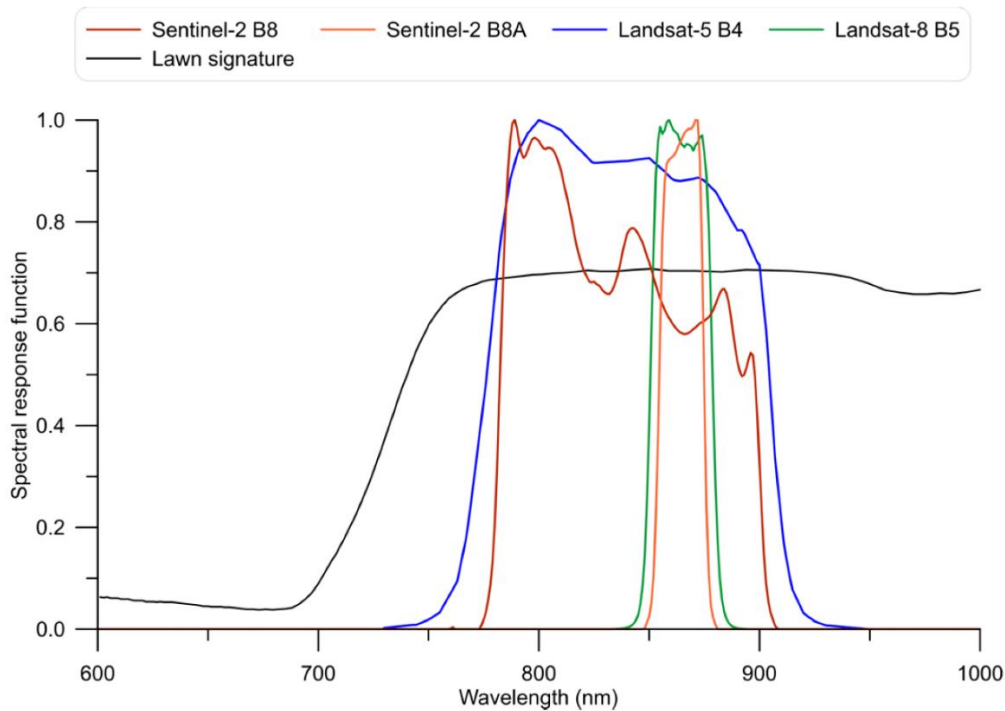


Figure 6. Comparison of the spectral response functions in the NIR bands of the Sentinel-2 MSI, Landsat-5 TM and Landsat-8 OLI. Source: (Mandanici and Bitelli, 2016)

Beside these data continuity, the S2 introduces some innovations, especially with the new 20m narrow bands in the Red-edge part of the electromagnetic spectrum, which results in a great impact in vegetation monitoring (Delegido et al., 2011).

The MSI instruments acquire and store information as a 12-bit digital image, allowing a radiometric resolution per pixel in the range of 0 to 4,095 potential values.

Summarizing, the Sentinel-2 multispectral mission provide information in the VNIR and SWIR domain, with medium spatial resolution and medium to high revisit time. From the spectral characteristics just described it can be stated that data consistency with Landsat family satellites should be ensured (see Figure 7 for visual comparison), still introducing some innovations including enhanced spatial, radiometric and temporal resolutions.

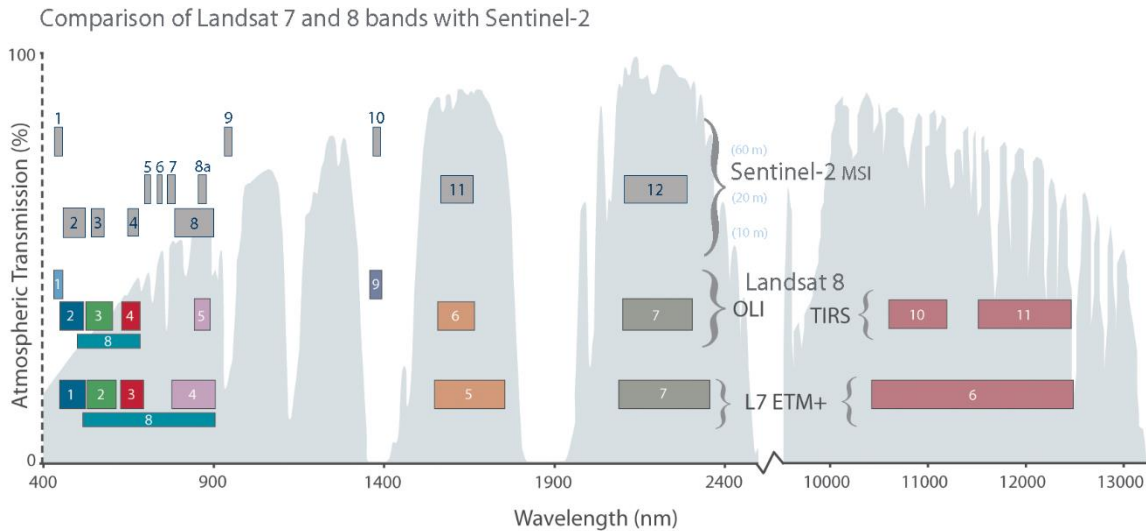


Figure 7. Comparison of multispectral bands of Landsat and Sentinel missions: Landsat-7 ETM+, Landsat-8 OLI and Sentinel-2 MSI. Credits: USGS

In conclusion, the first chapter has highlighted the main similarities among Landsat and Sentinel-2 missions regarding the acquisition of multispectral images. It is clear that great similarity in the design of the sensor allow consistency between these datasets, with some limitation that have to be quantified. However, the main aspect that must be considered in data continuity and for the combined used of these missions regards the satellite orbits and the geometry of acquisition. Indeed, observing the Earth from slightly different point of view might lead to different measurement of the reflected electromagnetic energy. The orbit drifting and the different equator crossing time cause the data acquisition in different solar angle geometry conditions, which might introduce discrepancy in the data consistency.

Chapter 2

2. Data products

The Landsat and Sentinel-2 missions acquire images of the Earth surface since the 70s through the multispectral instruments described in Chapter 1. After acquisition, the raw data undergo different processing steps and both the programs provide users with more and more complexity processing levels of the original raw data. In the following section the main products delivered by USGS and ESA through several platforms are presented.

2.1. Landsat collections and products

The programmatic development of Landsat program is based on ensuring data acquisition continuity (guaranteed by recent launch of Landsat 9) and facing the needs of interoperability and ready-to-use data (Wulder et al., 2019). Since its foundation, the programme is committed to continuously improving data quality and delivering data with different levels of processing and complexity to reach as many users as possible (Wu et al., 2019; Wulder et al., 2019).

First, as pointed out in Chapter 1, data continuity is ensured by the effort of mission designers to combine innovations with maintaining a similarity to

previous operational sensors. Furthermore, continuity is possible due to the careful scheduling of new launches in order to avoid data gap in the earth surface observations archive. However, as highlighted in Chapter 1, besides these efforts, some diversities between different sensors are impossible to avoid. Moreover, as it will be further discussed in the following chapters, the combined use of Landsat and Sentinel-2 data as a virtual constellation is highly promoted by both the programs. Indeed, allowing the interoperability of all available Landsat-like missions has many advantages for all the stakeholders, such as improving data availability for user and reducing costs for government and space agencies sharing facilities (for details see Chapter 3) (Lauer et al., 1997; Li and Roy, 2017).

In this context, in order to improve the interoperability between different subsequent operating missions, the Landsat archive was entirely reprocessed twice. After the first global Landsat 1 to 8 reprocessing into Collection-1 data (Dwyer et al., 2018), the second major reprocessing of the archive, performed in 2021, led to the release of Collection 2 data, which replaced Collection 1 starting from January 2022. A summary on the Collection-2 highlights can be found in (U.S. Geological Survey, 2021a). See Figure 8 for an overview on improvements of Collection-2 with respect of previous Collection-1. The major improvement provided by Collection-2 dataset regards geometry accuracy: for a better exploitation of archive interoperability, the Landsat-8 Ground Control Points (GCPs) were rebaselined to the ESA Sentinel-2 Global Reference Image (GRI). In addition, the digital elevation model sources were updated and accessibility from commercial cloud-based environment was improved (U.S. Geological Survey, 2021a).

Since the realisation of the Collection 1 data in 2016, the Landsat products are structured in a hierarchical three-level inventory to grant consistency in Landsat data processing and traceability of data quality records:

- Tier 1 (T1) includes products with the highest available data quality and with a geodetic accuracy showing a Root Mean Square Error (RMSE) equal or lower than 12m;
- Tier 2 (T2) includes products with a RMSE greater than 12m;
- Near real-time Tier (RT) includes Landsat 7 (ETM+) and Landsat 8/9 (OLI/TIRS) available for download in less than 12 hours after acquisition. These products are processed immediately upon downlink with limited calibration and ephemeris predictions, but useful in emergency response.

The data reprocessing into Collection-2 has definitely improved the data consistency along the archive and the interoperability with the S2 observations.

Type	Collection 1			Collection 2	
	Level 1 (Landsat 1-8)	Level 2 (U.S. ARD; Landsat 4-8)	Level 1 (Landsat 1-8 [Landsat 9])	Level 2 (Landsat 4-8 [Landsat 9])	Level 2 (U.S. ARD; Landsat 4-8 [Landsat 9])
Supporting software					
Processing software	Landsat Product Generation	L2PGS BRIDGE R0.8.x	Landsat Product Generation System (LPGS) R15.x		
Geometry					
Coverage	Global	U.S.	Global	Global ¹	U.S.
Geometric	Global Land Survey (GLS) 2000		Landsat 8 OLI Harmonized with Sentinel-2 Global Reference Image (GRI)		
Digital elevation	GLS DEM		GLS DEM/NASADEM/Alaska NED/CDEM/SNF/NPI/GIMP/ArcticDEM/RAMP		
Precision	Baseline		Improved usage of Ground Control Points (GCPs) to produce more		
Radiometry					
Solar/sensor viewing angle information	Angle Coefficient File	None (per-pixel correction already applied)	Angle Coefficient File + Band 4 Solar/Sensor Angle Bands	None (per-pixel correction already applied)	
TIRS Post-Stray Light Correction Adjustment (L8 only)	None		Post-Stray Light Residual Bias Applied	Post-Stray Light Residual Bias Applied	
Atmospheric correction/Level 2					
Surface Reflectance Algorithm Version	N/A	LEDAPS v3.2.1 (TM/ETM+) LaSRC v1.3.0 (OLI/TIRS)	N/A	LEDAPS v3.4.0 (TM/ETM+) LaSRC v1.4.1 (OLI/TIRS)	
Surface Temperature Algorithm Version	N/A	Landsat Single-Channel Surface Temperature v1.3.0	N/A	Landsat Single-Channel Surface Temperature v1.3.0	
Surface Reflectance Fill Value	N/A	-9999	N/A	0	
Surface Temperature Fill Value	N/A	-9999	N/A	0	
Data Type/Scaling Factor (Surface Reflectance)	N/A	Signed 16-bit integer 0.0001 (no offset)	N/A	Unsigned 16-bit integer 0.0000275 + -0.2	
Data Type/Scaling Factor (Surface Reflectance)	N/A	Signed 16-bit integer 0.1 (no offset)	N/A	Unsigned 16-bit integer 0.00341802 + 149.0	
L7 ETM+ Surface Temperature Band	N/A	Band 6L only	N/A	Bands 6L and 6H combined (6H if unsaturated, 6L otherwise)	

¹Global Level-2 products are only produced where solar angle constraints are met and atmospheric auxiliary data are available.

Figure 8 Comparison between the Landsat Collection-1 and Collection-2 sources (U.S. Geological Survey, 2021b)

At the same time, since its very beginning, the program has been devoted to reach as many users as possible, ensuring to deliver data in an uncomplicated form and grant their easy use (Pecora, 1972). In order to satisfy the different user type needs, data are provided with different processing levels. In particular, three different product levels are delivered: the global Level-1 data (Top Of Atmosphere, TOA), Level-2 data (Surface Reflectance) and the U.S. Analysis Ready Data (ARD). Figure 9 shows the geographical distribution of the available Level-1 and Level-2 products of the Landsat archive, for an amount of

more than 17 million of products. The data refers to the scenes acquired by Landsat-5, Landsat-7, Landsat-8 and Landsat-9 missions until January 20, 2023.

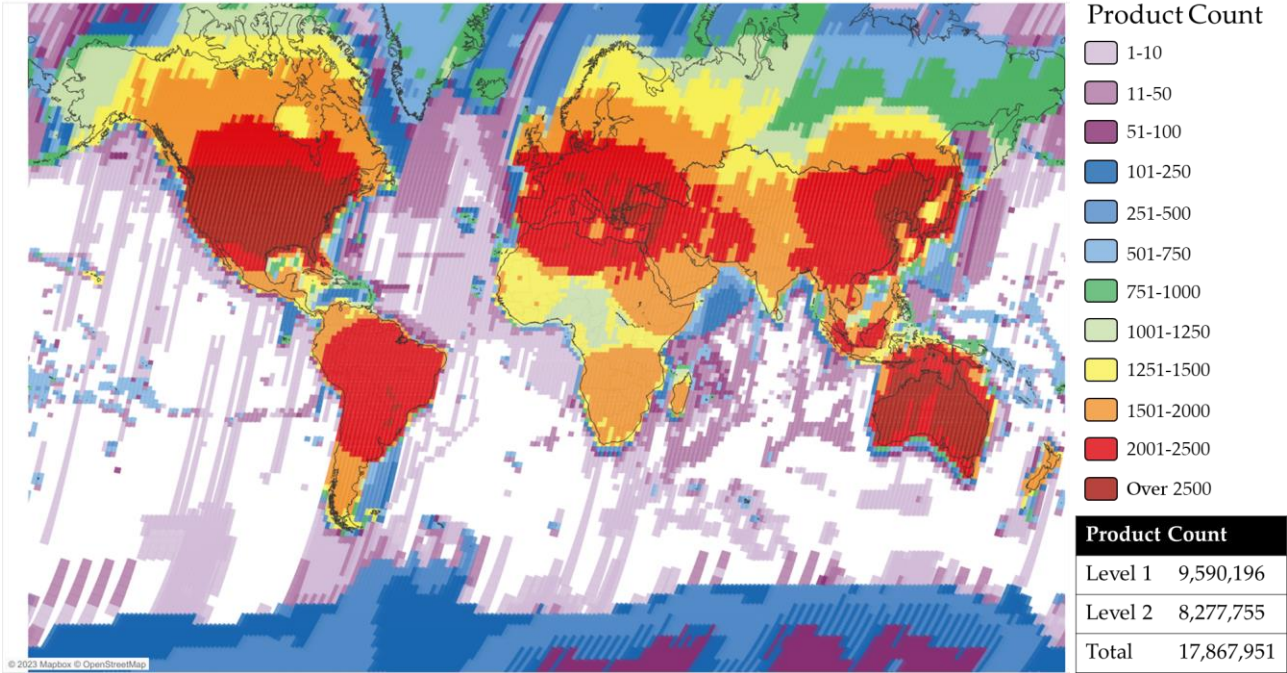


Figure 9. Landsat Level-1 and Level-2 products available acquired by Landsat-5, Landsat-7, Landsat-8 and Landsat-9 missions. Source: (U.S. Geological Survey, 2021c) <https://landsat.usgs.gov/landsat-archive-dashboard>

A radiometric and geometric processing performed on raw data allows to deliver Level-1 products which are characterized by cubic convolution resampling, North Up image orientation, and Universal Transverse Mercator (UTM) map projection (WGS84 datum). Moreover, a quality assessment (QA) band providing image quality statistics and cloud mask information computed through the CFMask algorithm is included (U.S. Geological Survey, 2019a, 2019b, 2022a). Refer to Foga et al. (2017) for more details about the CFMask algorithm.

Level-1 data, which represent the standard Landsat product available for all sensors since 1972, are delivered with their pixel values expressed as Digital Numbers (DN) in an unsigned 16-bit integer format. These values can be easily

reconducted to Top-of-Atmosphere (TOA) reflectance values by applying transformation factors given in the metadata.

Scenes classified as Tier-1 or Tier-2 are later processed to Landsat Level-2 Science Products (L2SP), while Near real time data are available just in the Level-1 format. The more recent Level-2 data products contain surface reflectance (SR) values. SR, as described by Vermote et al., is the “satellite derived top of atmosphere (TOA) reflectance corrected for the temporally, spatially and spectrally varying scattering and absorbing effects of atmospheric gases and aerosols”, and it is needed to monitor land surface reliably (Vermote et al., 2016a).

Usually Level-2 data are available within 24 hours after the T1/T2 scene classification. See Figure 10 for an overview of the timeline of product generation.

SR data are available from 1982 to present and are obtained applying atmospheric correction to Level-1 products with a Solar Zenith Angle lower than 76 degrees (Teixeira Pinto et al., 2020). To do that, the following algorithms are used: the Land Surface Reflectance Code (LaSRC) algorithm (Version 1.5.0) (Vermote et al., 2016a) was applied to Landsat-8 OLI products, while Landsat 4-5 Thematic Mapper (TM) and Landsat-7 Enhanced Thematic Mapper Plus (ETM+) surface reflectance products are generated using the Landsat Ecosystem Disturbance Adaptive Processing System (LEDAPS) algorithm (Version 3.4.0) (Masek et al., 2006).

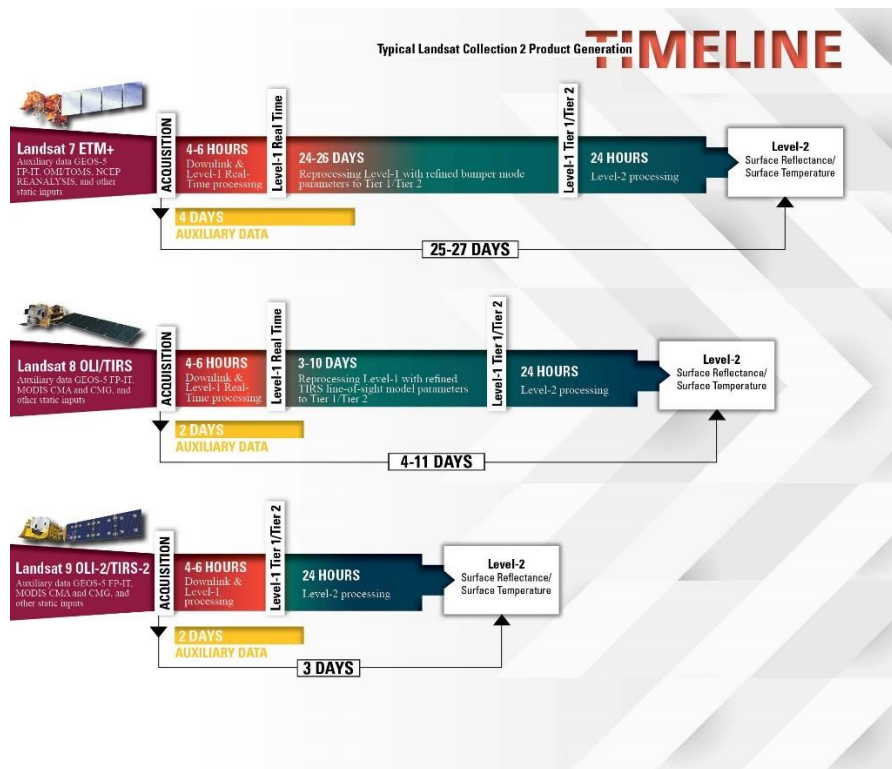


Figure 10 Time-line of different level products generation. Source: <https://www.usgs.gov/media/images/landsat-collection-2-generation-timeline>

Both the LEDAPS and the LaSRC are based on the Second Simulation of the Satellite Signal in the Solar Spectrum (6S) model for atmospheric correction. More precisely, the LaSRC uses the vectorial version of the code (Kotchenova et al., 2006; Vermote et al., 1997). They are physically based atmospheric correction methods that produce the reflectance that would be measured at ground level considering the absence of atmosphere along the Sun-target-instrument path, starting from the TOA observations (Vermote et al., 1997).

To do that, an estimation of atmospheric parameters is needed. Those are retrieved using the 6S code, a rigorous radiative transfer model, which provides a description of the properties of atmospheric constituents (such as the Rayleigh scattering and the gaseous absorption) based on ancillary data, and on retrieval of the aerosol concentration using the blue wavelengths bands, where the signal is mainly produced by aerosol (Vermote et al., 2016a, 1997).

For the LaSRC, ancillary data are provided by other missions, such as the climate information gathered from averaging 10 years of TERRA and AQUA Moderate Resolution Imaging Spectroradiometer (MODIS), or digital elevation terrain model from the Shuttle Radar Topography Mission (SRTM) (Vermote et al., 2016a). In Figure 11 the schema of how atmospheric correction is performed in the LaSRC as formulated by Vermote et al. is presented.

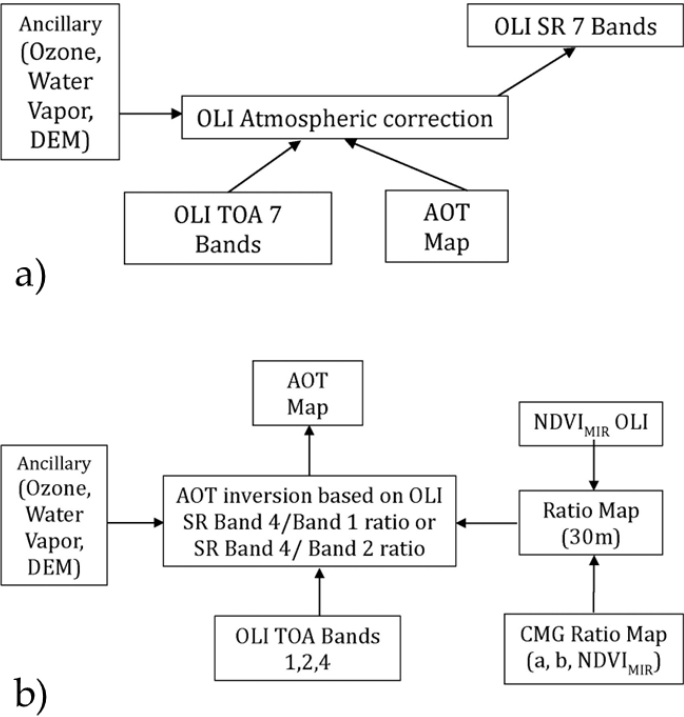


Figure 11. Schema of the LaSRC atmospheric correction. a) Flowchart of the Landsat8/OLI atmospheric correction scheme. (Vermote et al., 2016a) b) Flowchart of the OLI Aerosol Optical Thickness (AOT) retrieval (Vermote et al., 2016a)

On the other hand, LEDAPS uses ancillary data to estimate pressure, temperature, water vapor, ozone, and topography. For the aerosol retrieval a scene-dependent dense dark vegetation (DDV) is used (Kaufman and Sendra, 1988). In this case, auxiliary data are gathered either from other missions and in situ data. For example, water vapor is derived from NCEP (National Centers for

Environmental Prediction) and ozone quantity information from TOMS (Total Ozone Mapping Spectrometer).

The studies conducted by Vermote et al. and Pinto et al. demonstrated that the improvements of the OLI sensors allow to achieve better performances in the production of Level-2 products. Indeed, it is clear that LaSRC benefits of the use of Coastal aerosol band (0.433–0.450 μm), which cover shorter wavelengths than the conventional Landsat, TM and ETM + blue bands. Moreover, the LaSRC algorithm uses the OLI “cirrus” together with the TIRS bands instrument to produce a cloud and a cloud shadows masks (U.S. Geological Survey, 2022b).

Beside this technical aspects, some limitation of LEDAPS in the aerosol retrieval are known: those are mainly due to lacked DDV for optimal aerosol estimation (Teixeira Pinto et al., 2020; U.S. Geological Survey, 2019a).

Finally, when using Level-2 product, it is important to consider that even if the atmospheric correction algorithm is run on all the available scenes, the final product acquired at high latitude ($> 65^\circ$) should be used with caution. Indeed, high latitude areas should be excluded for different reasons: the solar elevation varies more near the poles; lower solar elevations at high latitudes results in longer atmospheric paths, which cause more scattering; the surface reflectance retrieval uncertainty greatly increases up to been highly inaccurate, at solar zenith angle > 76 degrees (Campbell and Aarup, 1989; U.S. Geological Survey, 2022b).

2.2.Sentinel-2 products

The Copernicus program and its space component share the Landsat’s programmatic development goal of spreading as much as possible the use of the produced satellite data (in the following we will mainly refer to the satellite

images, but great importance towards end users is assigned to the development of six services dedicated to as many themes: Atmosphere, Marine, Land, Climate Change, Security, Emergency). In fact, the EO market can benefit from the dissemination of this data, making the most of all the investments made by agencies and governments. To achieve this, it is important to address different types of users, providing products with different levels of complexity. Furthermore, by providing pre-processed and almost ready to use data, scientists and final users can focus on their applications instead of data preparation, requiring high remote sensing skills.

With this purpose, Sentinel-2 data, after the acquisition, undergo through different levels of processing, from raw data to Level-2 Science products (L2SP). Two different products are available for download to users: Level-1C and Level-2A (ESA, 2015).

Progressively complex processing is applied to produce Level-1C (L1C) and Level-2A (L2A) data. These are both orthorectified images delivered as granules (or tiles) with an extent of 100 x 100 km² in the UTM/WGS84 projection (Gascon et al., 2017).

In particular, Level-1C products are obtained after radiometric and geometric corrections (including orthorectification and spatial registration) applied to the Level-1B corresponding scenes. L1C products provide Top of Atmosphere (TOA) normalized reflectance observations, obtained from the radiance observation through the Solar Irradiance model described in (Thuillier et al., 2003) and then a b-spline interpolation of original values into the new orthorectified grid is performed.

Moreover, during the L1C processing, three masks layers are computed: quality, opaque clouds and cirrus clouds masks. Quality mask is based on image statistics provided by Level-1B. The opaque cloud mask is computed by using Band-1 (Coastal aerosol, 0.433 – 0.453 μm) and Band-12 (SWIR, 2.100 – 2.280 μm), while cirrus clouds uses the dedicated Band-10 (Cirrus, 1.360 – 1.390 μm) (Gascon et al., 2017). Finally, L1C products are stored as 15-bits integers and the physical values range from 1 (minimum reflectance 10^{-4}) to 10000 (reflectance 1), but values lower than 1 might occur due to particular angular reflectivity effects (Gascon et al., 2017).

The last processing is carried out in the Level-2 step: Level-2A products provide Bottom Of Atmosphere (BOA) reflectance images derived from the associated L1C scenes by applying them atmospheric correction through the Sen2Cor processor (Main-Knorn et al., 2017). The Sen2cor atmospheric correction estimates the atmosphere aerosol type and its optical thickness using the Dense Dark Vegetation (DDV) algorithm (Kaufman and Sendra, 1988); while the water vapour retrieval over land is performed with the Atmospheric Pre-corrected Differential Absorption (APDA) algorithm (Schläpfer et al., 1998) applied to S2 Band-8a and Band-9.

The Sen2Cor algorithm uses mainly two ancillary data: DEM by SRTM at 90 m spatial resolution, the Radiative Transfer Look-Up Tables (LUTs) obtained through the libRadtran software with rural/continental aerosol type condition (Emde et al., 2016; ESA, 2015; Mayer and Kylling, 2005). Moreover, when the DDV pixels on the L1C are not enough, the Sen2cor allows to use the meteorological data provided by the European Centre for Medium-Range Weather Forecasts (ECMWF) like Mean Sea Level Pressure estimations or total Column Ozone (ESA, 2015; Louis, 2016; Main-Knorn et al., 2017).

L2A output products are made of several layers. These include surface reflectance images for all the spectral bands but band 10 (Cirrus band), which is omitted, since it does not contain surface information (Louis, 2016). Moreover, an Aerosol Optical Thickness (AOT) and Water Vapour (WV) maps (60 m, 20 m and 10 m) are computed. A Scene Classification (SCL) map with eleven classes is provided (see Figure 12) together with Cloud confidence and a Snow confidence maps (Main-Knorn et al., 2017).






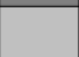



0	No Data (Missing data on projected tiles) (black)	
1	Saturated or defective pixel (red)	
2	Dark features / Shadows (very dark grey)	
3	Cloud shadows (dark brown)	
4	Vegetation (green)	
5	Bare soils / deserts (dark yellow)	
6	Water (dark and bright) (blue)	
7	Cloud low probability (dark grey)	
8	Cloud medium probability (grey)	
9	Cloud high probability (white)	
10	Thin cirrus (very bright blue)	
11	Snow or ice (very bright pink)	

Figure 12. Scene Classification (SCL) map classes (Main-Knorn et al., 2017)

Finally, the Sentinel-2 products can be identified with a processing baseline code, starting with the baseline 02.00 introduced in November 2015 as the Initial product Baseline. These Processing baselines are configuration files that evolve over the mission lifetime, and are useful to track corrections of errors in the processing chain. With these baseline, new features or product corrections might be included, updating and improving data quality. For example, as of January 25, 2022, the baseline 4.0 was introduced. The main change apported

with baseline 04.00 is the need to add an offset (readable in the metadata files) to the SR. This should result in an improvement of the performance over dark surfaces (ESA - European Space Agency, 2015; Gascon et al., 2017). Details on the processing baseline can be found in the periodic quality reports published through the ESA web pages (ESA - European Space Agency, 2022, 2015).

In conclusion, the differences of the TOA and BOA products provided by Landsat and Sentinel-2 programs have been presented, and the effort in generating inter-operable products has been highlighted.

The different product levels target different users and applications. In general, in the perspective of using these datasets for monitoring or change detection studies, the use of BOA observations is highly suggested, in order to exclude from the analysis the errors and changes due to modification in the atmosphere conditions instead of target surface actual change. However, as highlighted in section 1.1 and 1.2, Landsat and Sentinel-2 missions use three different algorithms to produce Level-2 products, each of them laying on different auxiliary data for the estimation of atmosphere parameters, such as water vapour, pressure or aerosol optical thickness. For this reason, it is important to assess the consistency of the Surface Reflectance datasets among these missions to ensure data continuity. Moreover, in order to evaluate the performance of atmospheric correction algorithms, the comparison of spectral response measured on the ground by in-situ survey with Level-1 and Level-2 satellite data could provide valuable information. An example of this approach and its utility can be found in (Teixeira Pinto et al., 2020).

Chapter 3

3. New approaches in EO data analysis

In the last decades a rising number of scientists and professionals have found in optical satellite imagery a useful data source for their analysis. The potential of these data has been pointed out for a great variety of disciplines (Malenovský et al., 2012), such as water applications, vegetation monitoring, natural and man-made hazard monitoring, but there is still an undiscovered potentiality that has not yet been fully exploited (Chawla et al., 2020; Malenovský et al., 2012; Poursanidis and Chrysoulakis, 2017; Tsatsaris et al., 2021; West et al., 2019). Among the fields that satellite remote sensing can fulfil with valuable information, Land Use Land Cover (LULC) and LULC changes, in the perspective of climate change studies, are those where Earth Observation (EO) represents the most efficient approach (Dash and Ogutu, 2016; Phiri et al., 2020; Tsatsaris et al., 2021). Indeed, missions like Landsat or Sentinel give a unique view over Earth surface dynamics and changes, capturing portion of Planet from the same point of view since the early 70s with a high-frequency revisit time and a medium geometric resolution. This represents a precious source of information from the past to deeply understand the dynamics that affected our rapidly changing world. Data availability together with recent

technical developments has open to new methodologies allowing to investigate these datasets extracting valuable information for wise resources management.

In this chapter the standard and new methodological approaches in multispectral data analysis are presented. Limits and possibilities of this methods are highlighted.

3.1.Change Detection Analysis traditional approaches and new perspectives

Satellite remote sensing provides a viable source of data for efficient monitoring of large areas from local to global scales. Indeed, as described in previous chapters, the need to quantify Earth's resources and improve Earth system process understanding led to the foundation of main international moderate resolution EO programs (Berger and Aschbacher, 2012; Lauer et al., 1997). In this context, the Landsat archive, together with the ongoing Sentinel-2, represents a precious source of information since they have been recording the Earth surface processes since the 1970s. The comparison of images acquired over the same area at different time is a very well-known powerful tool to detect and highlight changes occurred over that Earth surface portion. In remote sensing, since the very beginning, this approach in image processing is known as Change Detection Analysis (CDA).

Change Detection (CD) can be defined as the process of identifying differences in the state of an object or phenomenon by observing it at different times (Singh, 1989). For the sake of brevity only a brief summary of the main standard CD approach is provided here, a more detailed description of the standard CDA can be found in (Canty, 2019).

Standard digital remote sensed images CD is made of two phases. The first consists in the accurate selection of data and their pre-processing procedures, such as precise spatial registration. This step is fundamental to ensure that modifications highlighted by the procedure are due to effective land cover (LC) changes. The second phase is the proper analysis, allowing the detection of changes in the LC.

To do that, many algorithms and procedures were developed in the past and became standard approach in the CD analysis. Those can be grouped into (Mas, 1999):

- Image enhancement methods, based on unclassified image data, which combine the data mathematically to enhance the information content. Among these methods, for example naive image-differencing or image-ratio are included, as well as principal component analysis (PCA) (Ehlers et al., 2010);
- Multitemporal analysis, based on an isochronic analysis of a multitemporal image data set (Ehlers et al., 2010). Following this approach, single n-bands images acquired at different date t1 and t2 are merged together into a new image with $2*n$ bands, allowing to extract the changed areas in the merged image.
- Post classification comparison, involve the comparison of two independent classification results for at least two different dates. This methods allow the determination of the change occurred from one class to another class but is limited by the quality of each single classification. (Tomowski et al., 2010).

Basically, the change detection studies of remotely sensed data are based on two following principles (Mas, 1999):

- changes in land cover cause changes in radiance values;

- changes in radiance due to land cover change are larger with respect to those caused by others factors, such as atmospheric conditions or illumination differences.

Regarding the latter point, it is important to remark that EO measurements their self are affected by errors, among other atmosphere has a crucial impact on the quality of observations. Furthermore, as described in Chapter 2, when retrieving information of the target surface over a time interval, atmospheric correction algorithm are needed “to prevent changes due to atmospheric effects being interpreted as changes in the surface conditions”(Vermote et al., 2016b). For this reason, in CDA involving multitemporal analysis based on radiometric change detection Bottom of Atmosphere products are necessary. In this regard, Landsat and Sentinel program put their effort in delivering always improved products, described in detail in Chapter 2, limiting as much as possible these errors. However, illumination changes due to different atmospheric condition or geometric acquisition should be account when doing CDA.

Finally, in the last decades some important innovations have drastically changed the possibility in remotely sensed data image processing analysis, such as the just mentioned improved quality datasets, their availability and new cloud-based technology to perform the analysis. All these innovations moved CDA to new methodological approaches, improving our knowledge and deepen the understanding of Earth surface processes.

3.1.1. Open-access policy and cloud-based platforms

One of the most significant turning point for the remote sensing market was in 2008, when the Landsat policy turned into open-access (Woodcock et al., 2008). The USGS decision of making the Landsat archive available at no cost to anyone via the internet was unprecedented for medium spatial resolution data

(Woodcock et al., 2008). This new paradigm started a much faster spread of remote sensing applications, allowing more and more scientists to get familiar with the data and to start integrating it as part of their research. The impact of this change in the access to data is evident when looking at the records of scientific papers including Landsat missions. Indeed, as shown in Figure 13, the number of citations increased significantly after the decision to open the archive in December 2008. In addition, beside the tangible expansion in data utilizations, the no-charge data distribution has led to an increase of the depth and scope of the science questions asked and applications undertaken” (Wulder et al., 2022).

The same programmatic path has been followed in the design and maintenance of the open-access Sentinel-2 missions, providing data at no cost to users.

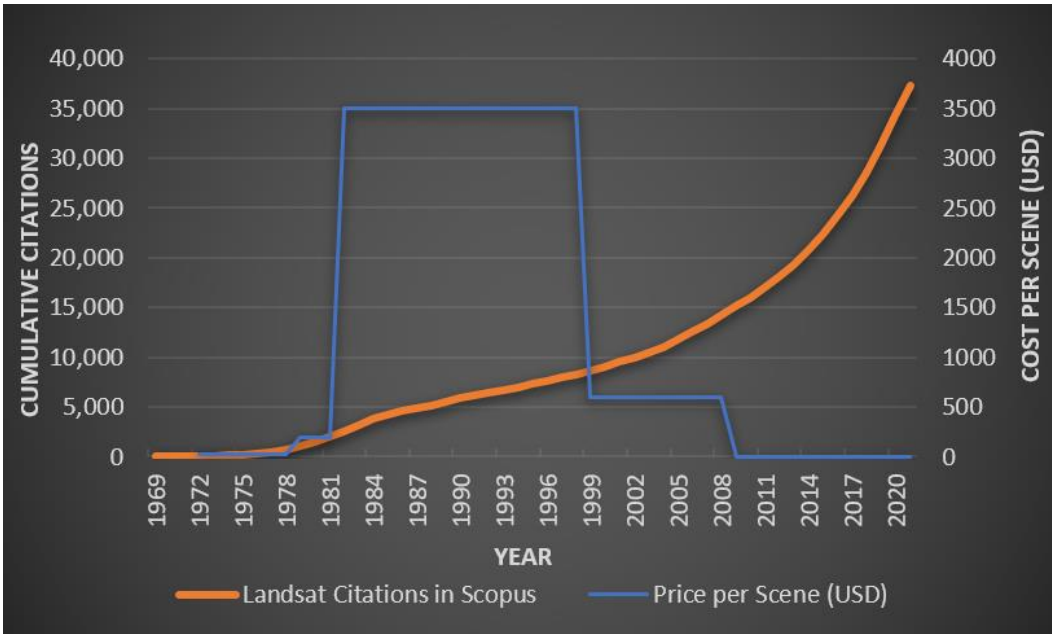


Figure 13. Record in Scopus of scientific papers involving Landsat products (orange line) and the cost per scene (blue line) from 1970 to 2022. Source: <https://www.usgs.gov/landsat-missions/landsat-project-statistics>

In this context, the development of new technologies in the era of big EO data is crucial to enable the full exploitation of the data potentiality (Casu et al., 2017). This demand has been successfully accomplished with the development of cloud-computing technologies like Google Earth Engine (GEE), which is the platform used in this research (Yao et al., 2019). GEE is a platform for geospatial analysis consisting in a multi-petabyte analysis-ready data catalog co-located with a high-performance, intrinsically parallel computation service powered by Google (Gorelick et al., 2017). From 2010 GEE makes available to users over 40 years of satellite imagery from more than 600 different EO, such as all Landsat and Sentinel-2 collections, and other geospatial datasets like digital terrain models, climate, weather and demographic data. In addition to this huge data warehouse, GEE offers Google's computational capabilities and algorithms for data processing. The relative simplicity of this tool opens a new frontier for remotely sensed Big Data analysis, which would normally require significant computing and storage capacity, resulting in large hardware and software costs. Indeed, this cloud-computing platform, combining all these data in one easy-to-use system with significant computational power, allows scientists (more than 500,000 registered users) to deepen their investigations of the satellite data archives (Wulder et al., 2022). Figure 14 shows the increase of Landsat collections users between 2018 and 2022 through the GEE platform.

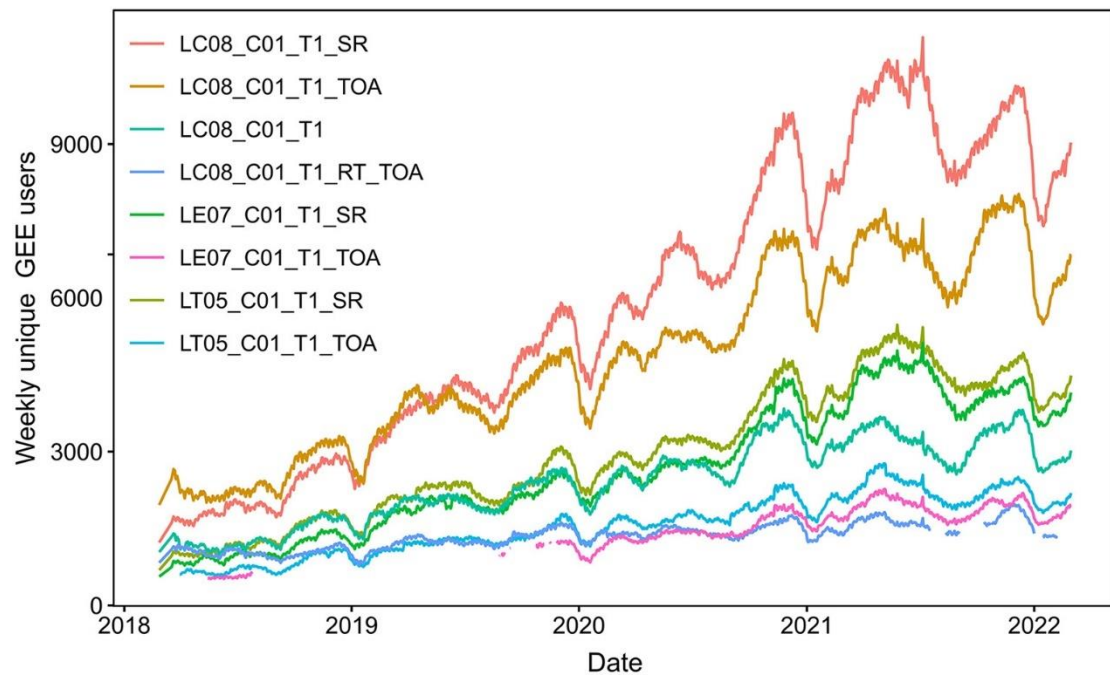


Figure 14. Summary of usage of redistributed Landsat Collection 1 data on Google Earth Engine, by collection and product traits. Source: (Wulder et al., 2022)

3.2. Time series analysis and data harmonization

The nowadays available open-access remote sensing datasets represent a massive source of information that has not been completely exploited yet to its full potential and requires new methodologies, supported by technological advances (West et al., 2019). Among these, Time Series Analysis (TSA) is undoubtedly promising to better understand Earth's surface change processes, making it possible to study not only drastic changes, but also long-term or more subtle phenomena, crucial in climate change studies. Thanks to this great amount of free data accessible through cloud computing platforms, traditional remote sensing applications such as change detection have successfully moved from standard approaches involving image pairs to TSA of remotely sensed data (Mas, 1999; Zhu, 2017). The pixel-based TSA for monitoring pixel trajectories over time represents nowadays a well-established methodological trend (Chaves et al., 2020) Figure 15. An overview regarding potentiality,

methodologies and challenges of remote sensing time series can be found in (Kuenzer et al., 2015).

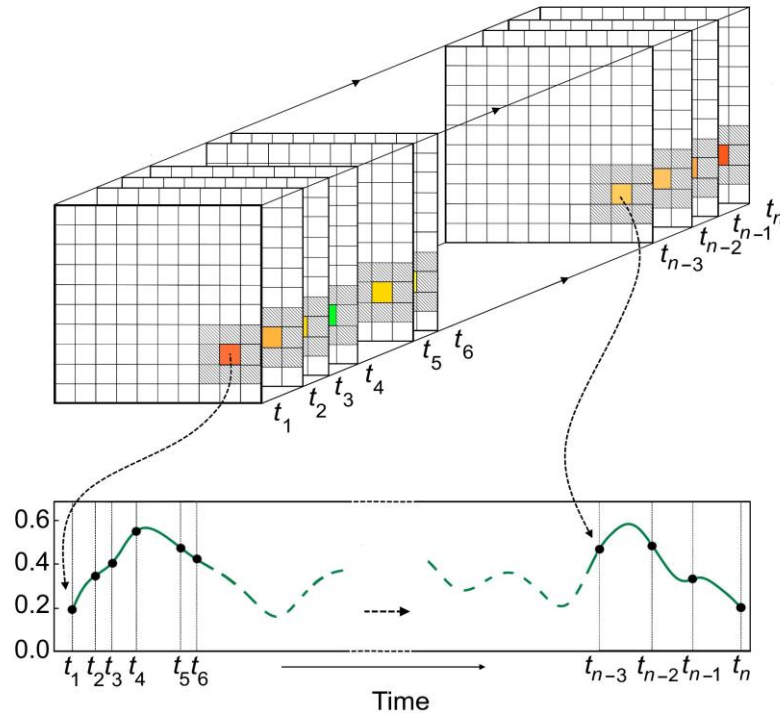


Figure 15. Schema of remotely sensed data time series. Source: (Ghaderpour and Vujadinovic, 2020)

Moreover, this approach to the analysis of multispectral data is rapidly becoming a standard practice in vegetation-related studies, including monitoring of both forest and agricultural environments (Banskota et al., 2014; Xue et al., 2014). The reviews by Bégué et al. (2018) and Gómez et al. (2016) cover a variety of examples where this methodology proved to be effective in identifying seasonal phenological variation, allowing, for example, a better classification of crop types. In this context, information on the biophysical characteristics of vegetation collected by multispectral cameras can be successfully synthesised thanks to vegetation indices (VIs), which are obtained through the combination of spectral bands (Xue and Su, 2017; Zeng et al., 2020).

Four of the most widely used VIs are considered in this study: Normalized Difference Vegetation Index (NDVI), Soil Adjusted Vegetation Index (SAVI), Enhanced Vegetation Index (EVI) and Normalized Difference Moisture Index (NDWI). In the last years, these VIs has been successfully implemented in a large variety of applications for their simplicity and effectiveness (Liu et al., 2020; Nagy et al., 2021; Roy and Yan, 2020; Wang et al., 2017; Zhong et al., 2019).

However, in the context of TSA, it is important to remarks that remotely sensed time series are often non-stationary and unequally spaced (irregularly sampled) dataset. Moreover, they are often affected by noise due to atmospheric effects, such as clouds or haze (Ghaderpour and Vujadinovic, 2020). These are some of the known limits of multispectral derived datasets that need to be overcome to improve TSA applications. For example, a recent study conducted by USGS (Wu et al., 2019), investigating user needs for future Landsat missions, raised attention on desired cloud-free observation frequency: the survey showed that in the 71% of cases, subject matter experts believe that a weekly cloud-free observation frequency is a breakthrough requirement. Having cloud free data information on a weekly basis would actually lead to a significant improvement in data effectiveness for their applications. One possible answer to this need is the harmonisation of several sensors, which would allow to increase the number of acquisitions. Furthermore, since the main limitation of passive sensors is the dependence on weather conditions, harmonisation would increase the probability of collecting cloud-free images. Looking at the present, as demonstrated by the analysis of Li and Chen (2020), the harmonization of Sentinel-2 MSI and Landsat OLI/OLI-2 (equipped on Landsat-8 and Landsat-9) would highly increase the revisit time, up to a 2.3 days global average, giving satellite remote sensing a new perspective for land surface monitoring.

In order to achieve these purposes, by building synthetic multi-satellite constellation, some authors proposed statistical calibration parameters to adjust spectral reflectance values across similar instruments. Mandanici and Bitelli (2016) analysed the correlation between corresponding bands of Sentinel-2A and Landsat-8 on selected but limited sites, also evaluating the effects of spatial heterogeneity. Chastain et al. (2019) proposed a cross sensors comparison of Sentinel-2A and 2B MSI, Landsat-8 OLI, and Landsat-7 ETM+ top of atmosphere spectral bands, giving the regression coefficients that allow to integrate MSI data with ETM+ and OLI over the conterminous United States (CONUS). Denaro and Lin (2020) proposed the use of non-linear models for the cross-sensor normalization of Landsat-7 and Landsat-8 imagery. More recently, Xie et al. (2022) estimated cross-sensors linear transformations between Landsat-8 and Sentinel-2 based on only 76 image pairs spread all over the world. Cao et al. (2022) proposed a similar analysis including Landsat-7 and deriving the transformations from a larger dataset but limited to the Chinese territory.

Other authors explicitly addressed the problem of vegetation index comparison. Li et al (2013) conducted a cross-comparison of four VIs derived from 6 pairs of Landsat-7 and Landsat-8 images over Myanmar. Roy et al. (2016) compared Landsat-7 ETM+ and Landsat-8 OLI and computed transformation coefficients for the integration of their spectral bands and the Normalized Difference Vegetation Index (NDVI) obtained from them. Chen et al. (2019) proposed transformations to harmonize the NDVI computed from Landsat-4-5 multispectral scanner and thematic mapper, elaborating on simulated data derived from Hyperion hyperspectral images. Mancino et al (2020) a specific case study in Italy comparing six VIs between Landsat-7 and Landsat-8 and

finding statistically significant differences among four different land cover classes.

In the last years, NASA and USGS developed the Harmonized Landsat-8 and Sentinel-2 surface reflectance data set (HLS) currently at version 2.0 which provide harmonized multispectral bands with global coverage (Claverie et al., 2018). However, at the time of the writing, there are not “analysis ready data” for vegetation index TSA including the full Landsat constellation and Sentinel data. Moreover, there is not any study available assessing spectral quality measurements by the new Landsat-9 nor evaluation of its interoperability with the ongoing Landsat and Sentinel-2 instruments.

Chapter 4

4. Cross-sensors comparison of popular vegetation indexes from Landsat TM, ETM+, OLI and Sentinel MSI for time series analysis

In the perspective of a long and dense time-series analyses for environmental monitoring applications, the paper discusses a cross-comparison analysis between the different instruments of Landsat and Sentinel Missions (TM, ETM+, OLI and MSI) and products levels (Collection-2 Surface Reflectance for Landsat and Surface Reflectance for Sentinel-2). The calibration coefficients for four of the most popular vegetation indexes (NDVI, EVI, SAVI and NDMI) were estimated, with the aim of harmonizing and minimizing radiometric differences for the combined use of these sensors. For this purpose, more than 20,000 pairs of images almost simultaneously acquired (+/- one day tolerance

window) were selected over a period of several years (depending on the lifespan overlap of every sensor pair). Vegetation indices (VIs) were computed for each image, and, for each cross-comparison, 100 random extractions of 300,000 sample pixels were performed all over the European continent. Linear transformation functions for each VI and between each sensor couple were computed by regression analyses, also assessing the repeatability of the estimation. Furthermore, the stability over time of the obtained coefficients was assessed when enough years of corresponding observations are available.

In the following sections we provide: a summary of L5, L7, L8 and S2 characteristics and their products; a description of the methodology including pre-processing, data gathering, sampling and statistical analysis; and finally, the results and the transformation coefficients are presented.

4.1. Materials

4.1.1. Landsat

Landsat program has been collecting Earth surface multispectral images since 1972 and it represents the longest living remote sensing mission in the world. It is a joint project between NASA, responsible for the satellite construction and launch, and USGS, which manages the archive and the distribution of data. The key parameters defining Landsat missions are the medium spatial resolution, the temporal resolution and the spectral coverage. The mission was designed to achieve efficient multispectral monitoring of land surface, with 30 m pixel average resolution and a revisit cycle of 16 days on every point on Earth. Every new Landsat satellite has been designed to create a pair constellation with the previous one still operating, resulting in an 8-day revisit coverage (Wulder et al., 2019).

This study included datasets acquired by three different Landsat instruments: L5 Thematic Mapper (TM), L7 Enhanced Thematic Mapper Plus (ETM+) and L8 Operational Land Imager (OLI).

After its launch in March 1984, L5 was operated by USGS until January 2013. For more than 29 years it acquired over 2.5 million images of the Earth, largely exceeding its original three-year designed life. Its TM sensor captured the Earth surface spectral reflectance in six bands at 30m spatial resolution and 120m spatial resolution for the thermal band (Chander et al., 2007).

The L7 was launched in April 1999 and carried the ETM+ instrument. The ETM+ represents an improvement with respect to the TM sensors, with the addition of the panchromatic 15m resolution band. From June 2003, when the Scan Line Corrector (SLC) failed, L7 images were acquired and delivered with gaps, producing a loss of information up to the 22% (Andréfouët et al., 2003). The decommissioning of L7 began in mid-2021, leaving its orbit to the new Landsat-9.

L8 was launched in February 2013 equipped with the OLI and the Thermal Infrared Sensor (TIRS). OLI measures the visible, NIR and SWIR part of the electromagnetic spectrum, while TIRS operates in the thermal region. Following the spectral improvements achieved with ETM+ instrument, OLI was designed with a panchromatic 15 m band and eight 30 m spectral bands. In OLI the new ultra-blue band (Band1) and the Band 9 (1.36 - 1.38 μm) are useful in coastal/aerosol studies and cirrus cloud detection respectively. Table 5 gives a summary of L5, L7 and L8 spectral characteristics.

In this study the SR Collection-2 Tier-1 dataset was used for all the Landsat instruments considered. Refer to Chapter 1 and 2 for details about sensor

characteristics and mission products. Table 5 provides a summary on spectral and geometric characteristics of the datasets used in the study.

Table 5 Spectral bands characteristics of L5 TM, L7 ETM+ and L8 OLI (U.S. Geological Survey, 2021d)

Landsat-5 TM			Landsat-7 ETM+			Landsat-8 OLI		
Bands	Wavelength (μm)	Res.	Bands	Wavelength (μm)	Res.	Bands	Wavelength (μm)	Res.
B1 Blue	0.45 - 0.52	30 m	B1 Blue	0.441 - 0.514	30 m	B1 Coastal/Aerosol	0.435 - 0.451	30 m
B2 Green	0.52 - 0.60	30 m	B2 Green	0.519 - 0.601	30 m	B2 Blue	0.452 - 0.512	30 m
B3 Red	0.63 - 0.69	30 m	B3 Red	0.631 - 0.692	30 m	B3 Green	0.533 - 0.590	30 m
B4 NIR	0.76 - 0.90	30 m	B4 NIR	0.772 - 0.898	30 m	B4 Red	0.636 - 0.673	30 m
B5 SWIR-1	1.55 - 1.75	30 m	B5 SWIR-1	1.547 - 1.749	30 m	B5 NIR	0.851 - 0.879	30 m
B6 TIR	10.41 - 12.5	120 m	B6 TIR	10.31 - 12.36	60 m	B6 SWIR-1	1.566 - 1.651	30 m
B7 SWIR-2	2.08 - 2.35	30 m	B7 SWIR-2	2.064 - 2.345	30 m	B10 TIR-1	10.60 - 11.19	100 m
-	-	-	B8 Pan	0.515 - 0.896	15 m	B11 TIR-2	11.50 - 12.51	100 m
-	-	-	-	-	-	B7 SWIR-2	2.107 - 2.294	30 m
						B8 Pan	0.503 - 0.676	15 m
						B9 Cirrus	1.363 - 1.384	30 m

4.1.2. Sentinel-2

S2 mission is a twin polar-orbiting satellite phased at 180° to each other: Sentinel-2A and Sentinel-2B were launched in 2015 and 2017, respectively. Their orbit is angled of 98.62° and acquires images over land and coastal areas with a 290 km width swath, covering the Earth surface between the latitudes 56° South and 83° North. The Mean Local Solar Time at the descending node is 10:30 AM (ESA, 2015).

The two satellites are equipped with the Multi-Spectral Instrument (MSI), a sensor that measures the Earth's reflected radiance in 13 spectral bands, from VNIR to SWIR, providing imagery at different spatial resolution, ranging between 10 m and 60 m, as summarized in Table 6. Details about sensor characteristics and Sentinel-products can be found in Chapter 1 and 2. In the study S2 Level-2A products were used.

Table 6 Spatial and spectral resolution of S2 MSI: band wavelengths interval and their geometric resolution.

Sentinel-2 MSI		
Bands	Wavelength (μm)	Res.
B1 Coastal aerosol	0.433 – 0.453	60 m
B2 Blue	0.458 – 0.523	10 m
B3 Green	0.543 – 0.578	10 m
B4 Red	0.650 – 0.680	10 m
B5 Red Edge 1	0.698 – 0.713	20 m
B6 Red Edge 2	0.733 – 0.748	20 m
B7 Red Edge 3	0.773 – 0.793	20 m
B8 NIR	0.785 – 0.900	10 m
B8a NIRn	0.855 – 0.875	20 m
B9 Water Vapour	0.935 – 0.955	60 m
B10 Cirrus	1.360 – 1.390	60 m
B11 SWIR	1.565 – 1.655	20 m
B12 SWIR	2.100 – 2.280	20 m

Figure 16 shows the operational timeline of the satellites considered in the study and gives a comparison of main mission characteristics.

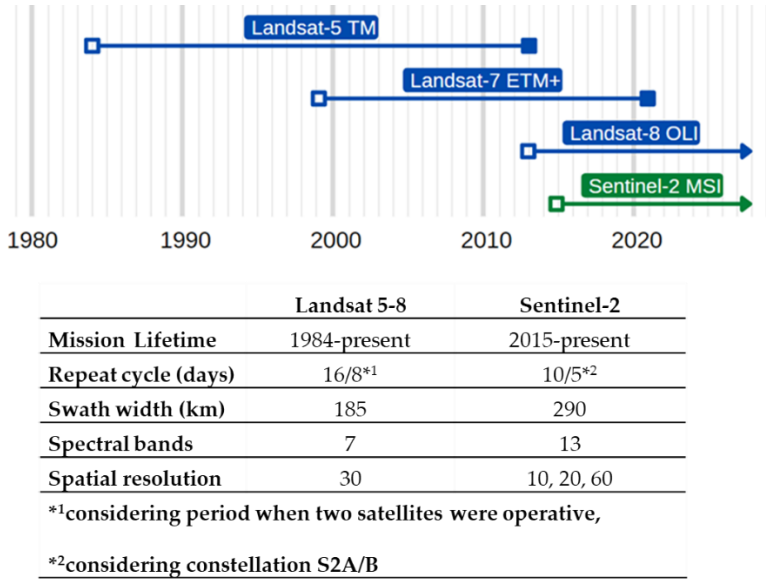


Figure 16 Landsat and Sentinel satellites. Top: timeline of operational periods. Bottom: comparison of main characteristics of the two missions.

4.1.3. Vegetation Indices

Four vegetation indices were considered in this study: NDVI, EVI, SAVI and NDMI. These VIs are obtained from the following bands: Green, Red and Red-edge bands (highly correlated with chlorophyll and other pigments contents); NIR band (sensitive to leaf structure) and the SWIR band (sensitive to water content) (Xue and Su, 2017; Zeng et al., 2020). NDVI is the most widespread index sensitive to chlorophyll computed from NIR and Red bands (Huang et al., 2021; Krieglner et al., 1969). Being one of the most stable indexes, NDVI allows comparisons of seasonal and inter-annual changes in vegetation growth. Some improvements to NDVI were implemented to reduce the environmental effects to index variations. SAVI proposed by Huete (1988) minimizes background soil brightness influences of NDVI. On the other hand, the EVI is used to reduce atmospheric effects that could lead to high biomass saturation (Huete et al., 2002). Finally, NDMI consists in the normalized difference between NIR and SWIR and it helps in vegetation water content assessment, useful for example when dealing with irrigations systems (Ferrant et al., 2017; Gao, 1996). In this study, these VIs were calculated using the Landsat Collection-2 and Sentinel Level-2A SR datasets, selecting the most similar bands across sensors. Details regarding the index formulas and the bands used for the calculations, for each sensor examined, are given in Table 7. The coefficients in the formulas for EVI and SAVI are those suggested by USGS for the computation of on-demand vegetation indexes (Masek et al., 2006; U.S. Geological Survey, 2021c; Vermote et al., 2016a).

Table 7 Left: Vegetation Indexes formulas. Right: comparison between bandwidth bands selected for each sensor for the VIs computation.

$NDVI = \frac{NIR - Red}{NIR + Red}$ $EVI = 2.5 \cdot \frac{NIR - Red}{NIR + 6 \cdot Red - 7.5 \cdot Blue + 1}$ $SAVI = 1.5 \cdot \left(\frac{NIR - Red}{NIR + Red + 0.5} \right)$ $NDMI = \frac{NIR - SWIR}{NIR + SWIR}$	TM	ETM+	OLI	MSI	
	(μM)	(μM)	(μM)	(μM)	
	Blue	B1	B1	B2	B2
		(0.45-0.52)	(0.441-0.514)	(0.452-0.512)	(0.458-0.523)
	Red	B3	B3	B4	B4
	(0.63-0.69)	(0.631-0.692)	(0.636-0.673)	(0.650-0.680)	
NIR	B4	B4	B5	B8A	
	(0.76-0.90)	(0.772-0.898)	(0.851-0.879)	(0.855-0.875)	
SWIR	B5	B5	B6	B11	
	(1.55-1.75)	(1.547-1.749)	(1.566-1.651)	(1.565-1.655)	

4.2. Methodology

The vegetation indexes derived from the spectral bands of the TM, ETM+, OLI and MSI sensors were compared. The sensors were compared in pairs, by randomly sampling the indexes values from overlapping images acquired with a maximum delay of one day, as detailed in the following sections. As a consequence, to ensure statistically robust samples of data, the comparison was possible just between those sensors which were actively operating for a common period of time of at least 2 years. For this reason, the newer Landsat 9 sensor was not included in this study. In order to perform the entire data pre-processing and extraction, a workflow was implemented in the Google Earth Engine (GEE) platform through the Javascript API. While the final statistical analysis on sampled data was performed in Python environment.

4.2.1. Study area

The study area covers the entire European continent (Figure 17), which was tiled in 100 subregions for computational reasons. This area comprehends a wide spectrum of land cover types and ecosystems, and thus it provides an exhaustive and varied set of data.

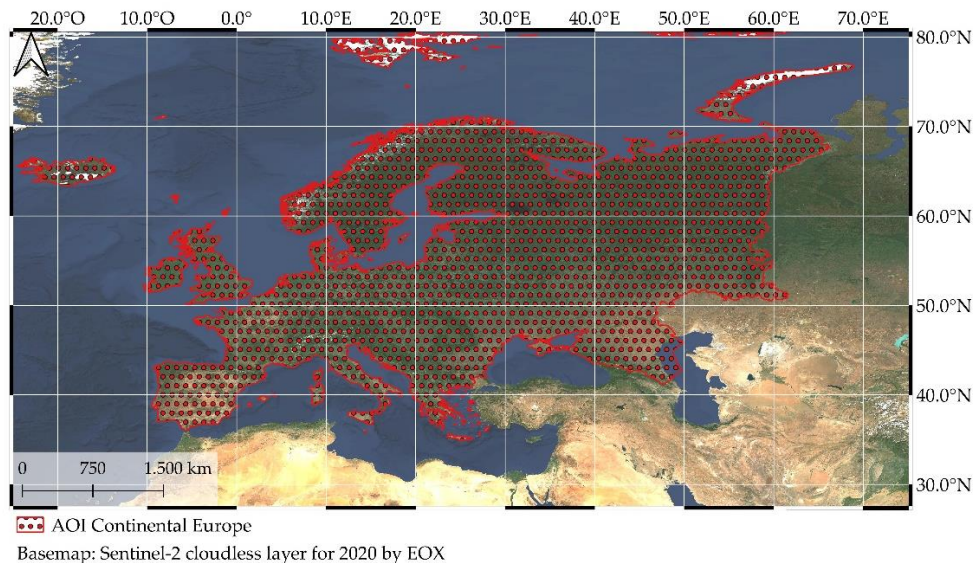


Figure 17. The Area of Interest covered by the analysis including continental Europe. Basemap: Sentinel-2 cloudless - <https://s2maps.eu> by EOX IT Services GmbH (Contains modified Copernicus Sentinel data 2020).

4.2.2. Data gathering

The data sampling was completely performed in GEE accessing the Landsat (Collection-2) and Sentinel-2 surface reflectance (SR) datasets available in its catalogue.

First of all, the image collections were filtered based on time, space and cloud cover. Specifically, at least two common years of acquisition were selected between the two missions; the search area was limited to Europe and the maximum image cloud cover percentage was set to 1% for Landsat data and to 0.1% for S2 data. This difference on cloud cover filter is to compensate for the higher revisit time of S2, resulting in higher data availability, and to consider

the lower effectiveness of the cloud masking algorithm of S2 (Baetens et al., 2019). In order to obtain balanced datasets concerning images acquired in different seasons, and thus in different vegetative states, the dataset was split into two different time spans: one from October to March (autumn-wintertime) and one from April to September (spring-summertime). Because of cloud free images shortage during wintertime and to balance the datasets between autumn-wintertime images and spring-summertime images, the search time span for the autumn-wintertime images were doubled. In addition, the search time span was carefully adjusted to ensure a similar population of valid pixels for each sensors couple, considering also the operational period of each sensor and some specific peculiarities, such as the SCL issues of L7 (details can be found in Table 8).

Table 8 Sentinel and Landsat data filtering for the analysis. Firstly, time span, covering summer and winter period separately, and cloud cover percentage are the filters applied to a single satellite collection. The total record (Tot records) is the number of images satisfying those filters for each satellite. The Joined collection is the number of pairs cross sensors images satisfying clouds and time span filters which were acquired over the same area almost in the same date (+/- 1 day) by the two satellites considered in the cross-sensor analysis.

L7-L8	Start	Stop	Month span	Cloud cover	Records	Tot records
L8 summer	01/01/2017	01/01/2021	Apr - Sep	1%	7994	13680
L8 winter	01/01/2013	01/01/2021	Oct - Mar	1%	5686	
L7 summer	01/01/2017	01/01/2021	Apr - Sep	1%	6366	10321
L7 winter	01/01/2013	01/01/2021	Oct - Mar	1%	3955	
Joined collection					9608	
L5-L7	Start	Stop	Month span	Cloud cover	Records	Tot records
L7 summer	01/01/1999	01/01/2007	Apr - Sep	1%	7721	12148
L7 winter	01/01/1999	01/01/2012	Oct - Mar	1%	4427	
L5 summer	01/01/1999	01/01/2007	Apr - Sep	1%	4821	7344
L5 winter	01/01/1999	01/01/2012	Oct - Mar	1%	2523	
Joined collection					3812	
L8-S2	Start	Stop	Month span	Cloud cover	Records	Tot records
S2 summer	01/01/2018	01/01/2020	Apr - Sep	0.1%	14824	25403
S2 winter	01/01/2016	01/01/2020	Oct - Mar	0.1%	10579	
L8 summer	01/01/2018	01/01/2020	Apr - Sep	1%	4141	7121
L8 winter	01/01/2016	01/01/2020	Oct - Mar	1%	2980	
Joined collection					4924	
L7-S2	Start	Stop	Month span	Cloud cover	Records	Tot records
S2 summer	01/01/2018	01/01/2020	Apr - Sep	0.1%	14824	25403
S2 winter	01/01/2016	01/01/2020	Oct - Mar	0.1%	10579	
L7 summer	01/01/2018	01/01/2020	Apr - Sep	1%	3294	5275
L7 winter	01/01/2016	01/01/2020	Oct - Mar	1%	1981	
Joined collection					4520	

4.2.3. Pixel masking

At this point, the selected images were pixel-wise masked on the basis of the pixel quality assessment (QA) bitmask band. For Landsat products, it was generated from the CFMASK algorithm. The CFMASK derives from the Function of Mask (FMask), which is able to label the scene pixels as cloud, cloud shadow, cirrus, snow/ice or water, and provides a bit-mapped values output (Foga et al., 2017; Zhu and Woodcock, 2012). This product was used to remove high and medium confidence clouds, dilated clouds, cloud shadows, snow/ice and water pixels, in order to include in the analysis only clear land pixels. Only for L8 products, it was possible to mask also pixel marked as high confidence cirrus.

The same process was performed for the S2 images by means of the Scene Classification map (SCL) quality assessment band, which, likewise the one for the Landsat products, labels the pixels on the basis of a classification process and thus allows the user to easily perform pixel-wise masking. High and medium probability clouds, cloud shadows, cirrus, water and snow/ice pixels were removed, accordingly with the masking process done for the Landsat products (Louis et al., 2010).

Furthermore, saturated and out-of-range pixels were masked using the radiometric saturation quality assessment bands and valid value range. This means that all the saturated pixels and the pixels with a value of the vegetation index outside the range of interest, which is [0; 1] for NDVI, EVI and SAVI, and [-1; 1] for NDMI, were discarded.

4.2.4. Image coupling, co-registration and reprojection

The images, or portion of images, of two different sensors, filtered and masked as described above, which are spatially overlapping and acquired

within 24 hours, were paired, finely co-registered with each other, reprojected, to make sure the images shared the same coordinate reference system, and resampled at the coarsest resolution (30m). This was done to avoid differences in the VI values due to land cover changes, bad spatial overlap or differences in pixel size.

Despite the maximum time difference of 24 hours between the two images of each pair, which should ensure no land cover changes occurred, there are still some pixels showing huge reflectance differences. Therefore, the paired images were further masked following the methodology proposed by Roy et al. (2016), which is based on the pixel-wise difference in the blue band values. However, using here images already corrected at surface reflectance, pixels with a difference greater than the 50% of the average were discarded.

4.2.5. Sampling

For computational limit reasons, cross sensors comparisons were not performed on the entire pixel population but on statistical samples randomly extracted from the population of valid pixels (after masking) belonging to the paired images. For each couple of sensors, samples were independently selected on a purely random basis. A statistical analysis was performed to assess the optimal sample size looking for a trade of between computational complexity and statistical significance.

Different sample sizes (in the range between 1,000 and 500,000 pixels) were tested by repeating the extraction 100 times and evaluating the variance of the cross-sensors parameters (described in section 3.6).

Figure 18 shows the analysis performed on the L7 and L8 NDVI pair, here presented as an example. As it can be seen from these plots, the decrease of the

variance with the increase of the sample size is asymptotic and higher number of pixels would result only in an unfruitful increase of the computational burden. The optimal sample size was therefore set to 300,000 pixels which corresponds – for the NDVI index – to a standard deviation of the linear regression coefficients lower than 0.0004 (i.e. intercept equal to 0.0002 and slope equal to 0.0003).

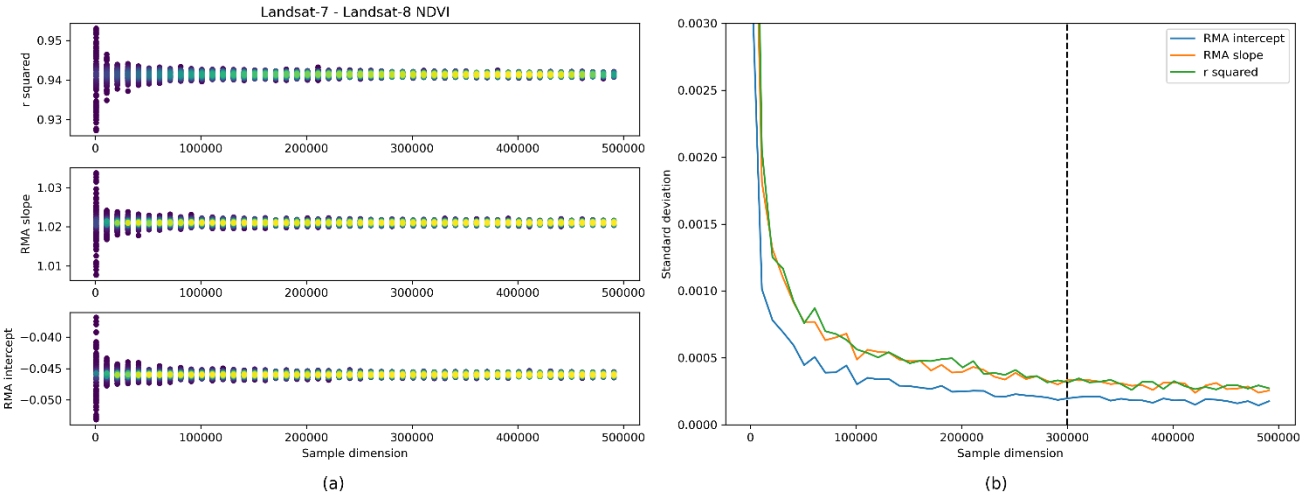


Figure 18. Variation of RMA coefficients for L7 and L8 NDVI image pairs. (a) RMA intercept, slope and r^2 coefficients values are plotted against the sample size; the colour ramp is defined by values frequency (points represented in yellow are those with the most frequent values). (b) Standard deviation of RMA intercept, slope and r^2 coefficients for the 100 random extractions for each sample size.

The case of the comparison between L5 and L7 is singular, because of the exceptionally long period in which both the satellites were contemporary operational. This circumstance offers the opportunity to further analyse the linear relationships, in particular to investigate possible fluctuations of the estimated coefficients during time. For this purpose, further samples of the same size were extracted, one for each year in the period 1999-2011.

4.2.6. Cross-sensors analysis

For each couple of sensors two Ordinary Least Square (OLS) regressions and a Reduced Major Axis (RMA) regression were computed. The OLS

regression allows to find a transformation function from a sensor to the other: the slope and intercept parameters change depending on which variable (i.e., which sensor) is defined as dependent or independent; thus, the OLS regression was performed twice, inverting dependent and independent variable each time, in order to provide transformation functions from a sensor to the other and vice versa (Roy et al., 2016). On the contrary, the RMA regression is performed only once, since the relationship between the interchanged variables can be obtained with a simple algebraic operation (Harper, 2016). In any case, it is assumed that both the dependent and independent variables are subject to errors, which is appropriate because of the possible residual errors that the data may have, such as atmospheric correction and sensor calibration errors (Chastain et al., 2019; Roy et al., 2016).

The goodness of the fit of the regressions was evaluated with the coefficient of determination (r^2), while the significance of the regressions was defined by the overall F-statistic p-value (Roy et al., 2016).

In order to provide an overall measure of similarity between the datasets, three different difference metrics were derived as:

$$\bar{\Delta} = \frac{\sum_i^n v_i^A - v_i^B}{n} \quad (1)$$

$$RMSD = \sqrt{\frac{\sum_i^n (v_i^A - v_i^B)^2}{n}} \quad (2)$$

$$\bar{\Delta}^* = \frac{\sum_i^n (v_i^A - v_i^B) / 0.5(v_i^A + v_i^B) \cdot 100}{n} \quad (3)$$

where $\bar{\Delta}$, RMSD and $\bar{\Delta}^*$ are the mean difference, the root mean square deviation, and the mean relative difference between corresponding values of the generic sensor A and sensor B for n pixels, respectively.

4.3.Results

The results obtained from the comparison of the vegetation indexes derived from different sensors are reported in Table 9-12 and Figure 19-27, and they are organized by couple of sensors: OLI and MSI, ETM+ and MSI, ETM+ and OLI and TM and ETM+. As explained above, for every sensor couple the results are obtained through 100 independent extractions of 300,000 paired observations. These analyses highlighted both differences and similarities between these products and allowed to derive transformation coefficients to be used for a harmonised integration of the different datasets.

4.3.1. OLI and MSI

In Table 9 and Figure 19 the results of the analysis involving the OLI and MSI sensors are presented. Considering the paired observations collected between 2016 and 2020, the lowest mean difference between corresponding indices was found in the NDVI, equal to -0.0008, whilst the highest in NDMI, equal to 0.0245. The RMSD values are quite similar for all the VIs, ranging from 0.0451 (SAVI) to 0.0586 (NDMI). All the regression models are highly significant, all showing r^2 values higher than 0.90 (p-values < 0.0001). In this case the highest deviation from the slope identity is given by the EVI, with an RMA slope value equal to 1.0846. As expected, the computed coefficients of the regression are quite stable in the 100 independent sample extractions, as can be observed by the standard deviations reported in Table 9. Indeed, the slope coefficients of EVI show the highest standard deviation for the regression, having OLI as the independent variable (0.0007 for the OLS and 0.0006 for the RMA).

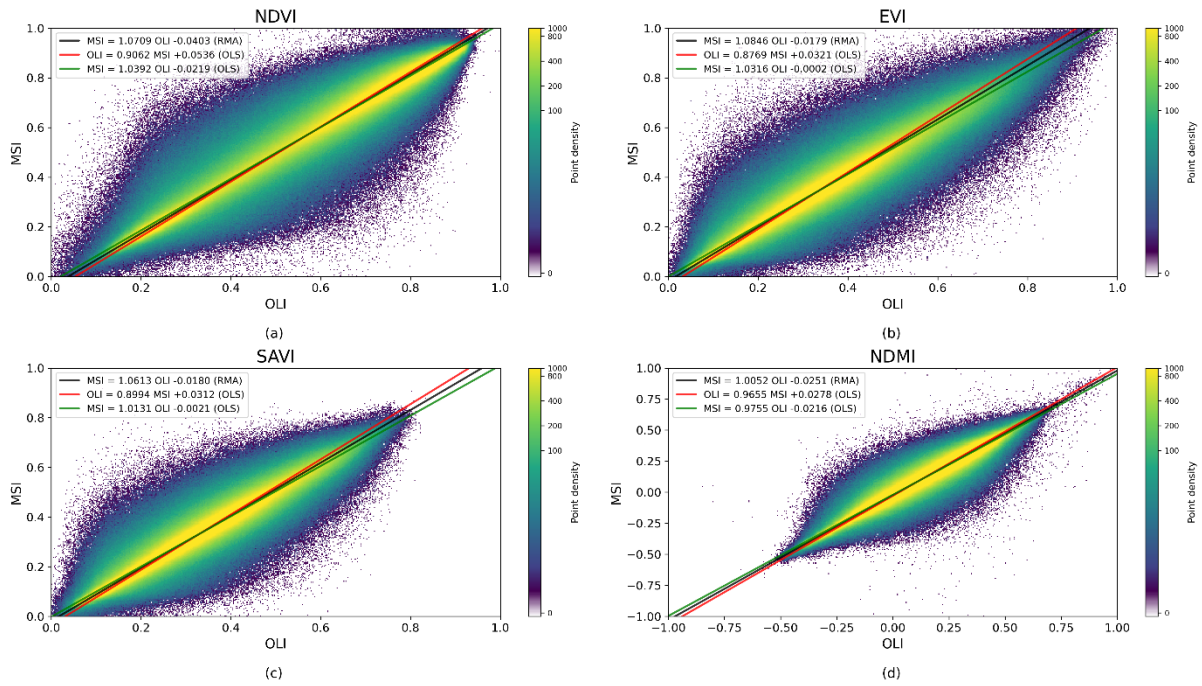


Figure 19. Scatterplots of the VIs for S2 MSI (vertical axis) against L8 OLI (horizontal axis): (a) NDVI, (b) EVI, (c) SAVI, (d) NDMI. The plot colours illustrate the frequency of VIs values with logarithmic scale. The solid lines show the three regression fits.

Table 9. Vegetation indexes sensor transformation functions (OLI to MSI and MSI to OLI): slope and intercept with their standard deviations in brackets, r^2 coefficient, Mean Difference (MD), Root Mean Square Deviation (RMSD), Mean Relative Difference (MRD).

VI	Regression type	Linear transformation functions (slope and intercept)	r^2 OLS	MD (OLI - MSI)	RMSD	MRD (OLI - MSI)
NDVI	RMA	MSI = 1.0709(±0.0004) OLI -0.0403(±0.0003)	0.9418	-0.0008	0.0571	1.8271
	OLS	OLI = 0.9062(±0.0004) MSI +0.0536(±0.0003)				
	OLS	MSI = 1.0392(±0.0004) OLI -0.0219(±0.0003)				
EVI	RMA	MSI = 1.0846(±0.0006) OLI -0.0179(±0.0002)	0.9046	-0.0104	0.0550	-0.9331
	OLS	OLI = 0.8769(±0.0005) MSI +0.0321(±0.0002)				
	OLS	MSI = 1.0316(±0.0007) OLI -0.0002(±0.0002)				
SAVI	RMA	MSI = 1.0613(±0.0005) OLI -0.0180(±0.0002)	0.9112	-0.0022	0.0451	1.1433
	OLS	OLI = 0.8994(±0.0005) MSI +0.0312(±0.0002)				
	OLS	MSI = 1.0131(±0.0005) OLI -0.0021(±0.0002)				
NDMI	RMA	MSI = 1.0052(±0.0003) OLI -0.0251(±0.0001)	0.9418	0.0245	0.0586	1.2995
	OLS	OLI = 0.9655(±0.0004) MSI +0.0278(±0.0001)				
	OLS	MSI = 0.9755(±0.0004) OLI -0.0216(±0.0001)				

To evaluate the residuals of the transformations, the RMA coefficients were applied to all the sample pixels extracted from the OLI images to compute the equivalent MSI* values. The differences between the transformed VI values (MSI*) and the original values from the paired MSI are then computed and the histograms are shown in Figure 20. The means of these residuals are very low for every index (always lower than 0.00005).

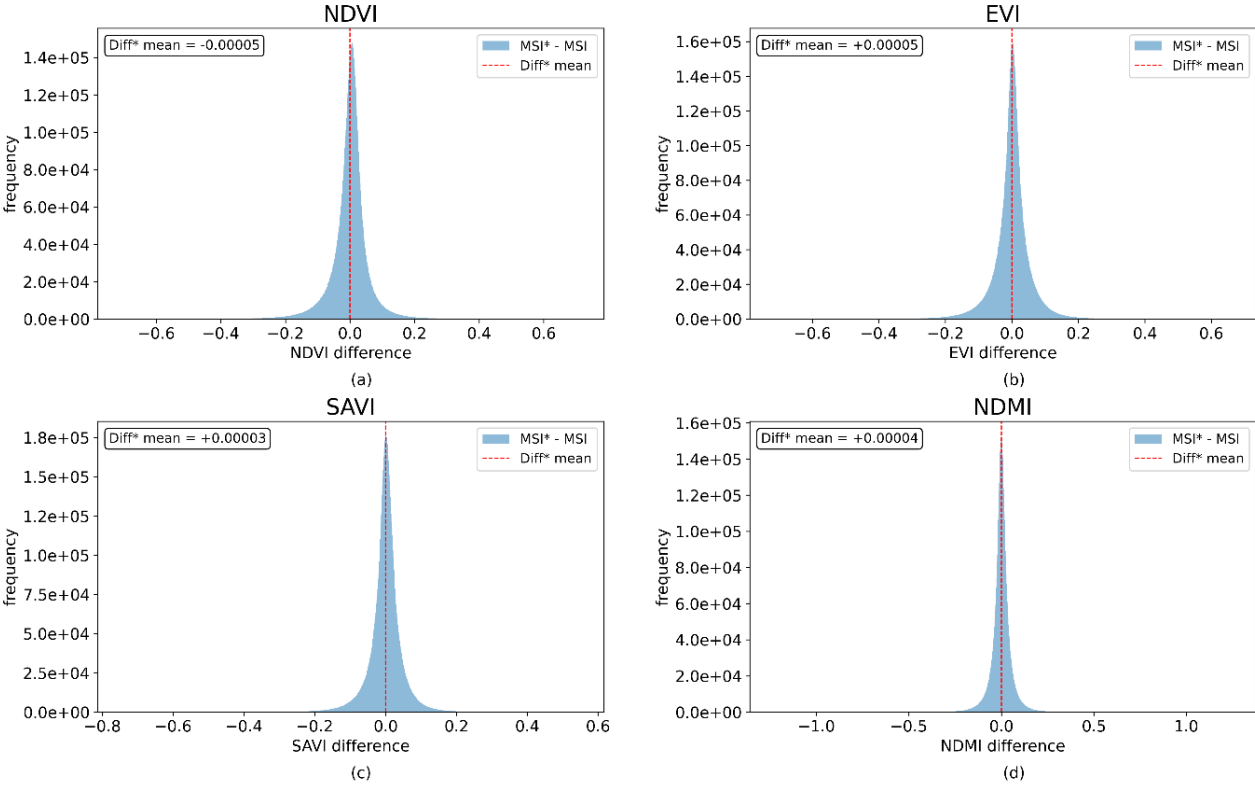


Figure 20. Residuals distribution of MSI and OLI applying the RMA coefficients (OLI independent variable) for NDVI (a), EVI (b), SAVI (c) and NDMI (d). Dashed red lines represent the mean values.

4.3.2. ETM+ and MSI

The comparison between ETM+ and MSI instruments acquisition are showed in Table 10 and Figure 21. The mean difference of the sampled values ranges from -0.0284 (EVI) to 0.0065 (NDMI). The RMSD ranges from 0.0469 (SAVI) to 0.0600 (NDVI). The relative mean difference values are all quite low, ranging from 0.2367 (NDMI) to -7.4047 (EVI). The r² values and p-values

indicate a high significance of the regression models ($r^2 > 0.92$ and p-values < 0.0001). The index with the highest deviation from slope identity is the EVI, with a slope value of 1.1045.

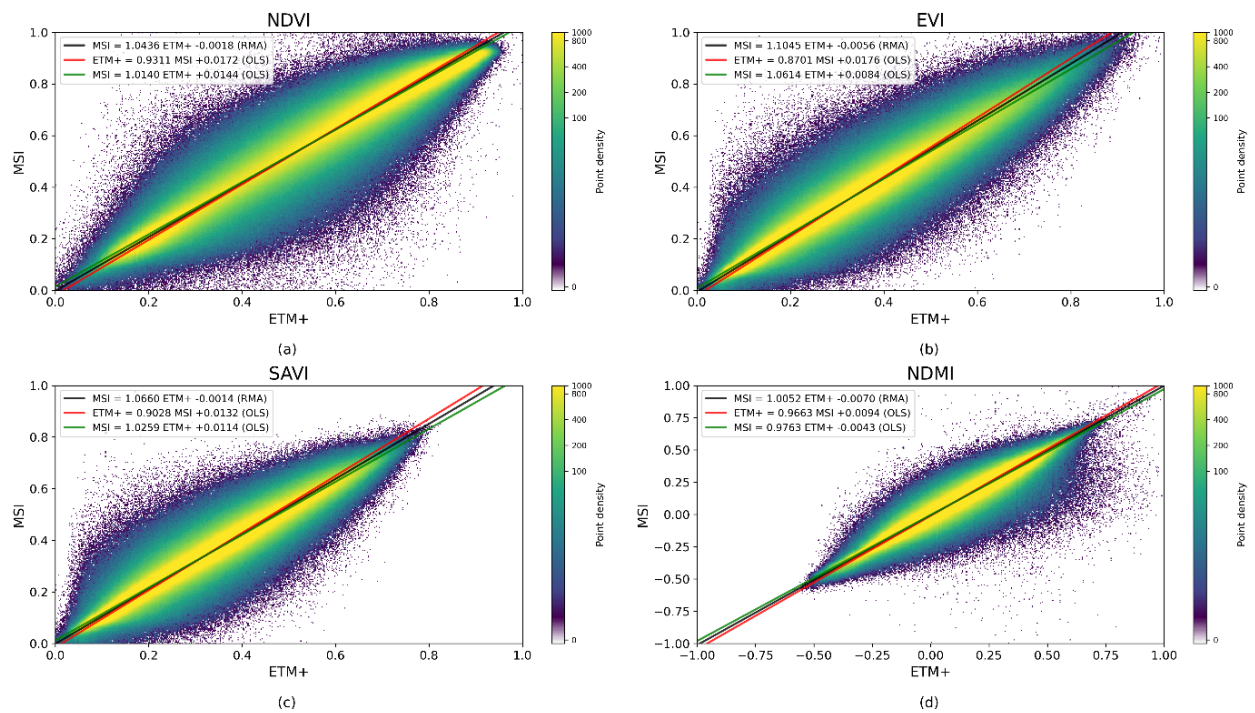


Figure 21. Scatterplots for all of the vegetation indexes for S2 MSI (vertical axis) against L7 ETM+ (horizontal axis): a) NDVI, b) EVI, c) SAVI, d) NDMI. The plot colours illustrate the frequency of occurrence of VIs values with logarithmic scale. The solid lines show the three regression fits.

Table 10. Vegetation indexes sensor transformation functions (ETM+ to MSI and MSI to ETM+): slope and intercept with their standard deviations in brackets, r^2 coefficient, Mean Difference (MD), Root Mean Square Deviation (RMSD), Mean Relative Difference (MRD).

VI	Regression type	Linear transformation (slope and intercept)	functions	r^2 OLS	MD (ETM+ - MSI)	RMSD	MRD (ETM+ - MSI)
NDVI	RMA	$MSI = 1.0436(\pm 0.0004) ETM+ - 0.0018(\pm 0.0003)$		0.9441	-0.0221	0.0600	-3.4924
	OLS	$ETM+ = 0.9311(\pm 0.0004) MSI + 0.0172(\pm 0.0003)$					
	OLS	$MSI = 1.0140(\pm 0.0004) ETM+ + 0.0144(\pm 0.0003)$					
EVI	RMA	$MSI = 1.1045(\pm 0.0006) ETM+ - 0.0056(\pm 0.0002)$		0.9234	-0.0284	0.0588	-7.4044
	OLS	$ETM+ = 0.8701(\pm 0.0005) MSI + 0.0176(\pm 0.0002)$					
	OLS	$MSI = 1.0614(\pm 0.0006) ETM+ + 0.0084(\pm 0.0002)$					

SAVI	RMA	MSI = 1.0660(± 0.0005) ETM+ -0.0014(± 0.0001)	0.9262	-0.0196	0.0469	-5.4098
	OLS	ETM+ = 0.9028(± 0.0005) MSI +0.0132(± 0.0001)				
	OLS	MSI = 1.0259(± 0.0005) ETM+ +0.0114(± 0.0002)				
NDMI	RMA	MSI = 1.0052(± 0.0004) ETM+ -0.0070(± 0.0001)	0.9434	0.0065	0.0534	-0.2367
	OLS	ETM+ = 0.9663(± 0.0004) MSI +0.0094(± 0.0001)				
	OLS	MSI = 0.9763(± 0.0004) ETM+ -0.0043(± 0.0001)				

Also in this case, the RMA transformation was computed on all the samples, using ETM+ observations as independent variable. The residuals distribution and mean values are presented in Figure 22.

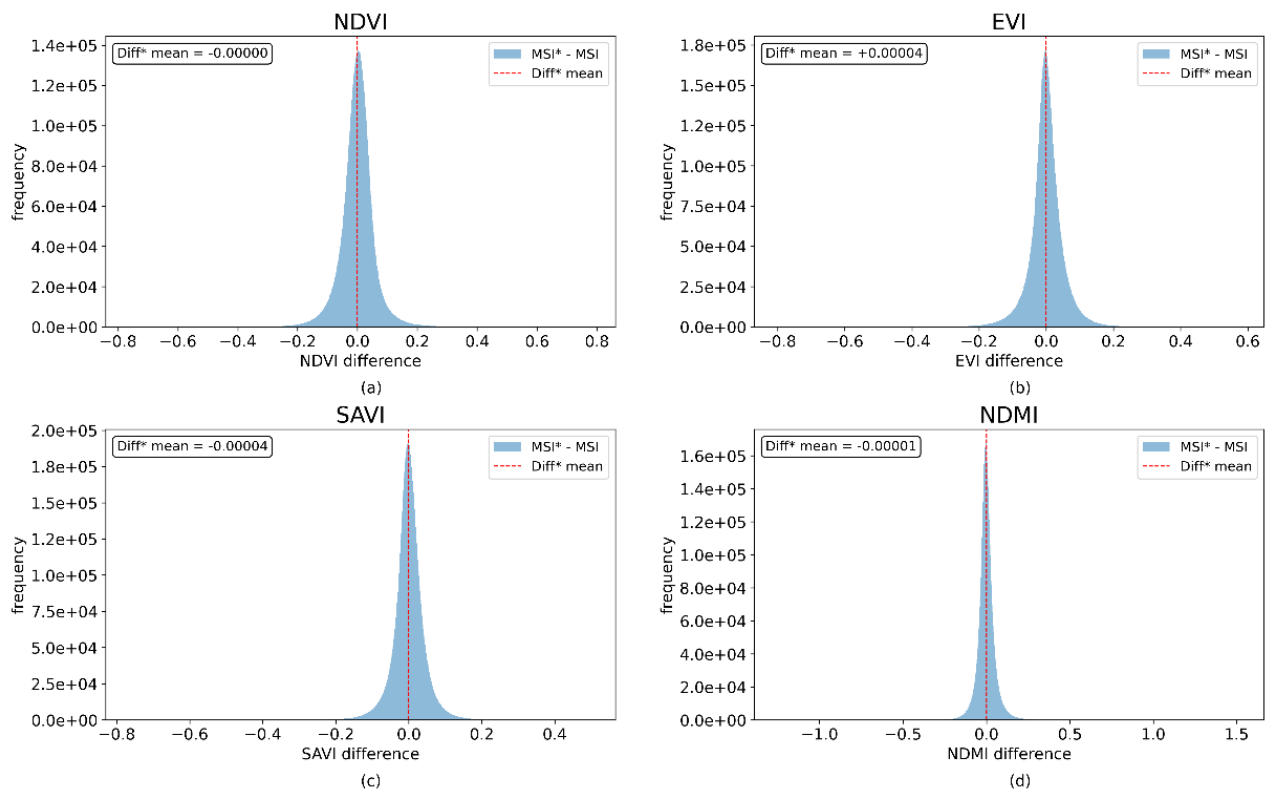


Figure 22. Residuals distribution of MSI and ETM+ applying the RMA coefficients (ETM+ independent variable) for NDVI (a), EVI (b), SAVI (c) and NDMI (d). Dashed red lines represent the mean value.

4.3.3. ETM+ and OLI

The mean differences of the sampled ETM+ and OLI paired observations range from a minimum of 0.0147, for the EVI, to a maximum of 0.0345, for the NDVI. The RMSD values go from 0.0416 (SAVI) and 0.0655 (NDVI), while the

relative mean difference is lower than 9 for all the vegetation indexes (Table 11). The r^2 values are very high for all the regressions, with values higher than 0.93. The significance of the regression is confirmed also by the very low values of the F-statistic p-value (p-value < 0.0001). The highest deviation from the slope identity is given by the NDVI, with a slope value equal to 1.0211. In this case the standard deviations on the coefficients are small (for the slope lower than 0.0007 and for the intercept lower than 0.0003).

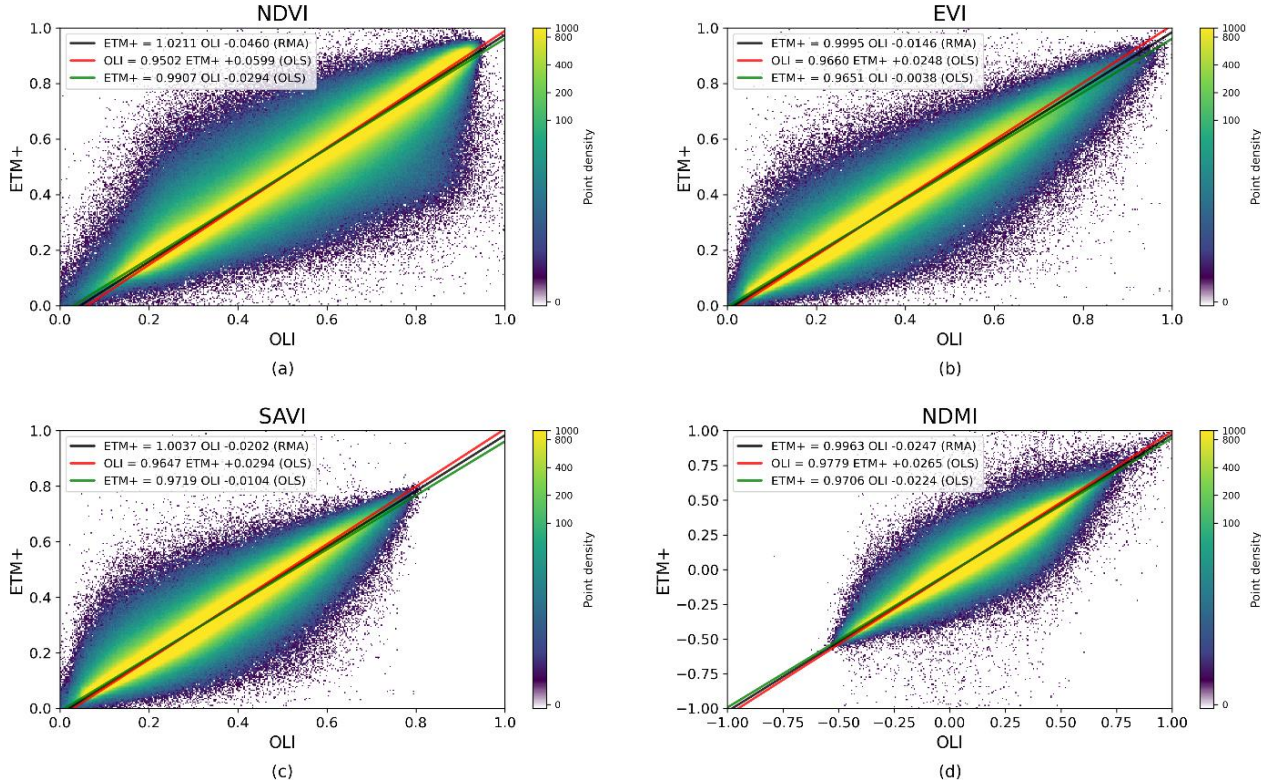


Figure 23 Scatterplots for all of the vegetation indexes for L7 ETM+ (vertical axis) against Landsat OLI (horizontal axis). a) NDVI, b) EVI, c) SAVI, d) NDMI. The plot colours illustrate the frequency of occurrence of VIs values with logarithmic scale. The solid lines show the three regression fits.

Table 11. Vegetation Indexes sensor transformation functions (ETM+ to OLI and OLI to ETM+): slope and intercept with their standard deviations in brackets, r^2 coefficient, Mean Difference (MD), Root Mean Square Deviation (RMSD), Mean Relative Difference (MRD).

VI	Regression type	Linear transformation functions (slope and intercept)	r^2	MD	RMSD	MRD
			OLS	(OLI-ETM+)		(OLI-ETM+)
NDVI	RMA	ETM+ = 1.0211(± 0.0003) OLI -0.0460(± 0.0002)	0.9414	0.0345	0.0655	8.6098
	OLS	OLI = 0.9502(± 0.0003) ETM+ +0.0599(± 0.0002)				
	OLS	ETM+ = 0.9907(± 0.0004) OLI -0.0294(± 0.0002)				
EVI	RMA	ETM+ = 0.9995(± 0.0005) OLI -0.0146(± 0.0001)	0.9324	0.0147	0.0455	6.6034
	OLS	OLI = 0.9660(± 0.0006) ETM+ +0.0248(± 0.0001)				
	OLS	ETM+ = 0.9651(± 0.0005) OLI -0.0038(± 0.0001)				
SAVI	RMA	ETM+ = 1.0037(± 0.0005) OLI -0.0202(± 0.0001)	0.9376	0.0191	0.0416	8.2362
	OLS	OLI = 0.9647(± 0.0005) ETM+ +0.0294(± 0.0001)				
	OLS	ETM+ = 0.9719(± 0.0005) OLI -0.0104(± 0.0001)				
NDMI	RMA	ETM+ = 0.9963(± 0.0003) OLI -0.0247(± 0.0001)	0.9492	0.0251	0.0583	0.2988
	OLS	OLI = 0.9779(± 0.0004) ETM+ +0.0265(± 0.0001)				
	OLS	ETM+ = 0.9706(± 0.0003) OLI -0.0224(± 0.0001)				

Over all the samples, the transformed ETM* was computed by means of the RMA using OLI observations as independent variables. The residuals distributions and mean values are presented in Figure 24.

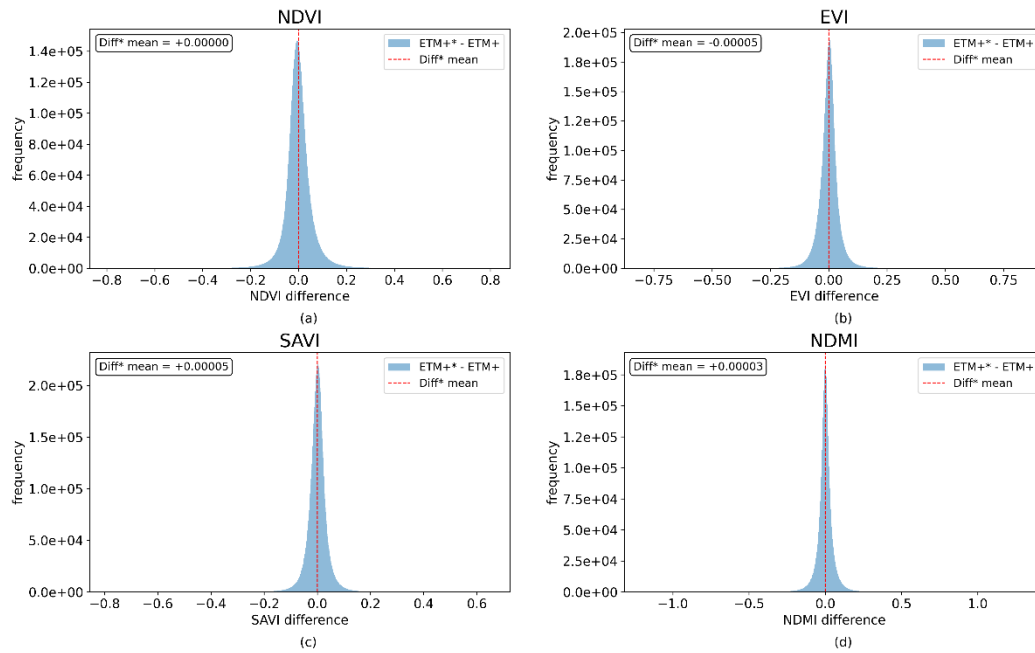


Figure 24 Residuals distribution of ETM+ and OLI applying the RMA coefficients (OLI independent variable) for NDVI (a), EVI (b), SAVI (c) and NDMI (d). Dashed red lines represent the mean value.

4.3.4. TM and ETM+

The results of the comparison between TM and ETM+ are summarized in Table 12 and graphically displayed in Figure 25. The mean difference ranges from 0.0004 (EVI) to -0.0188 (NDVI), the RMSD from 0.0597 (EVI) to 0.0384 (SAVI). The relative mean difference is lower than 4, in absolute value, for all the indexes. All the regression models show a high significance (r^2 values > 0.92 and p -value < 0.0001), and the model parameters are very small in magnitude. The NDVI is the one showing the highest deviation from the slope identity, with a slope value equal to 1.0377.

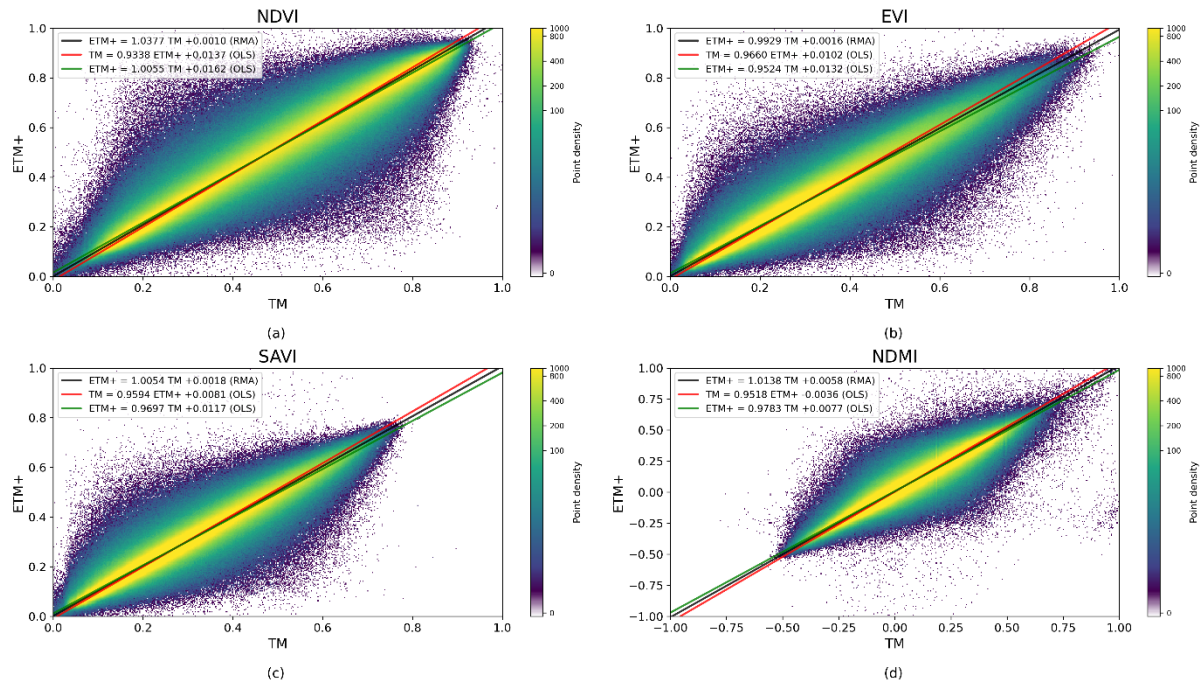


Figure 25 Scatterplots for all of the vegetation indexes for L7 ETM+ (vertical axis) against L5 TM (horizontal axis): a) NDVI, b) EVI, c) SAVI, d) NDMI. The plot colours illustrate the frequency of occurrence of VIs values with logarithmic scale. The solid lines show the three regression fits.

Table 12. Vegetation Indexes sensor transformation functions (TM to ETM+ and ETM+ to TM): slope and intercept with their standard deviations in brackets, r2 coefficient, Mean Difference (MD), Root Mean Square Deviation (RMSD), Mean Relative Difference (MRD).

VI	Regression type	Linear transformation (slope and intercept)	functions	r ²	MD	RMSD	MRD (TM-ETM+)
				OLS	(TM – ETM+)		
NDVI	RMA	ETM+ = 1.0377(±0.0003) TM +0.0010(±0.0002)		0.9389	-0.0188	0.0597	-3.7774
	OLS	TM = 0.9338(±0.0003) ETM+ +0.0137(±0.0002)					
	OLS	ETM+ = 1.0055(±0.0004) TM +0.0162(±0.0002)					
EVI	RMA	ETM+ = 0.9929(±0.0005) TM +0.0016(±0.0001)		0.9200	0.0004	0.0464	0.1843
	OLS	TM = 0.9660(±0.0006) ETM+ +0.0102(±0.0001)					
	OLS	ETM+ = 0.9524(±0.0006) TM +0.0132(±0.0002)					
SAVI	RMA	ETM+ = 1.0054(±0.0004) TM +0.0018(±0.0001)		0.9303	-0.0033	0.0384	-1.2528
	OLS	TM = 0.9594(±0.0005) ETM+ +0.0081(±0.0001)					
	OLS	ETM+ = 0.9697(±0.0005) TM +0.0117(±0.0001)					
NDMI	RMA	ETM+ = 1.0138(±0.0004) TM +0.0058(±0.0001)		0.9312	-0.0066	0.0571	-1.5781
	OLS	TM = 0.9518(±0.0004) ETM+ -0.0036(±0.0001)					
	OLS	ETM+ = 0.9783(±0.0004) TM +0.0077(±0.0001)					

Again, for all the samples the transformed ETM* VIs were computed by the RMA using TM observations as independent variables. The residuals distribution and mean values are presented in Figure 26.

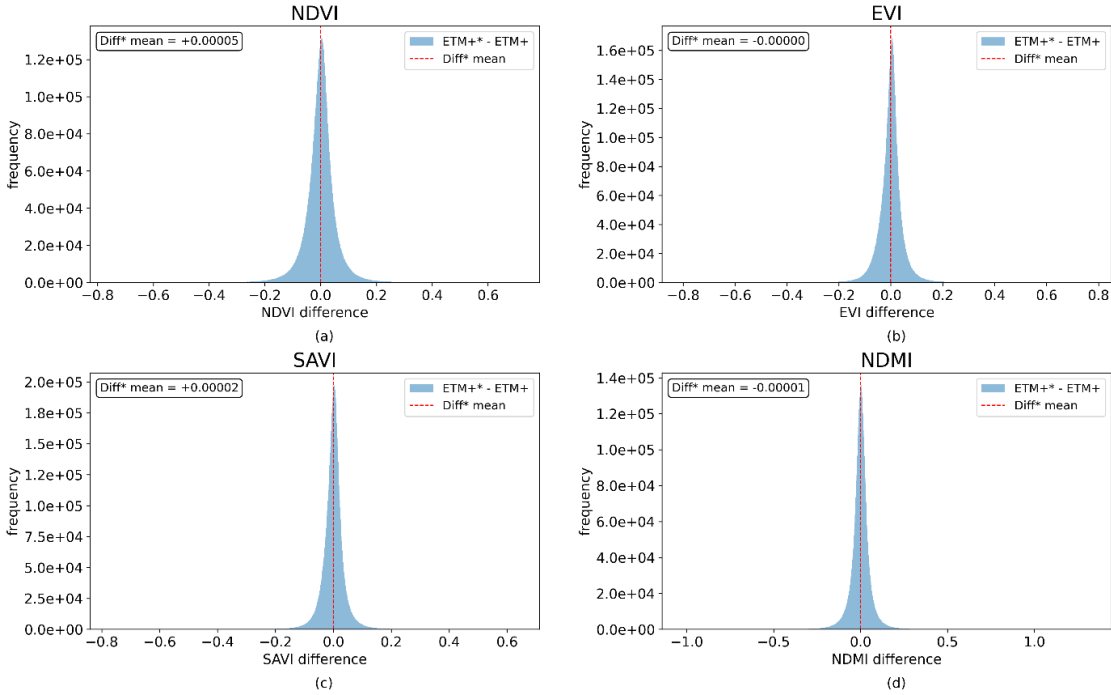


Figure 26 Residuals distribution of ETM+ and TM applying the RMA coefficients (OLI independent variable) for NDVI (a), EVI (b), SAVI (c) and NDMI (d). Dashed red lines represent the mean value.

4.3.5. Time

Thanks to the longer period of contemporary acquisitions of these two sensors, an additional analysis was performed here to investigate the stability over time of the computed parameters for the transformations. Figure 27 shows the intercepts and slopes of the RMA transformations computed for all the VIs, but using 12 samples extracted in different years (between 1999 and 2011). A sensible fluctuation of the values can be noted, even though no apparent trends are detectable.

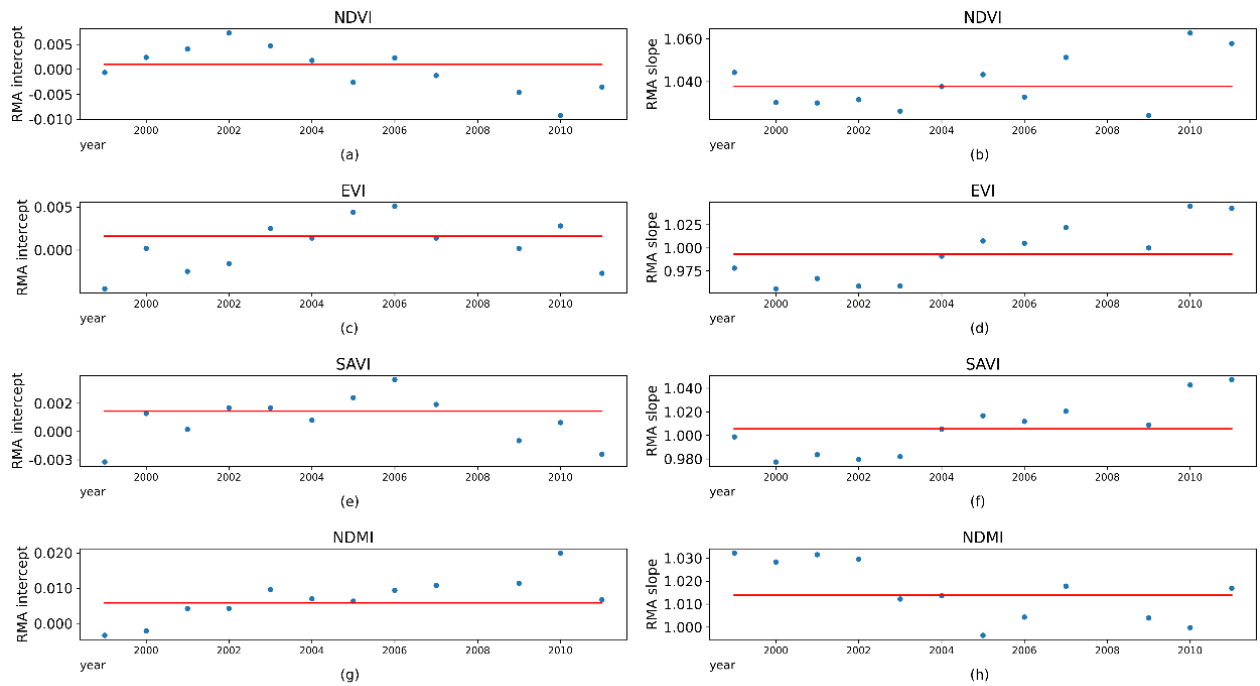


Figure 27. RMA intercept (a, c, e, g) and slope (b, d, f, h) coefficients computed for each VI on yearly samples of L5 and L7 paired observations. The red lines represent the coefficients resulting from the RMA computed within the entire period (from Table 12).

4.4. Discussion

In general, the presented results confirmed the data continuity expected from Landsat Collection-2. Furthermore, the calculated statistics validated its interoperability with the S2 mission. Indeed, the linear regression functions computed for each sensor pair showed a good agreement between the values of the indices, with r^2 always greater than 0.9 and the great majority of pairs falling close to the bisector of the scatter plots. Nevertheless, the application of a transformation seems advisable, when trying assessing changes and detecting anomalies in multi-sensor time-series analyses. Considering for example the NDVI computed on ETM+ and TM (Table 12), a sensible improvement is observed in the MD (from -0.0188 to 0.00005 with the transformation).

Observing the graphs in Figure 19, Figure 21, Figure 23 and Figure 25, two considerations can be made. EVI and SAVI are actually able to reduce noise and

saturation compared to the NDVI. NDVI observations, indeed, are the most disperse with respect to the linear function fits. This is confirmed by the values reported in Table 9, Table 10, Table 11 and Table 12 in which the NDVI difference metrics are higher, compared to the other indices, almost for every sensors pair. Furthermore, EVI and SAVI sample density is higher for lower values of the indexes, while NDVI is more homogeneously distributed along the entire range, showing a great concentration also for very high values of the index. Thus, EVI and SAVI effectively reduce the band saturations visible in NDVI. In addition, the NDVI scatter is the most asymmetric with respect to its linear regression lines: this is especially true when L7 ETM+ is considered. Generally, the NDMI performs similarly to the other indices, despite the fact that the SWIR bands – which are the ones with the lowest overlap in the spectral response function (Chastain et al., 2019) – are involved.

A direct comparison of the coefficients of the linear transformations proposed here with analogous values published in previous works is problematic, because in many cases the estimation is based on limited samples (Li et al., 2013; Mandanici and Bitelli, 2016), or using different regression algorithms (Cao et al., 2022), or on limited timespan (Mancino et al., 2020). On the other hand, the observed RMSEs are similar. The coefficient proposed here are averaged among 100 random extractions of a very large number of pixels and the obtained standard deviations are relatively small, proving the robustness of the solution. For example, a standard deviation by 0.0003 for the slope coefficient of the NDVI in Table 12 means a variation of 0.00015 on the corrected index, when the original value is 0.5.

More sensible fluctuations emerge instead from the analysis performed year by year when comparing ETM+ with TM. Indeed, their entity is one order

of magnitude higher than the standard deviations observed in the 100 extractions over the full period considered as a unique population. Observing the charts of Figure 27, it seems not possible to ascertain a common trend, nor a clear periodical oscillation. One possible justification for these fluctuations may be sought in the orbit drifting of L5. As pointed out by Roy et al. (2020), L5 orbit was not maintained consistently over years, and a temporal pattern of increasing and then decreasing overpass times were observed, as the orbit was adjusted by periodic station keeping manoeuvres. These resulted in changes in the illumination geometry at the moment of acquisition in a place. Anyway, further investigations are necessary to clarify this specific issue.

As a final remark, using all the considered sensors together appears beneficial for two main scenarios: firstly, the creation of a very long TS from 1984 to present (for example for climate change related studies), and, secondly, the generation of a dramatically denser TS henceforth (for near real-time monitoring applications). In both the cases, when assembling the TS including all these sensors, the estimated linear transformations can be used to produce a harmonized dataset. Due to its operational timespan, the authors recommend using L7 as the common reference and harmonizing all the other sensors with it.

Chapter 5

5. Preliminary assessment on Landsat-9 for a combined use

After its successful launch in September 2021 and a calibration period, Landsat-9 data were made available for download for the first time on February 15, 2022. This new dataset increases as never before the number of Landsat-like satellites in orbit, representing a great potential for data availability and suitability for several applications. Indeed, as evidenced by the study of Li and Chen (2020), the combined use of Landsat-9 in a virtual constellation with Landsat-8 still operating and the twin Sentinel-2 satellites allows to reach a 2.3 days revisit time. This achievement is vital for users requiring cloud-free data for monitoring purposes, providing more than three observations per week. Moreover, being a new mission, in order to use Landsat-9 data in a proper and aware way, there is the need for calibration as well as validation of its observations and data products.

Therefore, the present study addressed both the following research questions: the need for assessment of the quality of these observations, together

with the assessment of the consistency within Landsat-9 and its similar ongoing satellite measurements.

In order to achieve these purposes, the present study compared Landsat-9 OLI-2, Landsat-8 OLI and Sentinel-2 MSI observations with *in situ* measurements. In particular, from a practical point of view, the research was designed following two phases, assessing different aspects of the quality and interoperability of these products. Firstly, the assessment was performed by means of spectroradiometer surveys on the ground, collecting spectral signatures in a time window centred at the satellites acquisition time. This analysis was conducted on two test sites in Emilia-Romagna, Italy. Secondly, a cross-comparison analysis of almost synchronous acquisition by S2, L9 and L8 was performed over Europe. Both the study included the Top of Atmosphere and the Bottom of Atmosphere products for evaluation.

5.1. Local comparison with in-field survey

5.1.1. Survey design

Firstly, in order to compare the spectral response of different sensors, one with each other as well as with *in situ* data, a survey campaign was conducted with a spectroradiometer. These surveys took place over specific dates and geographical locations. The areas were selected to be those where the orbits of Landsat-9, Landsat-8 and Sentinel-2A/B overlapped. In addition, the selected dates were those where scenes were acquired within a maximum interval of 48 hours by the three instruments, but with only a 24-hour interval between the acquisition of L9 and that of each of the other two. Based on these requirements, and practical and logistic reasons, two areas of interest (AOIs) were selected (Figure 28). These areas are located in the Emilia-Romagna region, one in the

province of Reggio-Emilia and the other is in the area around the city of Ravenna, which includes Adriatic coastal areas. The two AOIs are situated in the Po river valley, which is mainly characterised by intense agricultural activities.

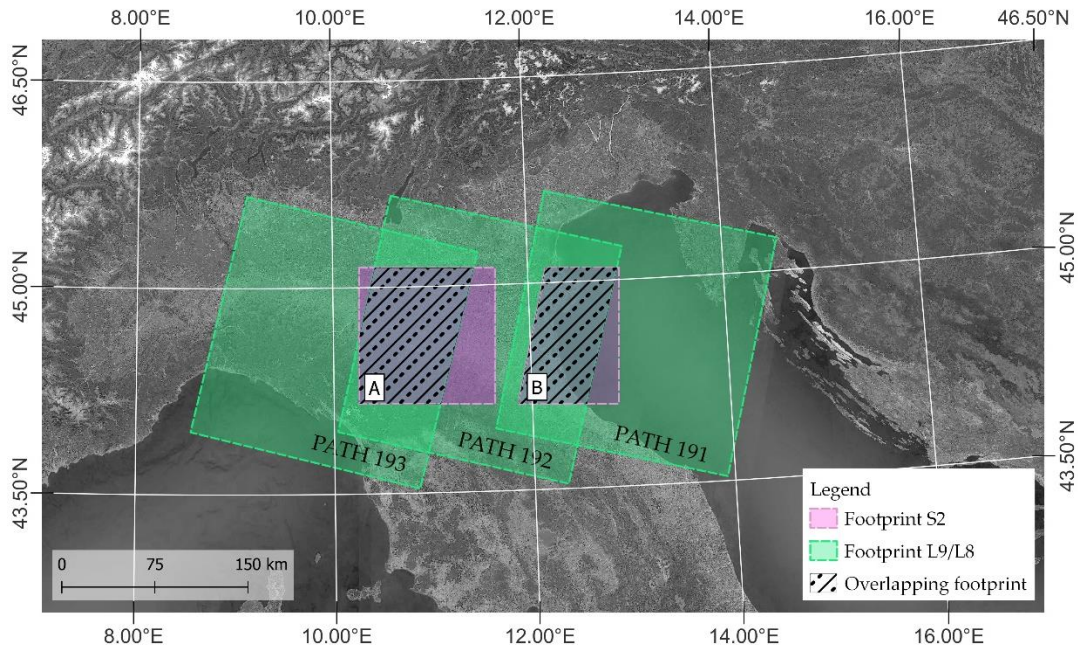


Figure 28 Sentinel-2, Landsat-8/9 overlapping footprint in the Emilia-Romagna region in Italy

Inside the selected overlapping footprints, homogeneous surfaces of at least $120 \times 120 \text{ m}^2$ were identified as possible survey locations. The surface extent parameter came from the need to address the cubic convolution (CC) applied during the orthorectification processing to produce the Level-1 data. Indeed, CC introduces a smoothing effect in the image over a heterogeneous area, by introducing a contamination in the DNs due to heterogeneous surrounding pixels. By isolating $120 \times 120 \text{ m}^2$ surfaces, which corresponds to a 4×4 Landsat pixels, the pixels in the middle should be less affected by this numeric effect. The selected thresholding extent represents a trade-off between having homogeneous surfaces and those actually available in the area: Po river basin is characterized by intense agricultural activity which leads to the high

fragmentation of the countryside. Moreover, the surveys aim to collect the spectral signature of different types of surface, both anthropic and natural. Therefore, a preliminary analysis of the feasibility of the survey was conducted: the different locations, satisfying these requirements, had to be close to each other allowing to reach one site to the other within a time range of a maximum of 2 hours, to meet the temporal window of satellite acquisition. This time window represents a trade-off between the need to limit as much as possible the illumination condition variation and the need of collecting a sufficient number of spectra. Finally, these locations needed to be open and accessible to public. Based on all these requirements, the seventeen points finally selected are shown in Figure 29.

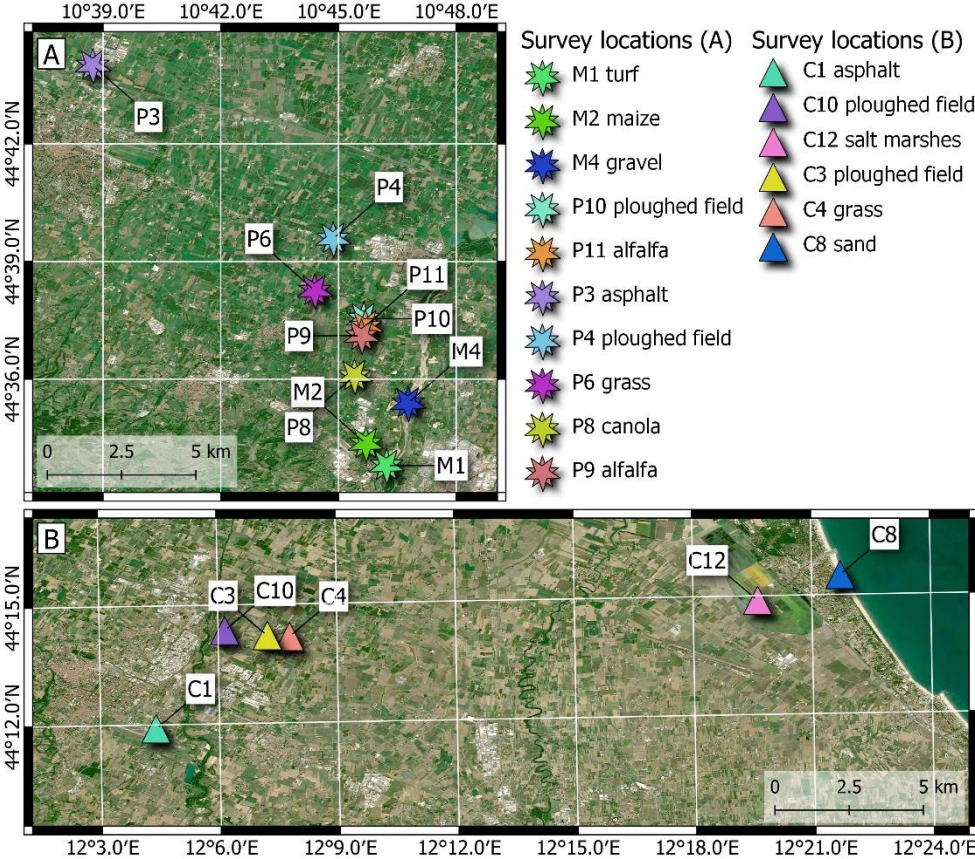


Figure 29 Location of surveys and their land cover.

Table 13 provides a summary of the “Contemporary Overlap Events” (COE) that occurred in the Emilia-Romagna region, i.e. when Sentinel-2, Landsat-8 and Landsat-9 captured the same site within 24h one to the others. COEs reported in Table 13 (where they are identified with a letter) are those when, thanks to cloud-free weather conditions, the spectroradiometer surveys on the field were possible. The campaign was conducted from March to May. For each COE, spectral signatures were collected on the ground in a temporal window of about 2 hours around the satellite’s overpass. Table 14 summarizes the temporal and geographic configuration of the surveys, providing information on the surveyed surfaces.

COE	Zone	Data	Sensor	Orbit id	Path/Row	Time (UTC)
A	Reggio Emilia	4/03/2022	Landsat 9		193/29	10:04
			Sentinel 2	22-T32TPQ		10:10
		5/03/2022	Landsat 8		192/29	09:58
B	Reggio Emilia	28/04/2022	Sentinel 2	22-T32TPQ		10:06
		29/04/2022	Landsat 8		193/29	10:04
		30/04/2022	Landsat 9		192/29	09:58
C	Ravenna	21/03/2022	Landsat 8		192/29	09:58
			Sentinel 2	122-T32TQQ		10:00
		22/03/2022	Landsat 9		191/29	09:52
D	Ravenna	15/05/2022	Sentinel 2	122-T32TQQ		10:00
		16/05/2022	Landsat 9		192/29	09:58
		17/05/2022	Landsat 8		191/29	09:52

Table 13. Contemporary Overlap Events details: date, platform and time of overpass over the same area.

zone	id	Land Cover	Coordinate	COE	Survey time (UTC + 1)	Survey date
Reggio Emilia	M1	Turf	44° 33' 47.809" N 10° 46' 13.427" E	A	11:49-11:57	03/03/2022
	M2	Maize	44° 34' 21.144" N 10° 45' 41.907" E	A	12:11-12:32	03/03/2022
	P3	Asphalt	44° 43' 59.729" N 10° 38' 44.300" E	A	10:45-10:52	04/03/2022
	P4	Ploughed field	44° 39' 34.669" N 10° 44' 51.921" E	A	11:31-11:38	04/03/2022
				B	11:49-11:55	29/04/2022
	M4	Graved	44° 35' 23.309" N 10° 46' 46.399" E	A	10:24-10:43	03/03/2022
	P6	Grass	44° 38' 15.378" N 10° 44' 23.771" E	B	11:38-11:40	29/04/2022
	P8	Canola	44° 36' 4.810" N 10° 45' 24.441" E	B	10:16-10:25	29/04/2022
	P9	Alfalfa	44° 37' 6.201" N 10° 45' 35.210" E	B	10:44-10:51	29/04/2022
	P10	Ploughed field	44° 37' 32.387" N 10° 45' 38.616" E	B	11:07-11:14	29/04/2022
	P11	Alfalfa	44° 37' 20.648" N 10° 45' 41.139" E	B	11:18-11:26	29/04/2022
Ravenna	C1	Asphalt	44° 11' 54.303" N 12° 4' 23.679" E	D	10:27-10:32	16/05/2022
	C3	Ploughed field	44° 14' 12.587" N 12° 7' 14.461" E	C	10:32-10:39	21/03/2022
				D	11:11-11:24	16/05/2022
	C4	Grass	44° 14' 10.775" N 12° 7' 14.461" E	C	10:47-10:53	21/03/2022
	C8	Water	44° 15' 33.202" N 12° 21' 51.319" E	D	12:12-12:16	16/05/2022
	C8	Sand	44° 15' 29.993" N 12° 21' 43.137" E	D	12:00-12:06	16/05/2022
	C10	Carrots	44° 14' 21.412" N 12° 6' 9.982" E	C	10:16-10:22	21/05/2022
D				10:51-10:56	16/05/2022	
C12	Salt marshes	44° 14' 52.927" N 12° 19' 37.731" E	C	11:34-11:49	21/05/2022	

Table 14 Contemporary Overpass Event (COE) with location, date (dd/mm/yyyy) and time (UTC +1) of surveys

5.1.2. Spectroradiometer Survey

The spectroradiometer used in the survey is the SVC HR-768i by Spectra Vista Corporation. The instrument records spectra in the wavelength range between 350 and 2500 nm with a high spectral resolution (768 channels). Details about the instrument characteristics can be found in Figure 30a and in (Spectra Vista Corporation - SVC, 2019)

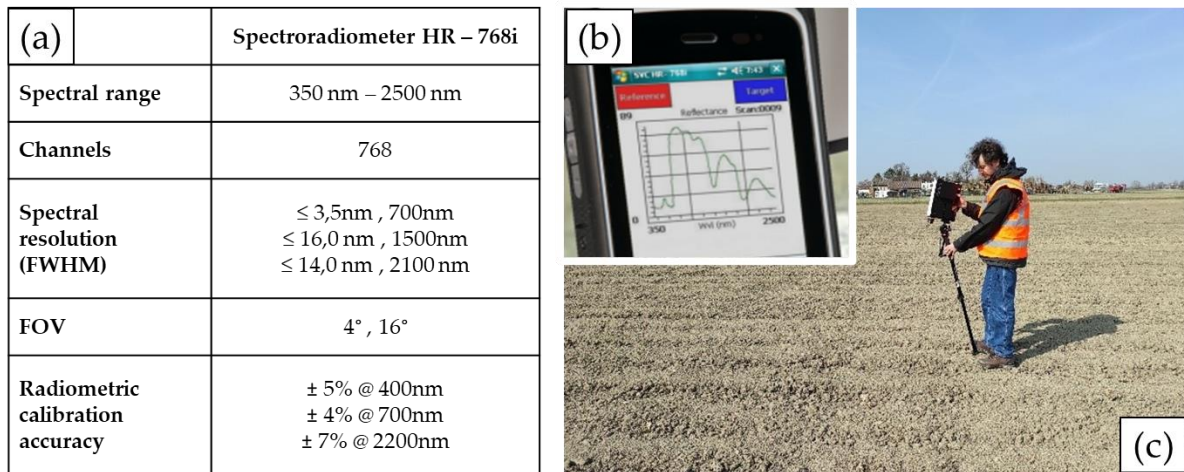


Figure 30 a) Spectroradiometer SVC HR-768i specifications; b) spectral signature as recorded by the spectroradiometer and displayed in the associated device; c) in situ measurement over an ploughed field

For every location, several measurements were performed. Firstly, at the beginning and at the end of every measurements set, the spectral response of a specific calibrated panel with known scattering properties diffusion was recorded. The panel is made of Spectralon, a fluoropolymer with a very high reflectance close to 100% in all the wavelengths range of interest. It represents a good approximation of a Lambertian surface. This operation is vital to retrieve illumination conditions needed in the post processing to compute the surface reflectance of investigated target (Figure 31a). Secondly, four measurements with different inclination in the nadir direction were performed to take into account the BRDF (Roitberg et al., 2022), as shown in the schema of Figure 31b.

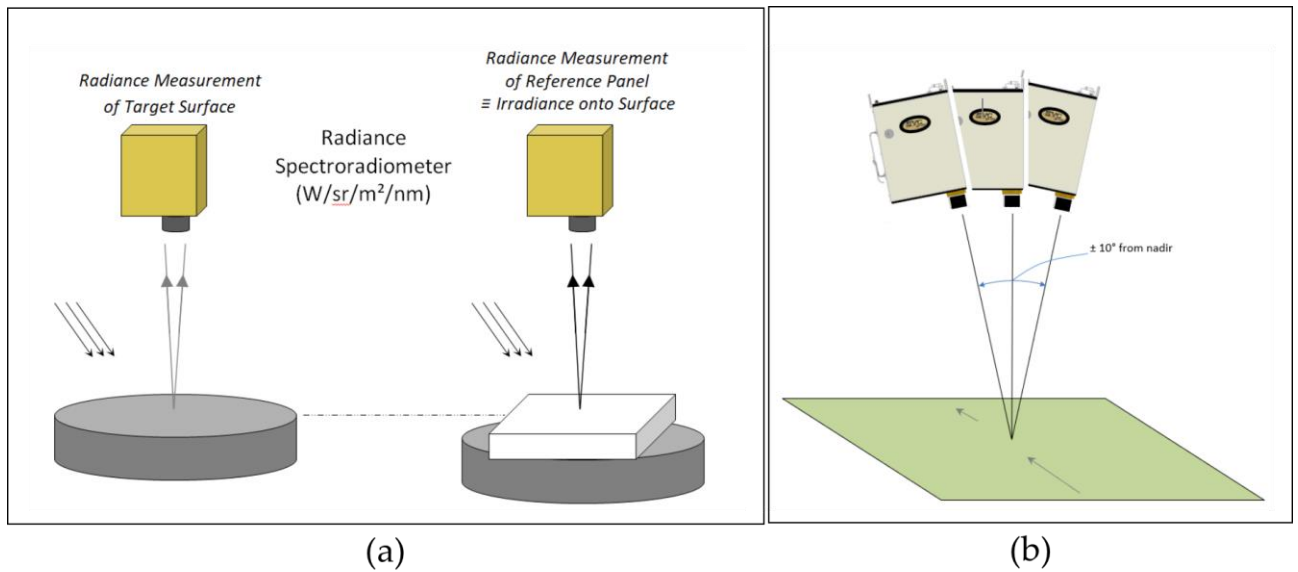


Figure 31 Schematic representation of surveying methodology a) Irradiance measurements using a Radiance spectroradiometer and reference panel; b) schematic example of off-nadir measurements for bi-directional reflectance factors. Source: (Spectra Vista Corporation - SVC, 2019)

5.1.3. Spectral signature processing

The collected spectral signatures underwent some pre-processing. The spectral reflectance of the target is obtained by dividing the radiance measured directly on the target surface by the one measured onto the reference panel (Figure 31a). The so obtained spectral signatures were resampled to the spectral resolution of Landsat-9 OLI-2, Landsat-8 OLI and Sentinel-2 MSI, using the relative spectral response function of the sensor. In Figure 32 an example of the resampling results is shown. This procedure allows to compare these *in situ* measurements with satellite observations, in particular the Level-2 images which provide atmospherically corrected information (i.e. as if they were collected on the ground and atmosphere in the sun-target-instrument path was not present). The spectral angle mapper (SAM) was used to quantify the similarity between the spectroradiometer derived signatures with the signatures extracted from the pixels in the image corresponding to the same location (Kruse et al., 1993). Indeed, the signatures extracted from the image

were compared with every spectra acquired on the ground, computing a SAM for every inclinations of the instrument (Figure 31b). The SAM algorithm calculates the angular distance between two positional vectors, which synthetize the two spectral signatures in the feature space. The smaller this angle, the more similar the two compared spectra are.

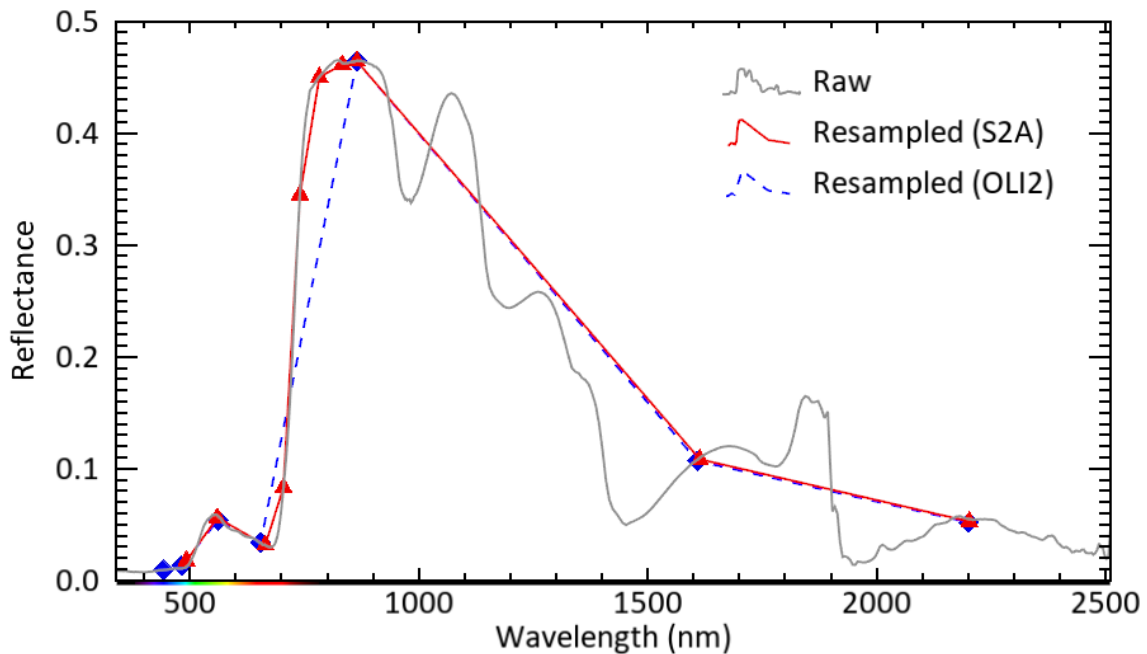


Figure 32. Spectral resolution of in situ measurements against the Landsat-9 and Sentinel-2 instruments. Comparison of the spectral signature originally recorded by the spectroradiometer (grey line) with its resampling as if it was collected by the OLI-2 (dashed blue line) and the MSI sensor (red line).

5.1.4. Image-to-image preliminary assessment

Moreover, referring to the COE acquisitions reported in Table 13, a preliminary image to image comparison was performed to assess the Landsat-9 and Sentinel-2 interoperability. Firstly, the geometric images coregistration was verified. The assessment was performed by automatic tie points generation algorithm based on images correlations statistics. Thanks to the Landsat Collection-2 reprocessing, which rebaselined Landsat GCPs to those provided

in the Sentinel-2 Global Reference Image (as mentioned in Chapter 2), an high consistency was expected (U.S. Geological Survey, 2021b).

Secondly, a first spectral evaluation was conducted by comparing image to image bands differences, considering both TOA and BOA datasets.

5.2. Cross-sensors comparison at continent level

5.2.1. Materials

Landsat-9, Landsat-8 and Sentinel-2 BOA and TOA products were compared. For details about the spectral and geometric characteristics of these dataset, refers to Chapter 1, while information regarding Level-1, Level-2 Surface reflectance products by Landsat and Level-1C and Level-2A products by Sentinel-2 can be found in Chapter 2.1 and Chapter 2.2 respectively. By comparing their spectral characteristics, six band were selected as the most similar to perform the cross-sensors analysis (Chastain et al., 2019). These are Blue, Green, Red, NIR, SWIR1 and SWIR2 bands. Indeed, the percentage of overlap in per-band SRF among the Sentinel-2 MSI and Landsat OLI were estimated as follows by Chastain et al.: Blue 79.2%, Green 99.5%, Red 78.1%, NIR (Band-8a) 98.8%, SWIR1 89.7% and SWIR2 92.2% (Chastain et al., 2019). Table 15 provides a comparison of the spectral wavelength of the considered sensors.

As discussed in Chapter 1 and Chapter 2, the main differences between sensors observations may derive from different geometry acquisition and atmospheric corrections algorithms applied in the Level-2 products. The first is caused by different orbits and sensing times, resulting in measurements of the electromagnetic energy from distinct viewpoints and varying solar illumination conditions. Landsat-8 and Landsat-9 orbit around the Earth at a nominal altitude of 705 km, crossing the equator on the descending node at 10:00 (± 15

minutes) a.m. Mean Local Time (MLT), with a revisit cycle of 16 days each (8 days considering both platforms). On the other hand, the orbit of Sentinel-2 satellites is 786 km high and crosses the equator at 10:30 a.m. (± 15 min) Mean Local Solar Time (MLST) at the descending node (ESA, 2015).

<i>Landsat-8 OLI</i>			<i>Landsat-9 OLI-2</i>			<i>Sentinel-2 MSI</i>		
<i>Bands</i>	<i>Wavelength (μm)</i>	<i>Res. (m)</i>	<i>Bands</i>	<i>Wavelength (μm)</i>	<i>Res. (m)</i>	<i>Bands</i>	<i>Wavelength (μm)</i>	<i>Res. (m)</i>
<i>B2 Blue</i>	0.452 - 0.512	30	<i>B2 Blue</i>	0.45 - 0.51	30	<i>B2 Blue</i>	0.435 - 0.451	10
<i>B3 Green</i>	0.533 - 0.590	30	<i>B2 Green</i>	0.533 - 0.590	30	<i>B3 Green</i>	0.452 - 0.512	10
<i>B4 Red</i>	0.636 - 0.673	30	<i>B3 Red</i>	0.636 - 0.673	30	<i>B4 Red</i>	0.533 - 0.590	10
<i>B5 NIR</i>	0.851 - 0.879	30	<i>B5 NIR</i>	0.851 - 0.879	30	<i>B8a NIR</i>	0.851 - 0.879	20
<i>B6 SWIR-1</i>	1.566 - 1.651	30	<i>B6 SWIR-1</i>	1.566 - 1.651	30	<i>B11 SWIR-1</i>	1.566 - 1.651	20
<i>B7 SWIR-2</i>	2.107 - 2.294	30	<i>B7 SWIR-2</i>	2.107 - 2.294	30	<i>B12 SWIR-2</i>	2.107 - 2.294	20

Table 15. Comparison of the similar spectral bands of the MSI, OLI-2 and OLI instruments

Beside these elements affecting data acquisition, as described in Chapter 2, to produce Level-2 products two different atmospheric correction algorithm are applied involving different ancillary datasets (see Chapter 2 for details). Senitnel-2 Level-2A dataset is produced by means of the Sen2Cor algorithm, while the Land Surface Reflectance Code (LaSRC) algorithm (Version 1.5.0) is used to correct scenes acquired by Landsat-9/8 platforms (Main-Knorn et al., 2017; Vermote et al., 2016a).

Another aspect to point out regards the different initial radiometric resolution due to the quantization of acquired images assigned to each satellite. Indeed, OLI and MSI acquire and store information as a 12-bit digital image, allowing a radiometric resolution per pixel in the range of 0 to 4,095 potential values; while OLI-2 stores information as a 14-bit digital image, increasing resolution of a maximum range of 16,383 values. Finally, all the products are

delivered as 16-bit digital images, redistributing the original DN's in the new range of 65,535 possible values (ESA, 2015; U.S. Geological Survey, 2022a, 2019b). Clearly, in the present study all the images were converted to physical units of reflectance with values ranging between 0 and 1.

In this study were analysed the TOA and BOA datasets available through the Google Earth Engine data catalog (Gorelick et al., 2017). It included: the Landsat-9 and Landsat-8 Collection-2 Tier-1 TOA and Surface Reflectance (SR) as well as the Sentinel-2 TOA and SR harmonized collection. This harmonized collection takes into account the shift in DN introduced with the processing baseline 04.00 and corrects all the new scenes, identified with this baseline, to provide all the images in the archive in the same data range (ESA - European Space Agency, 2015).

In addition to these datasets, the land cover information was included in the analysis. With this purpose, the Dynamic World Land Use Land Cover (LULC) developed by Brown et al. (2022) and available in the GEE data catalog was used. It provides a 10 m LULC map, obtained from the classification of every Sentinel-2 image available from 27 June 2015 to present. In other words, in the GEE catalog there is a Dynamic World LULC layer associated with every S2 image, providing information about the land cover/use on the ground at the time of acquisition of the satellite. The deep-learning classification produces a thematic map with the following classes: water, trees, grass, flooded vegetation, crops, shrub and scrub, built area, bare ground, snow and ice. This dataset was selected for its high spatial resolution and because it provides a LULC temporally coherent with every Sentinel-2 image used in the study.

5.2.2. Methodology

The spectral bands of the OLI-2 were compared with their corresponding ones from both the MSI and OLI sensors (Table 15). The sensors were compared in pairs, by randomly sampling the pixel values from triplets of overlapping images sensed with a maximum delay of one day from the Landsat-9 acquisition, as detailed in the following sections. In order to perform the entire data pre-processing and extraction, a workflow was implemented in the Google Earth Engine (GEE) platform through the Javascript API. While the final statistical analysis on sampled data was performed in Python environment.

5.2.2.1. Study area

The analysis was performed over the entire European continent. The total area was tiled into subregions in order to reduce as much as possible the computational burden. Since the reliability of the SR reflectance products is ensured for a latitude lower than 65° (see Chapter 2), the analysis excluded regions at higher latitude (Figure 33).

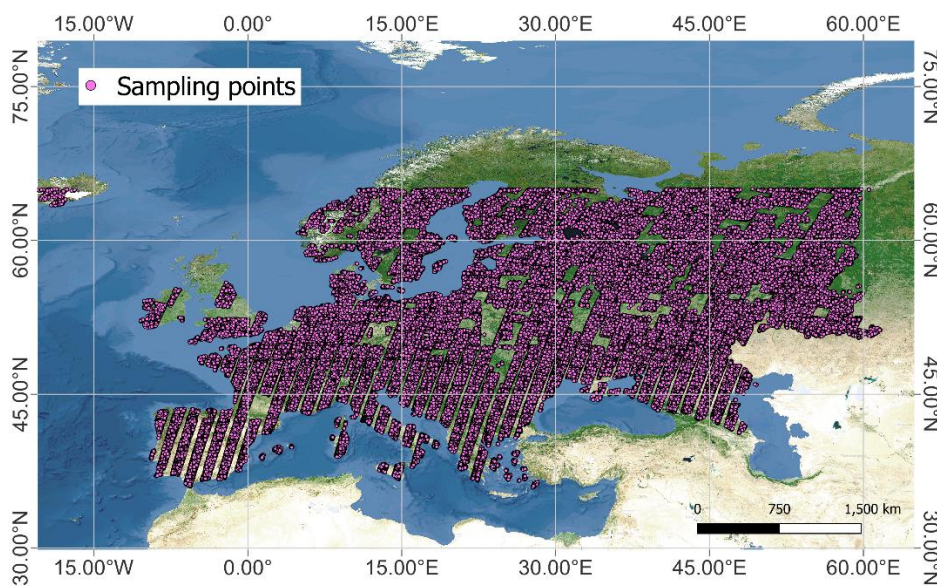


Figure 33 Area covered by the cross-sensors comparison and distribution of random sampling.
Basemap: Sentinel-2 cloudless - <https://s2maps.eu> by EOX IT Services GmbH (Contains modified Copernicus Sentinel data 2020)

5.2.2.2. Data gathering and preparation

The data extraction used for the statistical analysis was performed in the Google Earth Engine (GEE) cloud computing platform (Gorelick et al., 2017).

First of all, the three sensors scenes archives were filtered separately based on metadata information, which includes time, space and cloud cover. For each collection all the images acquired between the 1 February 2022 until December 2022, over Europe, with a cloud coverage lower than 15% were selected. The study was based on the idea of comparing the best scene available, but considering the recent launch of Landsat 9 the analysis had to be restricted to a 11 months period. Therefore, the cloud coverage threshold was increased, when compared with the previous study in Chapter 4, to gather a sufficient number of images in the analysis. See Table 16 for the total records of images available with the time, space and cloud coverage requirements. Moreover, every Sentinel-2 image was joined with the associated LULC provided by the Dynamic World V1 dataset.

<i>Collection</i>	<i>Start</i>	<i>Stop</i>	<i>Cloud cover</i>	<i>Records</i>
<i>Landsat-8 OLI</i>	Feb 2022	Dec 2022	15%	3826
<i>Landsat-9 OLI-2</i>	Feb 2022	Dec 2022	15%	3765
<i>Sentinel-2 MSI</i>	Feb 2022	Dec 2022	15%	48664

Table 16 Records of all Landsat-8/9 and Sentinel-2 images available in Europe, with a cloud coverage lower than 15% from February to December 2022.

At this point, the selected images were pixel-wise masked using the pixel quality assessment (QA) bitmask band. In Landsat Collections, QA layer, obtained with the CFMASK algorithm (details can be found in Foga et al. (2017)), labels the scene pixels as cloud, cloud shadow, cirrus, snow/ice or water, and provides a bit-mapped values output (Foga et al., 2017; Zhu and Woodcock, 2012). This product was used to remove high and medium confidence clouds,

dilated clouds, cloud shadows, high confidence cirrus, snow/ice and water pixels.

The same masking process was performed on the S2 images by means of the Scene Classification map (SCL) quality assessment band, which, likewise the Landsat QA products, labels the pixels on the basis of a classification process and allows to easily perform pixel-wise masking. High and medium probability clouds, cloud shadows, cirrus, water and snow/ice pixels were removed, accordingly with the masking process done for the Landsat products (Louis et al., 2010). In addition, saturated and out-of-range pixels were masked out thanks to the radiometric saturation quality assessment bands and valid value range.

5.2.2.3. *Image pairing, co-registration and reprojection*

Firstly, Landsat-8/Landsat-9 and Sentinel-2/Landsat-9 images were coupled. The images, or portion of images, of two different sensors, filtered and masked as described above, which are spatially overlapping and acquired within 24 hours, were paired, finely co-registered with each other, reprojected, to make sure the images shared the same coordinate reference system, and resampled at Landsat-9 30 m pixel resolution. In fact, in these operations the paired Landsat-9 image was used as reference grid. While Sentinel-2 was resampled by computing the mean values of the original 10 or 20 m pixels, since the land cover band is made of 10 m pixel with integer values identifying thematic classes, the resampling to the coarser resolution of 30 m was performed using the mode statistics.

At this point, an additional mask was calculated to take into account any possible change in land cover that occurred between the two acquisitions of the

paired images (maximum distance of 24 hours). The mask was calculated on the pixel-wise difference in the blue band values, following the methodology proposed by Roy et al. (2016). Pixels with a difference in the blue greater than the 50% of their mean were discarded. It was assumed that such a change in the blue can be caused by surface changes or by the presence of undetected clouds and therefore masked out from the analysis.

Finally, the two paired collections were merged together through an inner join operation, selecting those L8/L9 and S2/L9 pairs sharing the same Landsat-9 image. This resulting collection is made of triplets of images acquired in the same area by Landsat-8, Sentinel-2 and Landsat-9, where L8 and S2 were acquired at a maximum distance of 1 day from the L9 resulting in a total maximum distance of two days in the triplet.

The previously computed mask for the L8/L9 and S2/L9 pairs were multiplied to obtain a single mask that keeps in the analysis only the pixel with valid value in all the images.

5.2.2.4. *Data sampling*

As described for the study presented in Chapter 4, the cross sensors comparison was performed on randomly selected unmasked pixel, instead of using the entire valid pixel population, which would result in an excessive computational burden, samples were independently selected on a random basis. A stratified sampling approach was applied based on the land cover classes, in order to extract a representative sample from each class. The statistical analysis performed in Chapter 4 assessing the optimal sample size demonstrated that significant and stable results are given with a size greater than 250,000 observations. At the end, 30 independent extraction of 270,000

sample pixels were performed. For every pixel, Blue, Green, Red, NIR, SWIR1, SWIR2 bands were gathered for the Landsat-8/9 and Sentinel-2 both TOA and SR datasets.

With the so extracted samples, for each product level (TOA and BOA) bands difference of Landsat-8/9 and Sentinel-2/Landsat-9 of almost synchronous observation were computed and compared.

5.2.2.5. *Cross-sensors analysis*

Following the methodology described in the previous chapter, a cross-sensors analysis was performed between Sentinel-2/Landsat-9 and Landsat-8/9. In this case just the atmospherically corrected products were considered. For each couple of sensors (S2/L9 and L8/L9) two Ordinary Least Square (OLS) regressions and a Reduced Major Axis (RMA) regression were computed. See Chapter 4 for more details about the regression models.

The goodness of the fit of the regression models was evaluated with the coefficient of determination (r^2), while the regressions significance was defined by the overall F-statistic p-value (Roy et al., 2016). The similarity of the sampled pair values was quantifies using the parameters described in Chapter 4: Mean Difference (MD), the Root Mean Square Deviation (RMSD), and the mean relative difference (MRD).

5.3. Example of the impact of harmonization on time series analysis

A final experiment was performed to verify the impact of using harmonization coefficients in a multi constellation time series on an anomaly detection algorithm. The procedure was implemented in GEE and tested in the same area of the COE A, but in this case all the images available were used, with

a cloud coverage lower than 40% and the clouds, cirrus and shadows pixels masked out.

For the pixel corresponding to P3 site (asphalt) a time series (TS) of NDVI including both L9 and S2 imagery was created, one without any harmonization and the other by applying the harmonization coefficient previously computed. P3 was selected to perform the test since it is an anthropic surface which is expected to be coherent through time.

These TS were then analysed with the Bayesian Ensemble Algorithm for Change-Point Detection and Time Series Decomposition BEAST (Zhao et al., 2019). It derives the seasonality and trend components from the TS and it computes the probability of having an abrupt change. Refer to Zhao et al. (2019) for a detailed explanation of the algorithm. In this study, the BEAST was applied to test harmonized and not harmonized TS, by comparing the algorithm's output in terms of the number of detected changing points in the TS and their probability.

5.4.Results

5.4.1. *In situ* survey and local analysis

The image to image comparison has been performed on data summarized in Table 14 for a preliminary assessment of the new Landsat-9 acquisitions on a local scale.

From a geometric point of view, the registration between Landsat-9 and Sentinel-2 contemporaneous acquisition was verified as expected. Two examples are here presented, based on images collected over the Reggio Emilia AOI on the 04 March 2022 and over Ravenna on the 15 (S2) and 16 (L9) May 2022. As summarized in Table 17, the distance in X and Y directions between

the two grids was assessed and resulted in a mean Euclidean distance always lower than the 30 m pixel dimension. This is verified for both the products levels. The worst alignment resulted to be that computed for the S2 and L9 Level-1 acquired in the Ravenna area and quantified in 0.7 pixel. At the same time, for the same pair the shortest distance was registered (0.46 pixel) but with the highest Standard deviation over the entire image. This might be due to the nature of the earth surface captured in the image: a coastal area, where a consistent portion of the surface in the scene is the sea.

Reggio Emilia 04.03.2022	X difference [m]		Y difference [m]		Euclidean distance [m]	
	<i>Mean</i>	<i>Std. Dev.</i>	<i>Mean</i>	<i>Std. Dev.</i>	<i>Mean</i>	<i>Std. Dev.</i>
Level-1 (TOA)	15.13	1.28	-7.94	7.21	18.31	3.24
Level-2 (BOA)	15.17	3.80	-7.89	8.01	18.72	4.54

Ravenna 15-16.05.2022	X difference [m]		Y difference [m]		Euclidean distance [m]	
	<i>Mean</i>	<i>Std. Dev.</i>	<i>Mean</i>	<i>Std. Dev.</i>	<i>Mean</i>	<i>Std. Dev.</i>
Level-1 (TOA)	12.97	7.53	-15.67	2.19	21.06	5.62
Level-2 (BOA)	8.04	5.24	-9.51	8.12	13.75	7.72

Table 17 Results of the coregistration assessment between Landsat-9 and Sentinel-2 image

From a radiometric point of view, the Landsat-9 and Sentinel-2 were compared. Figure 34 compares the Relative Spectral Response Functions (RSRF) in the NIR bands of the Sentinel-2 MSI and Landsat-9 OLI-2 sensors.

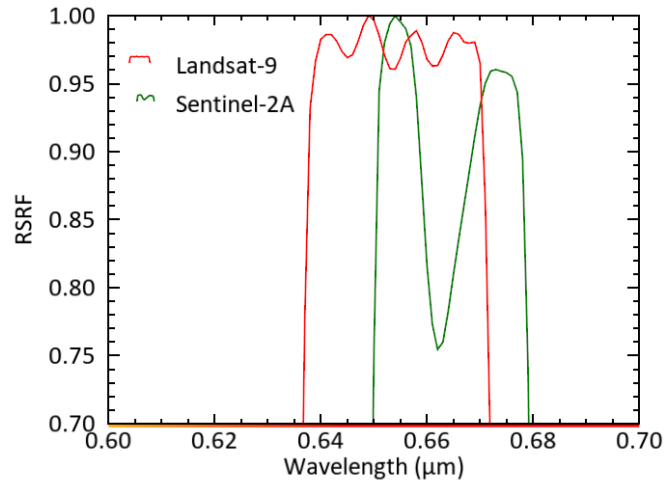


Figure 34 Comparison of relative the spectral response functions in the Red bands of the Sentinel-2 MSI and Landsat-9 OLI-2

Analysing the results obtained from image to image difference on the common bands (Figure 35 shows, as an example, the results for the Red band computed on the S2/L9 images of the 4 March 2022), it can be observed that the difference is higher in the BOA Level-2 products rather than in the TOA ones, since the standard deviation increases. For example, referring to Figure 35, the standard deviation for the BOA difference is twice the TOA one, they are 0.0266 and 0.0160 respectively. As discussed above in this chapter and in previous ones, this is probably caused by different atmospheric correction algorithms, estimating atmosphere parameters from different datasets and introducing discrepancies in the two sensors observations. However these differences can be considered low, and are always lower than the declared radiometric accuracy, which is $\pm 5\%$ for Sentinel and $\pm 3\%$ for Landsat (ESA - European Space Agency, 2022).

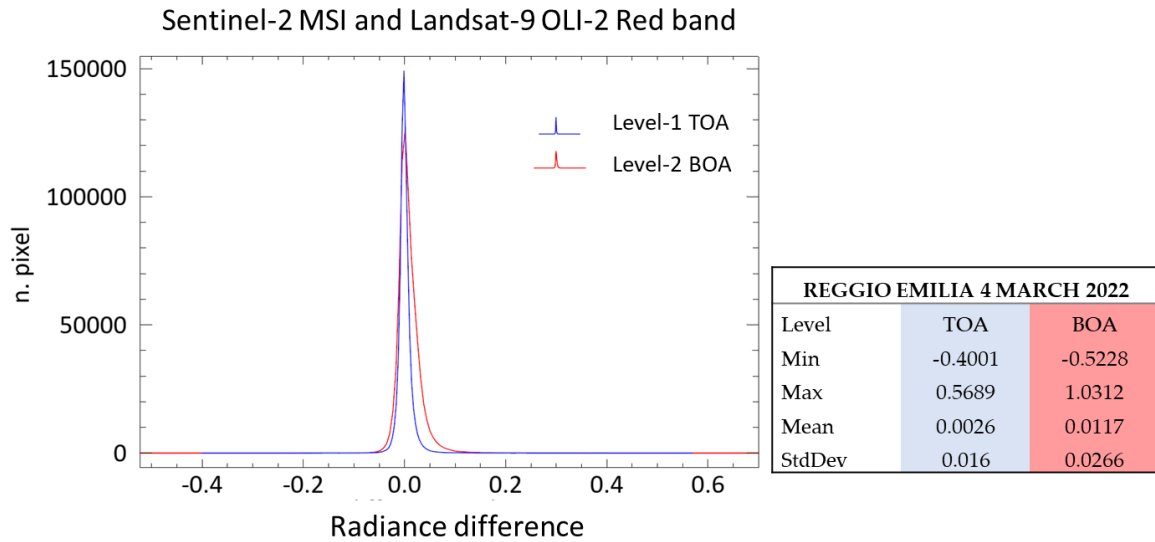


Figure 35. Comparison between difference of Landsat-9 OLI-2 and Sentinel-2 MSI Red band TOA and BOA levels

Regarding *in situ* measurement, the spectral signature collected with the spectroradiometer on the ground were compared with the Landsat-9 and Sentinel-2 Level-2 products acquired at the same time. The Figure 36 shows the results of the SAM computation between spectroradiometer survey and sensors acquisitions. Moreover, the results obtained from Sentinel-2 and Landsat-9 can be compared. The lower the SAM, the highest the similarity between spectral signature measured on the ground and that measured by the satellite. In general, the parameter calculated are low, lower than 0.15. In rare cases, notable differences are registered between sensors, such as in the case of the salt marshes (C12). A possible explanation of this fact can be given by different atmospheric correction. Indeed, looking at the SCL band of the corresponding S2 image, C12 pixels are classified as cirrus; the level-2 generation algorithm may in fact over- or under-correct the reflectance values. An example of cirrus misclassification is given in Figure 37.

Residual differences may be due to different geometry of acquisition and BRDF effects.

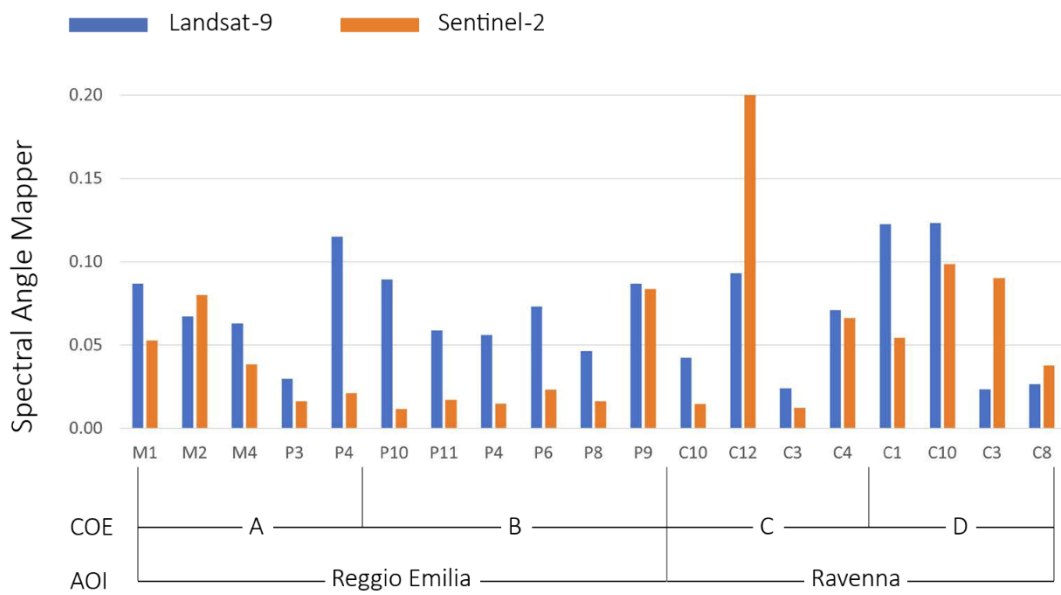


Figure 36. Comparison of the SAM resulted from different surveys and different sensors.

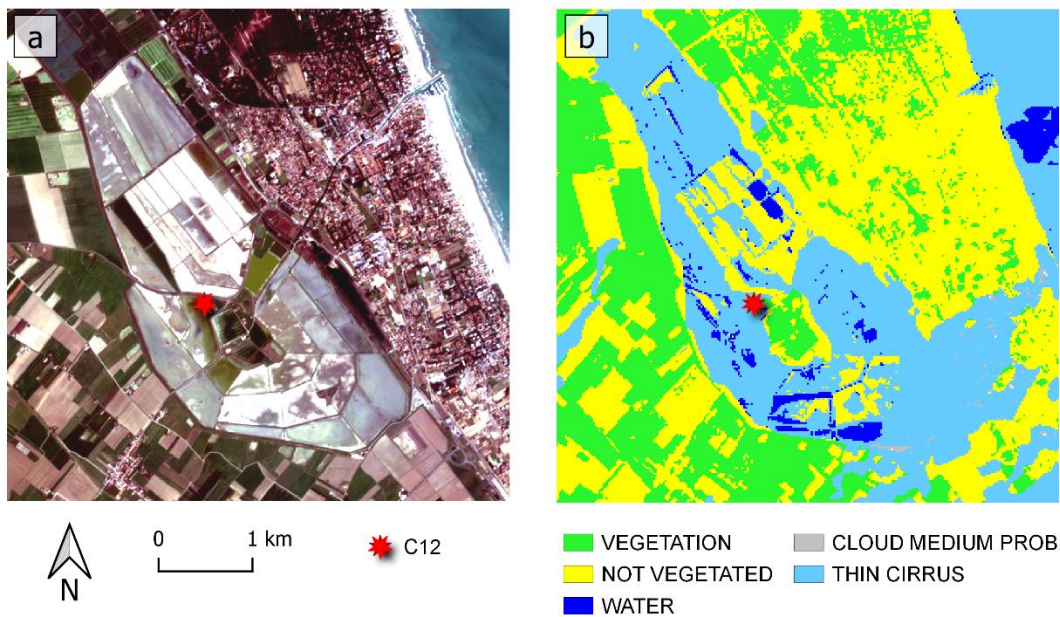


Figure 37 S2 image of the COE C at C12 sample (salt marshes): (a) true color composite, (b) SLC classification included in the Level-2 product. It can be observed that the cirrus class follows the borders of the salt marsh and it is likely misclassified.

5.4.2. European cross-sensors comparison

The results of the cross-sensors comparison between Landsat-9 OLI-2 with Landsat-8 OLI and Landsat-9 OLI-2 with Sentinel-2 MSI on their common bands (Blue, Green, Red, NIR, SWIR1 and SWIR2) are reported in the following tables and figures. As described in the methodology section, the here presented statistics and regression models were computed on a sampling of the entire dataset of almost synchronous acquisition in 2022 all over Europe. Indeed, the results are obtained through 30 independent extractions of at least 260,000 triplets observations, for a total amount of more than 6.8 million of observations. For each band, the linear regression coefficients here reported are the mean value of the parameters estimated in each extraction.

The analyses highlighted differences and similarities between L8, L9 and S2 products, allowing to derive transformation coefficients to be used for a harmonised integration of the three datasets.

Moreover, following the approach used for the image to image comparison at a local scale, using the sample from a single extraction, BOA and TOA differences were computed for triplet observations. In particular L8/L9 and S2/L9 Level-1 and Level-2 products differences were calculated. For a preliminary qualitative assessments histogram of these differences are shown in Figure 38 and Figure 39. The trend highlighted by the analysis performed by subtracting two single images is confirmed by data collected in eleven months and over Europe.

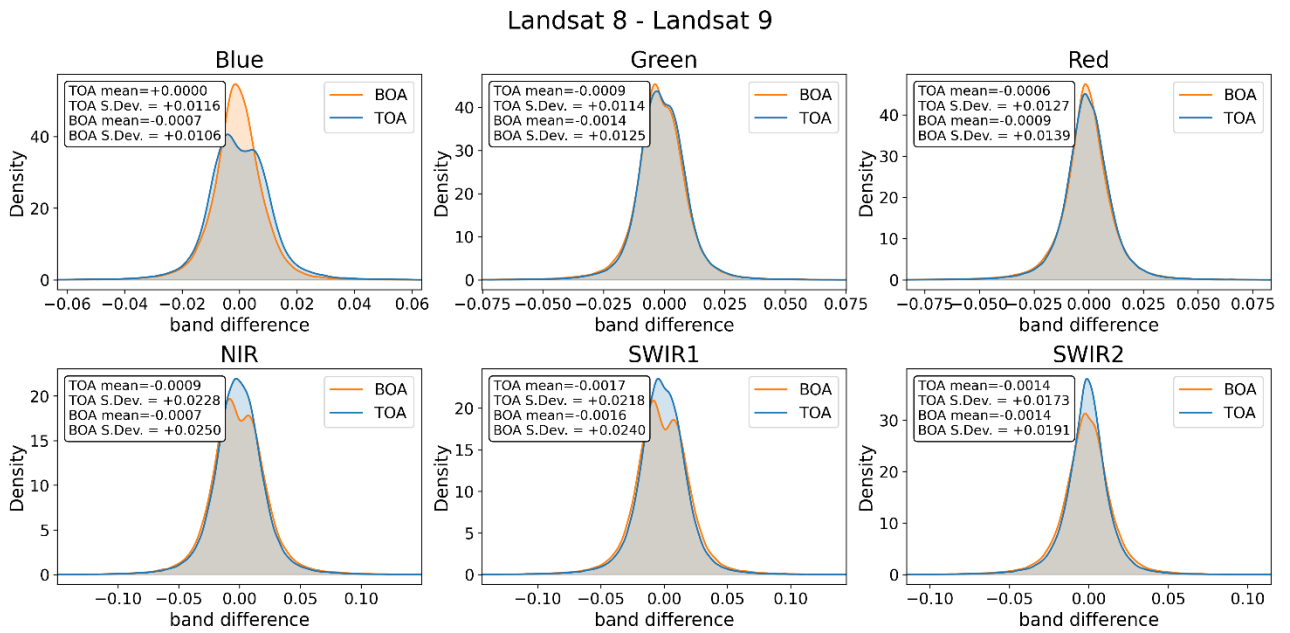


Figure 38 Comparison of band differences between TOA and BOA products by Landsat-8 and Landsat-9 missions

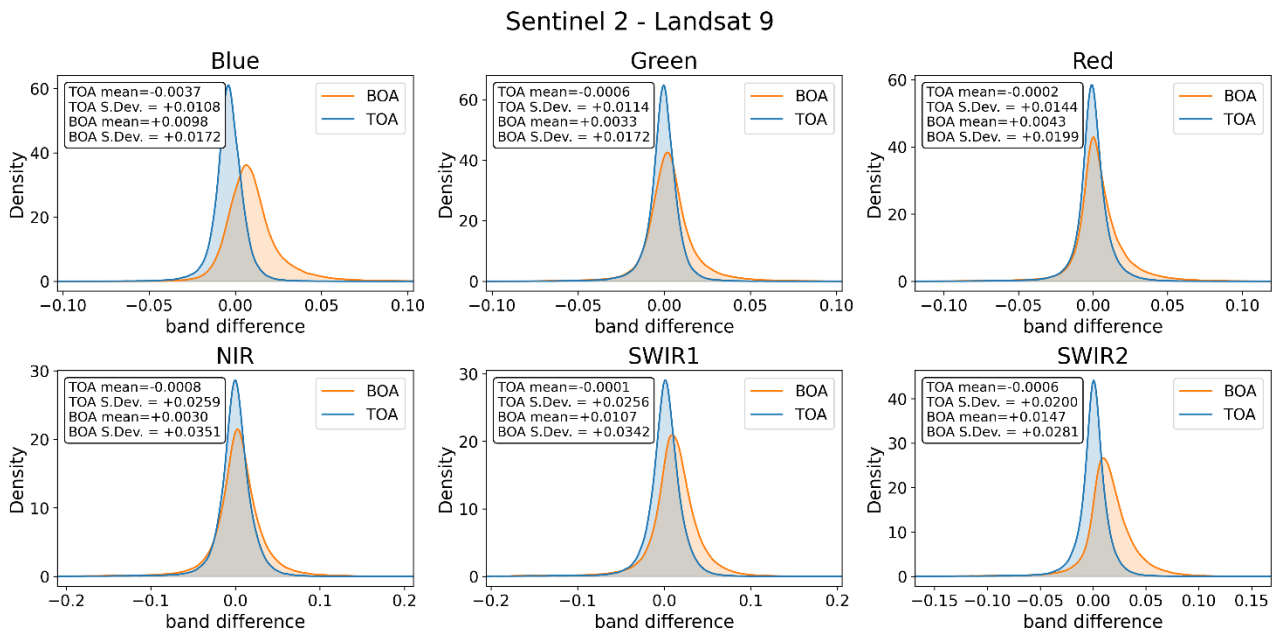


Figure 39 Comparison of band differences between TOA and BOA products by Sentinel-2 and Landsat-9 missions

Furthermore, it is evident the role of atmospheric correction in reducing similarity between data. Although this effect is limited in the Landsat-8/9 comparison, it seems non-negligible between L9 and S2. Moreover, some bands

are more affected than others, such as the Blue, SWIR1 and SWIR2 bands. These bands, indeed, are those more affected by atmosphere elements such as water vapour and aerosol.

However, it is important to remark that the analysis was performed with almost synchronous acquisitions and for this reason the TOA observations are so similar. This is not the case of time series analysis, which covers large time spans, and does require the use of BOA data.

5.4.2.1. *Landsat-8 OLI and Landsat-9 OLI-2*

The results of the cross-sensors analysis are presented in a graphical and numerical way through Figure 40, Figure 41 and Table 18 and Table 19.

To quantify the similarity between the two Landsat datasets, presented visually in Figure 38, the mean difference, root mean square deviation and mean relative difference parameters have been computed. All these coefficients, reported in Table 18, confirm a great similarity between OLI and OLI-2 Level-2 products. The lowest MD value is registered for the blue band, while SWIR1 and SWIR2 dataset have a MD equal to -0.0022 and -0.0018 respectively.

Spectral Band	Mean Difference	Root Mean Square Deviation	Mean Relative Difference
Blue	-0.0005	0.0091	-1.1214
Green	-0.0014	0.0109	0.0109
Red	-0.0010	0.0123	-0.9850
NIR	-0.0013	0.0236	-0.4423
SWIR1	-0.0022	0.0231	-0.9050
SWIR2	-0.0018	0.0184	-1.0219

Table 18 Similarity coefficients computer for sampled pixel from Landsat-8/Landsat-9 image pairs: Mean Difference (MD), Root Mean Square Deviation (RMSD), Mean Relative Difference (MRD).

In Table 19 the results of the linear regression models are summarized. For every band the RMA and the two OLS transformation functions are reported,

with the associated r^2 value. In general, a high level of significance of selected regression models in describing the dataset is found: $r^2 > 0.9$ and p -values < 0.0001 for all the bands. It seems that the best fitting is achieved from the cross-sensor analysis of the red bands, while the worst (r^2 equal to 0.9195) is in the blue linear regression. On the other hand, it is well known that the blue wavelengths can be highly affected by water vapour introducing noise in the sampled paired observations. This effect can be seen also in the scatterplots of Figure 40. Indeed, in Figure 40a, in the scatterplot comparing the blue OLI and OLI-2 band, the paired observations are concentrated around the identity axis just for a very short range of low values. After this low threshold, the paired data points begin to disperse for higher values, drawing a fan shape in the plot.

Landsat-8 OLI – Landsat-9 OLI-2 linear regressions (lat<65°)			
Band	Reg. type	Linear transformation function	R ² (OLS)
Blue	RMA	OLI-2 = 1.0065 (± 0.0018) OLI + 0.0002 (± 0.0001)	0.9195
	OLS	OLI = 0.9527 (± 0.0019) OLI-2 + 0.0021 (± 0.0001)	
	OLS	OLI-2 = 0.9652 (± 0.0017) OLI + 0.0024 (± 0.0001)	
Green	RMA	OLI-2 = 1.0100 (± 0.0015) OLI + 0.0005 (± 0.0001)	0.9340
	OLS	OLI = 0.9568 (± 0.0015) OLI-2 + 0.0024 (± 0.0001)	
	OLS	OLI-2 = 0.9761 (± 0.0014) OLI + 0.0034 (± 0.0001)	
Red	RMA	OLI-2 = 1.0103 (± 0.0012) OLI - 0.0000 (± 0.0001)	0.9570
	OLS	OLI = 0.9683 (± 0.0012) OLI-2 + 0.0021 (± 0.0001)	
	OLS	OLI-2 = 0.9883 (± 0.0011) OLI + 0.0021 (± 0.0001)	
NIR	RMA	OLI-2 = 1.0070 (± 0.0007) OLI - 0.0006 (± 0.0002)	0.9230
	OLS	OLI = 0.9541 (± 0.0007) OLI-2 + 0.0114 (± 0.0002)	
	OLS	OLI-2 = 0.9674 (± 0.0007) OLI + 0.0102 (± 0.0002)	
SWIR1	RMA	OLI-2 = 1.0077 (± 0.0010) OLI + 0.0003 (± 0.0002)	0.9270
	OLS	OLI = 0.9554 (± 0.0010) OLI-2 + 0.0087 (± 0.0002)	
	OLS	OLI-2 = 0.9702 (± 0.0010) OLI + 0.0094 (± 0.0002)	
SWIR2	RMA	OLI-2 = 1.0142 (± 0.0014) OLI - 0.0005 (± 0.0002)	0.9451
	OLS	OLI = 0.9586 (± 0.0018) OLI-2 + 0.0050 (± 0.0003)	
	OLS	OLI-2 = 0.9859 (± 0.0010) OLI + 0.0041 (± 0.0002)	

Table 19 Bands sensor transformation functions (OLI to OLI-2 and OLI-2 to OLI): slope and intercept with their standard deviations in brackets, r^2 coefficient

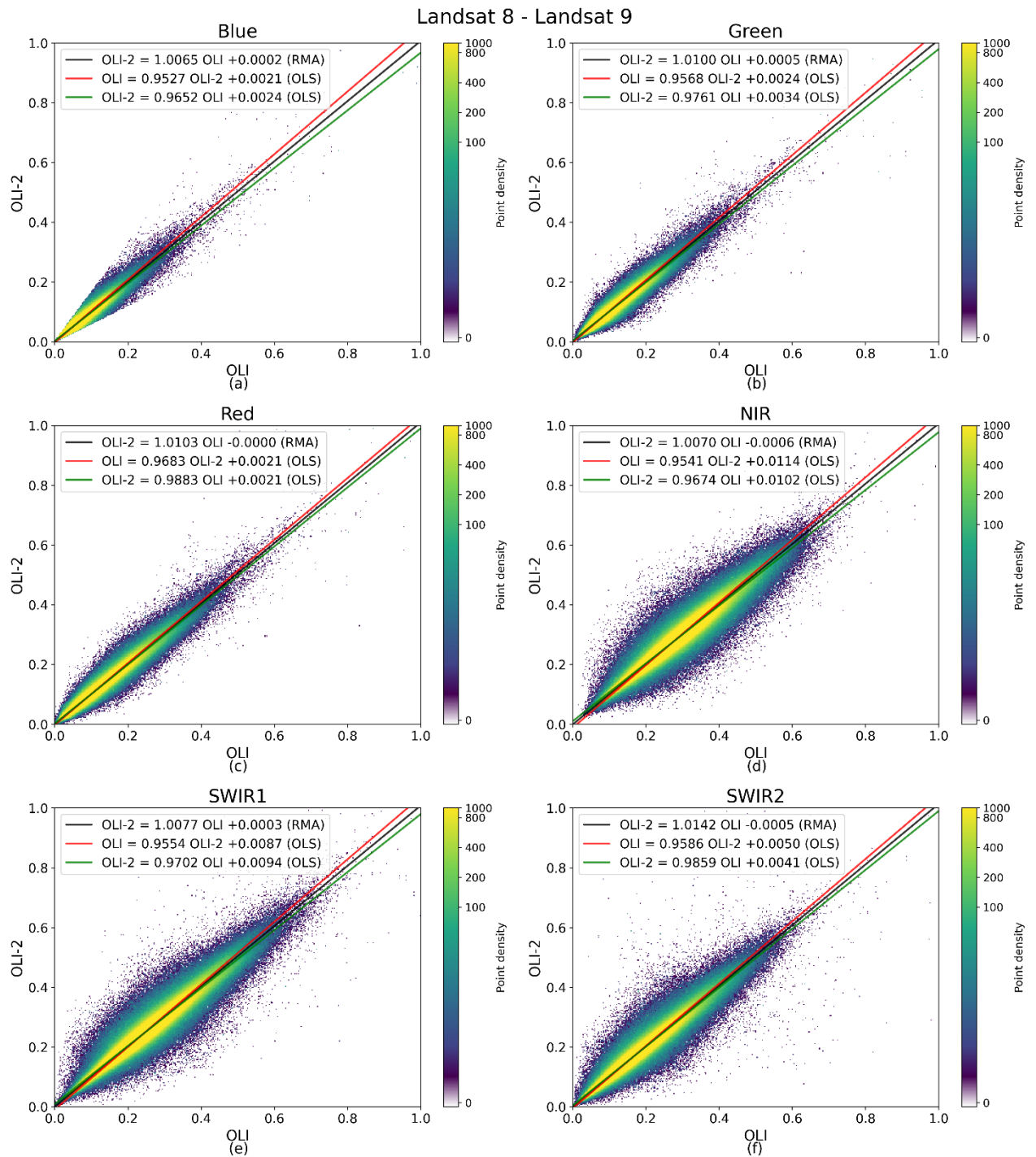


Figure 40 Scatterplots of the reflectance values for L9 OLI-2 (vertical axis) against L8 OLI (horizontal axis) in the a) Blue, b) Green, c) Red, d) NIR, e) SWIR1, f) SWIR2 bands. The plot colours illustrate the frequency of reflectance values with logarithmic scale. The solid lines show the three regression fits.

After the linear regression fitting, the differences between the paired observations were compared. In general, the difference between L8 and L9

observations is very low, and as highlighted in Table 18 the similarity is higher in some bands more than others. This can be seen in the histogram in Figure 41, where the difference between original OLI and OLI-2 paired data are plotted together with the difference between the OLI-2* and OLI-2. OLI-2* is the OLI original observation harmonized to the OLI-2 by means of the computed transformation coefficients (Table 19). Overall, in the cross-sensors analysis performed between the ongoing Landsat satellites it is clear that the two datasets differ just for a very little amount that is corrected by means of the transformation coefficient: see the two almost overlapping histograms for every bands in Figure 41.

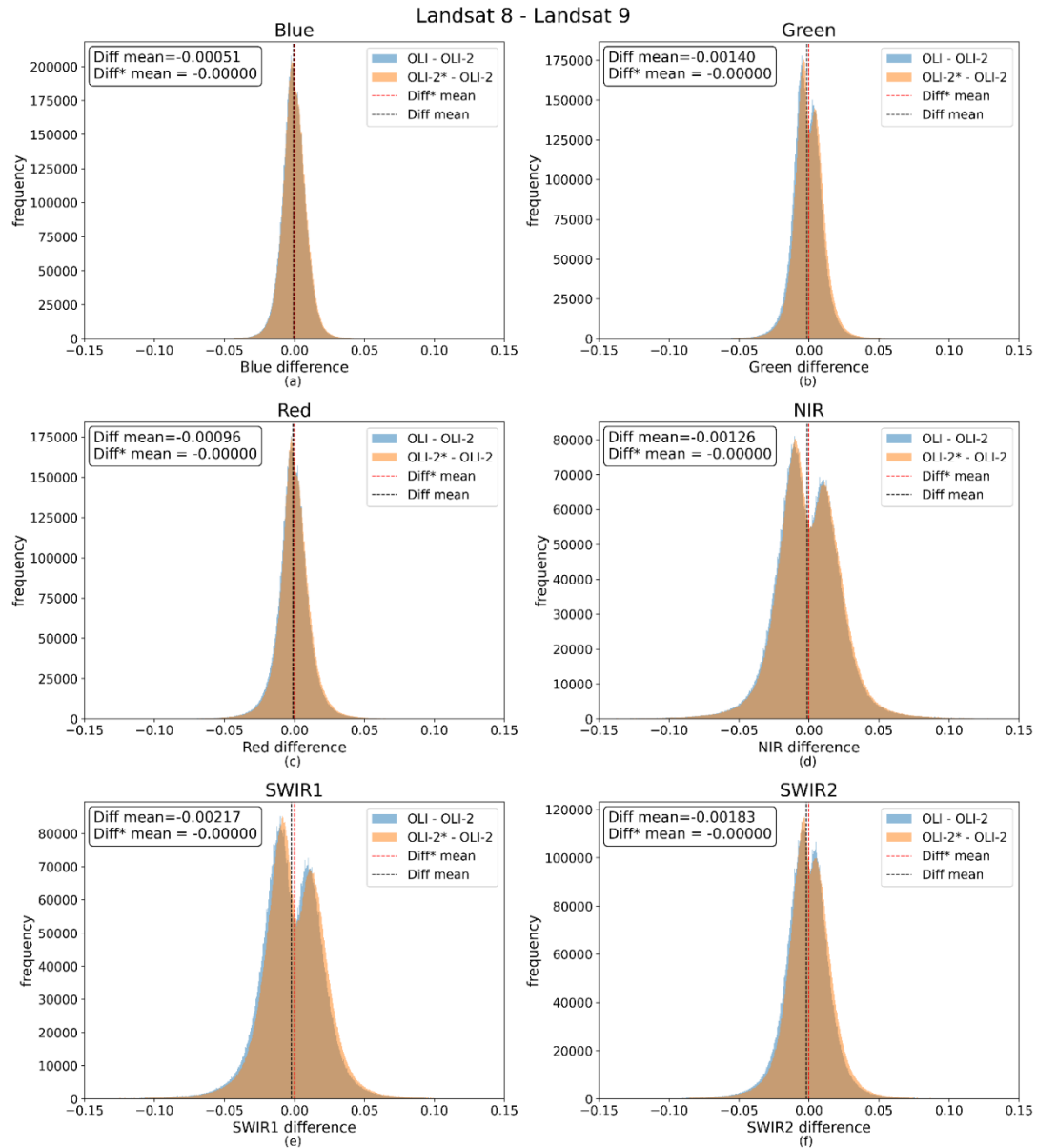


Figure 41 Residuals distribution of OLI-2 and OLI applying the RMA coefficients (OLI-2 independent variable) for Blue (a), Green (b), Red (c), NIR (d), SWIR1 (e) and SWIR (2) bands, compared with the original paired observation differences. Dashed lines represent the mean values.

In conclusion, a very high consistency and similarity between Landsat-8 and Landsat-9 has been demonstrated. This was the expected result of the research, since the two instruments are almost identical in their design and their products undergo the same Collection-2 processing chain. However, this now-verified condition must be monitored throughout the lifetime of the two satellites, as Landsat-8, which is in its 10th year of operation, might be affected

in the next year to possible orbital drifts as it happened to its predecessors (see Chapter 1).

5.4.2.2. *Sentinel-2 MSI and Landsat-9 OLI-2*

In Table 20, Table 21, Figure 42 and Figure 43 the results of the analysis involving the OLI-2 and the MSI instruments by Landsat and Sentinel-2 missions are presented.

The similarity of the paired observations sampled from the available scenes, acquired almost at the same time by Sentinel-2 and Landsat-9 over Europe during 2022, was quantified (see Figure 39 for a qualitative overview) through the MD, RMSD and the MRD coefficients. The computed coefficients for each band are reported in Table 20. In general, a great similarity was revealed. The lowest mean difference between reflectance measurements of corresponding bands was found in the green channel, equal to 0.004, whilst the highest in the blue, equal to 0.0095. The RMSD values are quite similar for all the visible bands, ranging from 0.0174 (blue) to 0.0142 (green), while it increases in the NIR (0.028) and the SWIR bands (up to 0.03 in the SWIR1 channel).

Spectral Band	Mean Difference	Root Mean Square Deviation	Mean Relative Difference
Blue	0.0095	0.0174	13.9572
Green	0.0040	0.0142	2.5506
Red	0.0056	0.0169	2.8360
NIR	0.0049	0.0280	1.5204
SWIR1	0.0138	0.0306	5.6493
SWIR2	0.0178	0.0293	10.5625

Table 20 Similarity coefficients computer for sampled pixel from Sentinel-2/Landsat-9 image pairs: Mean Difference (MD), Root Mean Square Deviation (RMSD), Mean Relative Difference (MRD).

All the results of the linear regressions are reported in Table 21, providing the transformation function needed to harmonize the common spectral bands

of Landsat-9 and Sentinel-2 for a combined use. All the regression models resulted as highly significant, all showing r^2 values higher than 0.90 (p-values < 0.0001). In this case, the r^2 are lower than those obtained for the L8/L9 cross-sensor analysis, however the red band linear regression is the one with the highest significance also in the S2/L9 fitting. On the other hand, as for the L8/L9 analysis, the lower r^2 is registered by the blue band and the same peculiar dispersion in the scatterplot can be seen in Figure 42a.

As expected, the computed coefficients of the regression are quite stable in the 30 independent sample extractions, as can be observed by looking at the standard deviations reported in Table 21. The highest standard deviation on the slope coefficient is registered in the OLS regression of the blue band having OLI-2 as independent variable.

Sentinel-2 MSI and Landsat-9 (lat <65 °)			
Band	Reg. type	Linear transformation function	R ²
Blue	RMA	OLI-2 = 0.7807(±0.0022) MSI +0.0045(±0.0001) (RMA)	0.9004
	OLS	MSI = 1.2154(±0.0037) OLI-2 -0.0022(±0.0002) (OLS)	
	OLS	OLI-2 = 0.7408(±0.0021) MSI +0.0070(±0.0001) (OLS)	
Green	RMA	OLI-2 = 0.8635(±0.0019) MSI +0.0085(±0.0001) (RMA)	0.9324
	OLS	MSI = 1.1183(±0.0026) OLI-2 -0.0063(±0.0002) (OLS)	
	OLS	OLI-2 = 0.8338(±0.0019) MSI +0.0112(±0.0001) (OLS)	
Red	RMA	OLI-2 = 0.8738(±0.0012) MSI +0.0074(±0.0001) (RMA)	0.9544
	OLS	MSI = 1.1180(±0.0017) OLI-2 -0.0059(±0.0001) (OLS)	
	OLS	OLI-2 = 0.8536(±0.0012) MSI +0.0095(±0.0001) (OLS)	
NIR	RMA	OLI-2 = 0.9582(±0.0009) MSI +0.0068(±0.0002) (RMA)	0.9014
	OLS	MSI = 0.9908(±0.0011) OLI-2 +0.0074(±0.0003) (OLS)	
	OLS	OLI-2 = 0.9098(±0.0010) MSI +0.0204(±0.0003) (OLS)	
SWIR1	RMA	OLI-2 = 0.9603(±0.0012) MSI -0.0036(±0.0003) (RMA)	0.9042
	OLS	MSI = 0.9902(±0.0015) OLI-2 +0.0161(±0.0004) (OLS)	
	OLS	OLI-2 = 0.9132(±0.0010) MSI +0.0086(±0.0003) (OLS)	
SWIR2	RMA	OLI-2 = 0.9125(±0.0015) MSI -0.0018(±0.0003) (RMA)	0.9285
	OLS	MSI = 1.0560(±0.0023) OLI-2 +0.0086(±0.0004) (OLS)	
	OLS	OLI-2 = 0.8792(±0.0013) MSI +0.0042(±0.0002) (OLS)	

Table 21 Bands sensor transformation functions (MSI to OLI-2 and OLI-2 to MSI): slope and intercept with their standard deviations in brackets, r^2 coefficient.

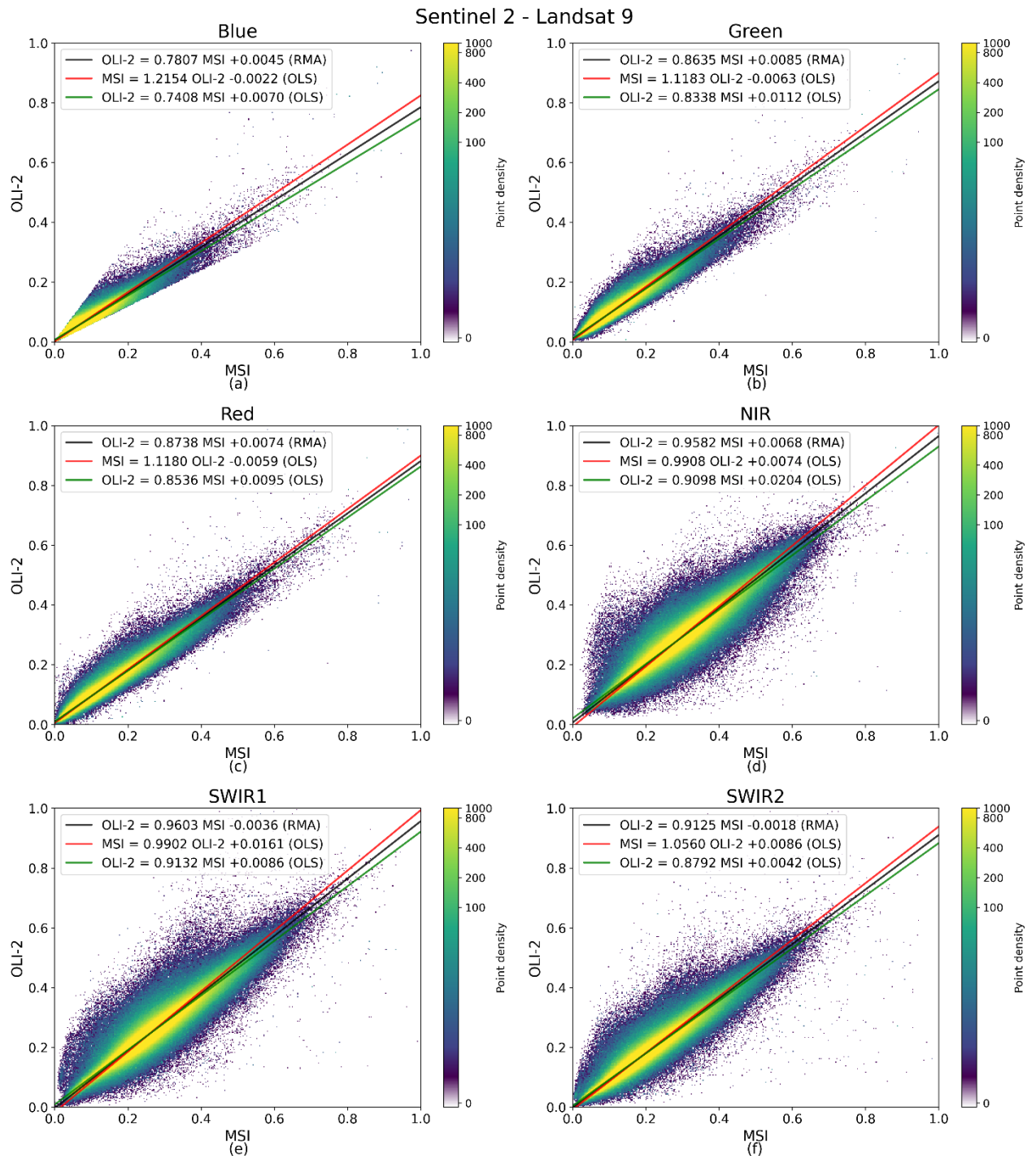


Figure 42 Scatterplots of the reflectance values for L9 OLI-2 (vertical axis) against S2 MSI (horizontal axis): a) Blue, b) Green, c) Red, d) NIR, e) SWIR1, f) SWIR2. The plot colours illustrate the frequency of reflectance values with logarithmic scale. The solid lines show the three regression fits.

In addition to the linear regression fitting, the differences between the paired observations were considered. To evaluate the residuals of the transformations, the RMA coefficients were applied to all the sample pixels extracted from the MSI images to compute the equivalent OLI-2* values. The differences between the transformed reflectance (OLI-2*) and the original OLI-2 values for every band from the paired observations are computed. Those are shown in Figure 43 together with the untransformed paired observation difference (MSI-OLI). This time, the beneficial effect of the harmonisation is more evident, and the use of the transformation coefficients allows to translate the curve and concentrate its values on the null mean axis. The bands which benefit more of this harmonization are the blue and the two SWIR bands.

In conclusion, a good consistency between the two datasets from Landsat and Sentinel mission was verified. The possibility of interoperability was confirmed. Indeed, NIR, Red and Green bands have a good correspondence. However, in the blue and SWIR bands higher differences were registered.

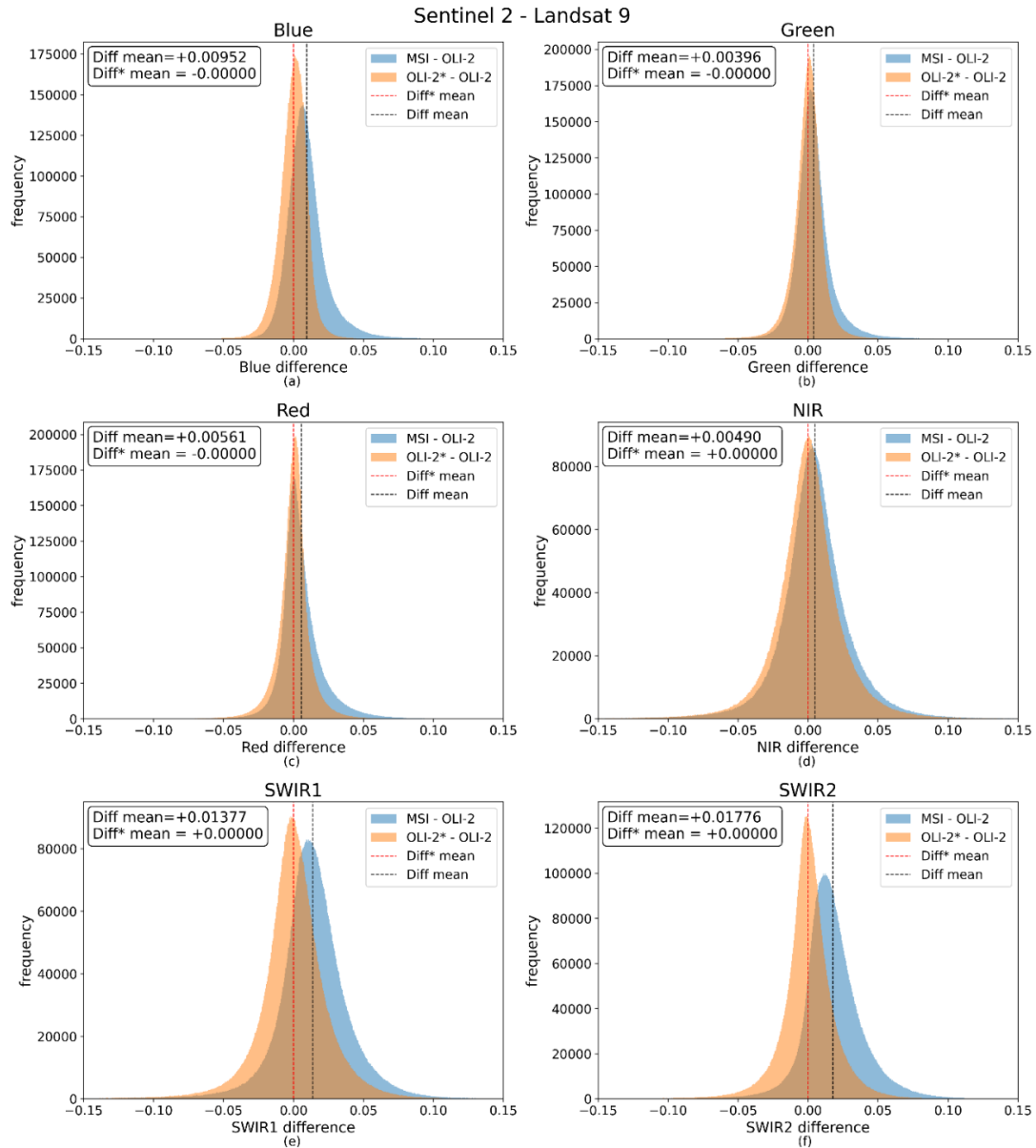


Figure 43 Residuals distribution of OLI-2 and MSI applying the RMA coefficients (OLI-2 independent variable) for Blue (a), Green (b), Red (c), NIR (d), SWIR1 (e) and SWIR (2) bands, compared with the original paired observation differences. Dashed lines represent the mean values.

5.4.3. Harmonization example on selected sample

The NDVI TS derived from L9 and S2 images were extracted for P3 site (asphalt surface), since it is expected to be quite stable over time. The BEAST algorithm was applied on both the TS and the Harmonized TS, as described in Section 5.3. Although this algorithm provides an exhaustive time series analysis,

in this case it was used only to assess the impact of harmonization on selected sample. Therefore, for simplicity, only the trend is here considered as example.

In Figure 44 the asphalt case (P3) is shown, comparing the TS and BEAST trend analysis applied on the NDVI L9 and S2 observation before (on the left) and after (on the right) harmonizing S2 values to be as similar as OLI2. The BEAST retrieved a mean trend model and its probability of having changepoints. Focusing on the NDVI TS it is evident that the harmonization reduces the level of noise in the series, allowing the BEAST algorithm detecting the 15-10-2022 S2 observation as a change point with a probability of 80%. Clearly this is not a real change, but it can be interpreted as an anomaly in the TS. Checking the corresponding image, indeed, it resulted to be affected by clouds that remained undetected by the cloud mask. Reducing noise in the TS is the first benefit of harmonization, allowing also the detection and removal of anomalous values. This is more evident and effective when analysing data with low magnitude dynamics.

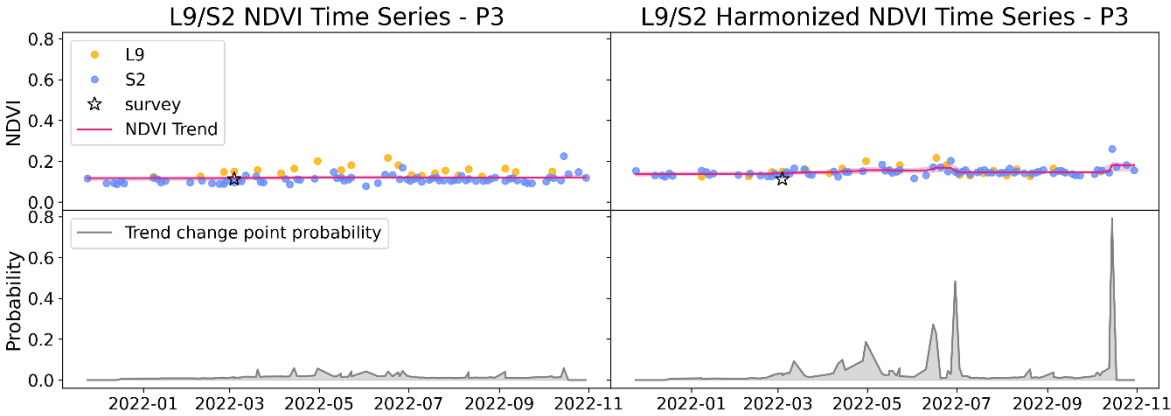


Figure 44 Time series of original (on the left) and harmonized (on the right) L9 and S2 NDVI data with their trend and trend change points estimated with BEAST at P3 (asphalt surface).

Overall, the two presented example highlights that harmonization highly benefit analysis of TS detecting lower-magnitude features, which usually are

more challenging to map (Cohen et al., 2017). By reducing spectral noise, it helps distinguish anomalies along temporal trajectories.

Summarizing, the statistics and preliminary assessment conducted to evaluate the interoperability between Landsat-8 and Sentinel-2 together with the newest Landsat-9 over a localized area were confirmed in the continental scale cross-sensors analysis covering almost one year of observations.

The first remarks to point out is that TOA observations acquired by different instruments at the same time are more similar to each other than their Level-2 products. As discussed above in this chapter and in previous chapters, this is probably due to different atmospheric correction algorithms, estimating atmosphere parameters from different datasets, introducing differences in the measurements. On one hand, atmospheric correction is needed for studies involving images acquired at different time, such as change detection applications, in order to remove changes in the reflectance measurement due to changes in the atmospheric condition instead of actual change in the land surface. On the other hand, it is here demonstrated that atmospheric corrections introduces changes in the observations that might lead to misinterpretation of changes occurred on the ground.

Moreover, among the cross-sensors analysis performed in this study, despite a general consistency of the datasets, higher differences were registered in the Blue, SWIR1 and SWIR2 band. This is due to their sensitivity of these wavelength to water vapour, that is also the reason why they result effective in the monitoring of water content. Indeed, these bands are often used in the computation of index, such as the EVI or NDMI, commonly employed in

vegetation monitoring studies. In such studies, where the improved frequency that the use of these three data sources would allow is highly requested, the use of the presented harmonization coefficients is highly recommended, especially when using index involving SWIR or blue band.

For these reasons, calibration and validation studies are needed, as well as transformation coefficient to harmonize these datasets. In this way, it is possible to perform improved time series analysis of remote sensed data with increased frequency benefitting by these virtual constellation of Landsat/Sentinel data availability, and at the same time reducing errors of algorithm and residual diversity of the datasets.

Conclusion

The presents study addressed the problem of evaluating interoperability of Landsat and Sentinel-2 multispectral datasets for a combined use, to increase the frequency of observation for time series analysis with the purpose of environmental monitoring. In particular, two different studies were conducted, including different datasets and time spans.

The research presented in chapter 4 focused on popular multispectral vegetation index, extensively used in vegetation monitoring studies through time series analysis. In this case, cross-sensors transformation coefficients for NDVI, EVI, SAVI and NDMI computed from Landsat-5 TM, Landsat-7 ETM+, Landsat-8 OLI and Sentinel-2 MSI were computed. The aim was to enable long time series to increase the frequency of data thanks to different sensors harmonization. For each sensor pair, RMA and OLS linear regressions were computed on 300,000 pixels, randomly sampled from couples of almost simultaneous acquisitions by different sensors, and the computations were repeated 100 times to check the repeatability. The adopted methodology moves from the works by Roy et al. (2016) and Chastain et al. (2019), but with several novelties. For the first time a cross-comparison analysis on VIs (NDVI, SAVI, EVI, NDMI) derived from Landsat Collection-2 and Sentinel SR (L2A) products acquired all over the European continent was performed. Furthermore, the study included data from L5, L7, L8 and S2 altogether, allowing the extraction of time series starting from 1984. This approach highly increases the acquisition frequency, combining the 16 days L8 repeat cycle with the 5 days of S2 and thus raising the chance to collect cloud-free images that enables effective vegetation monitoring. This study was able to compute coefficients that allow to create a

consistent TS starting from 1984 to present, combining in a temporal sequence L5, L7, L8 and S2.

In this context, the launch of the new Landsat-9 mission in September 2021 further increases data frequency of observations gathered from the ongoing multispectral moderate resolution missions. In order to quantify the similarity of Landsat-9, Landsat-8 and Sentinel-2 datasets for a combined use, a cross comparison analysis based on the six common bands was performed. The coefficients computed for harmonization of Landsat-8/9 and Sentinel-2/Landsat-9 bands of blue, green, red, NIR, SWIR1 and SWIR2 were presented. Moreover, the preliminary assessment of L9 measurements was supported by spectroradiometer survey campaign on the ground.

In general, a very high consistency between the Landsat-9 and the others ongoing missions was verified. However, some bands appeared more noisy, probably due to residual atmospheric effects and different correction algorithms. A lower consistency was found, as described in Chapter 5, for blue and SWIR bands, especially in the Sentinel-2/Landsat-9 comparison. These bands are those more sensitive to water content. For this reason, these bands are often used for the calculation of multispectral indexes, such as EVI and NDMI, in many effective studies dealing with, for example, humidity or vegetation monitoring. Therefore, although the differences in the red, NIR and green channels are generally smaller than the declared product accuracies and harmonization may be unnecessary, the use of the transformation coefficients is recommended for users who wants to integrate L8/L9/S2 blue or SWIR bands (and their deriver index). In any case, users who intend analysing Landsat and Sentinel data together should firstly estimate the minimum difference in the band reflectance or in the index values that is meaningful for the phenomena

they want to observe. Then, they should consider if the discrepancies due to the radiometric characteristics of the sensors, here discussed, are sensible or not.

In conclusion, the present research assessed the differences between Landsat-9, Landsat-8, Landsat-7, Landsat-5 and Sentinel-2 multispectral data and proposed a set of harmonization coefficients. For the ongoing satellite missions, a very high consistency was found.

The research conducted has produced results that can be directly used in various application areas, and it will in any case be useful for analyses of this type to be updated in the future by taking into consideration the new missions that will be implemented and checking mission consistency over time.

Ringraziamenti

Alla fine di questi anni così formativi ci sono tanti grazie da dire, a tutte le persone che questo percorso mi ha donato e che ho avuto la fortuna di poter conoscere da un punto di vista umano oltre che lavorativo.

Il primo grazie va al Prof. Bitelli, senza il quale, probabilmente, non avrei mai neanche immaginato di intraprendere questo percorso. Grazie Gabriele per tutte le possibilità che mi hai dato, per la fiducia e la libertà di portare avanti e sviluppare le mie idee.

Grazie a Pietro, perché insieme abbiamo pensato e fatto nascere questa ricerca in una bellissima atmosfera di giovialità, condivisione e creatività. Grazie soprattutto per essere stato un amico ancor più di un collega e avermi aiutato ad affrontare anche i giorni peggiori strappandomi sempre un sorriso.

Grazie a Emanuele, per avermi accolta e avermi impegnata quando ne avevo più bisogno. Grazie per donarmi la tua sintesi e le tue parole per dare ordine e concretezza a quello che nella mia mente è spesso caotico.

Grazie Arianna, sapere di poter fare affidamento sul tuo prezioso lavoro e supporto emotivo sono stati fondamentali per portare a termine questo percorso.

Grazie ai “ce la faremo”, Ester, Pietro e Chiara, siete un porto sicuro, siete persone meravigliose e mi offrite sempre prospettive nuove con cui guardare il mondo. Siete così brillanti che penso che, alla fine, in qualche modo, ce la faremo davvero!

Grazie a tutto il gruppo di topografia in cui si respira un'atmosfera speciale. Un ringraziamento particolare a Enrica, compagna di questa avventura, che mi ricorda che non è mai tardi per le “pazzerie” e ad Alessandra. Ale, grazie per la tua professionalità, per la tua generosità nel condividere le tue capacità e conoscenze; ma soprattutto per la tua umanità e capacità di ascolto.

Infine, un ringraziamento alla mia famiglia per avermi sempre assecondata e sostenuta; alle amiche di sempre e a quelle acquisite strada facendo, Cinzia e Laura, che sono diventate dei punti di riferimento indispensabili. Grazie a Fede, per avermi sempre lasciato libera, di andare, provare, anche sbagliare, ma con la consapevolezza di avere sempre un porto sicuro in cui fare ritorno.

Bibliography

- Andréfouët, S., Bindschadler, R., Brown De Colstoun, E.C., Choate, M., Chomentowski, W., Christopherson, J., Doorn, B., Hall, D.K., Holifield, C., Howard, S., Kranenburg, C., Lee, S., Masek, J.B., Moran, M., Mueller-Karger, F., Ohlen, D., Palandro, D., Price, J., Qi, J., Reed, B.C., Samek, J., Scaramuzza, P., Skole, D., Schott, J., Storey, J., Thome, K., Torres-Pulliza, D., Vogelmann, J., Williams, D.L., Woodcock, C., Wylie, B., 2003. Preliminary Assessment of the Value of Landsat 7 ETM+ Data following Scan Line Corrector Malfunction.
- Aschbacher, J., Milagro-Pérez, M.P., 2012a. The European Earth monitoring (GMES) programme: Status and perspectives. *Remote Sens. Environ.* 120, 3–8. <https://doi.org/10.1016/j.rse.2011.08.028>
- Aschbacher, J., Milagro-Pérez, M.P., 2012b. GMES space component: Programmatic status. *Int. Geosci. Remote Sens. Symp.* 1699–1702. <https://doi.org/10.1109/IGARSS.2012.6351197>
- Baetens, L., Desjardins, C., Hagolle, O., 2019. Validation of Copernicus Sentinel-2 Cloud Masks Obtained from MAJA, Sen2Cor, and FMask Processors Using Reference Cloud Masks Generated with a Supervised Active Learning Procedure. *Remote Sens.* 11, 433. <https://doi.org/10.3390/rs11040433>
- Banskota, A., Kayastha, N., Falkowski, M.J., Wulder, M.A., Froese, R.E., White, J.C., 2014. Forest Monitoring Using Landsat Time Series Data: A Review. *Can. J. Remote Sens.* 40, 362–384. <https://doi.org/10.1080/07038992.2014.987376>
- Barsi, J., Lee, K., Kvaran, G., Markham, B., Pedelty, J., 2014. The Spectral Response of the Landsat-8 Operational Land Imager. *Remote Sens.* 6, 10232–10251. <https://doi.org/10.3390/rs61010232>
- Bégué, A., Arvor, D., Bellon, B., Betbeder, J., de Aballeyra, D., Ferraz, R.P.D., Lebourgeois, V., Lelong, C., Simões, M., Verón, S.R., 2018. Remote sensing and cropping practices: A review. *Remote Sens.* 10, 1–32. <https://doi.org/10.3390/rs10010099>
- Berger, M., Aschbacher, J., 2012. Preface: The Sentinel missions-new opportunities for science. *Remote Sens. Environ.* 120, 1–2. <https://doi.org/10.1016/j.rse.2011.12.026>
- Berger, M., Moreno, J., Johannessen, J.A., Levelt, P.F., Hanssen, R.F., 2012. ESA's sentinel missions in support of Earth system science. *Remote Sens. Environ.* 120, 84–90. <https://doi.org/10.1016/j.rse.2011.07.023>

- Brown, C.F., Brumby, S.P., Guzder-Williams, B., Birch, T., Hyde, S.B., Mazzariello, J., Czerwinski, W., Pasquarella, V.J., Haertel, R., Ilyushchenko, S., Schwehr, K., Weisse, M., Stolle, F., Hanson, C., Guinan, O., Moore, R., Tait, A.M., 2022. Dynamic World, Near real-time global 10 m land use land cover mapping. *Sci. Data* 9, 1–17. <https://doi.org/10.1038/s41597-022-01307-4>
- Campbell, J.W., Aarup, T., 1989. Photosynthetically available radiation at high latitudes. *Limnol. Oceanogr.* 34, 1490–1499. <https://doi.org/10.4319/lo.1989.34.8.1490>
- Camps-Valls, G., Tuia, D., Gómez-Chova, L., Jiménez, S., Malo, J., 2012. Remote Sensing Image Processing, Synthesis Lectures on Image, Video, and Multimedia Processing. Springer International Publishing, Cham. <https://doi.org/10.1007/978-3-031-02247-0>
- Canty, M.J., 2019. Image Analysis, Classification, and Detection in Remote Sensing With Algorithms for Python. Cambridge University Press, Cambridge.
- Cao, H., Han, L., Li, L., 2022. Harmonizing surface reflectance between Landsat-7 ETM + , Landsat-8 OLI, and Sentinel-2 MSI over China. *Environ. Sci. Pollut. Res.* 29, 70882–70898. <https://doi.org/10.1007/s11356-022-20771-4>
- Casana, J., Cothren, J., 2013. The CORONA Atlas Project: Orthorectification of CORONA Satellite Imagery and Regional-Scale Archaeological Exploration in the Near East. pp. 33–43. https://doi.org/10.1007/978-1-4614-6074-9_4
- Casu, F., Manunta, M., Agram, P.S., Crippen, R.E., 2017. Big Remotely Sensed Data: tools, applications and experiences. *Remote Sens. Environ.* <https://doi.org/10.1016/j.rse.2017.09.013>
- Chander, G., Markham, B.L., Barsi, J.A., 2007. Revised Landsat-5 Thematic Mapper Radiometric Calibration. *IEEE Geosci. Remote Sens. Lett.* 4, 490–494. <https://doi.org/10.1109/LGRS.2007.898285>
- Chastain, R., Housman, I., Goldstein, J., Finco, M., Tenneson, K., 2019. Empirical cross sensor comparison of Sentinel-2A and 2B MSI, Landsat-8 OLI, and Landsat-7 ETM+ top of atmosphere spectral characteristics over the conterminous United States. *Remote Sens. Environ.* 221, 274–285. <https://doi.org/10.1016/j.rse.2018.11.012>
- Chaves, M.E.D., Picoli, M.C.A., Sanches, I.D., 2020. Recent applications of Landsat 8/OLI and Sentinel-2/MSI for land use and land cover mapping: A systematic review. *Remote Sens.* 12. <https://doi.org/10.3390/rs12183062>

- Chawla, I., Karthikeyan, L., Mishra, A.K., 2020. A review of remote sensing applications for water security: Quantity, quality, and extremes. *J. Hydrol.* 585, 124826. <https://doi.org/10.1016/j.jhydrol.2020.124826>
- Chen, F., Lou, S., Fan, Q., Wang, Chenxing, Claverie, M., Wang, Cheng, Li, J., 2019. Normalized Difference Vegetation Index Continuity of the Landsat 4-5 MSS and TM: Investigations Based on Simulation. *Remote Sens.* 11, 1681. <https://doi.org/10.3390/rs11141681>
- Claverie, M., Ju, J., Masek, J.G., Dungan, J.L., Vermote, E.F., Roger, J.-C., Skakun, S. V., Justice, C., 2018. The Harmonized Landsat and Sentinel-2 surface reflectance data set. *Remote Sens. Environ.* 219, 145–161. <https://doi.org/10.1016/j.rse.2018.09.002>
- Cohen, W. B., Healey, S. P., Yang, Z., Stehman, S. V, Brewer, C. K., Brooks, E. B., Gorelick, N., Huang, C., Hughes, M. J., Kennedy, R. E., Loveland, T. R., Moisen, G. G., & Schroeder, T. A. (2017). How Similar Are Forest Disturbance Maps Derived from Different Landsat Time Series Algorithms? 1–19. <https://doi.org/10.3390/f8040098>
- CSC Mission Management Team, 2018. Sentinel High Level Operations Plan (HLOP) 75.
- Dash, J., Ogutu, B.O., 2016. Recent advances in space-borne optical remote sensing systems for monitoring global terrestrial ecosystems. *Prog. Phys. Geogr.* 40, 322–351. <https://doi.org/10.1177/0309133316639403>
- Delegido, J., Verrelst, J., Alonso, L., Moreno, J., 2011. Evaluation of Sentinel-2 Red-Edge Bands for Empirical Estimation of Green LAI and Chlorophyll Content. *Sensors* 11, 7063–7081. <https://doi.org/10.3390/s110707063>
- Denaro, L.G., Lin, C.-H., 2020. Hybrid Canonical Correlation Analysis and Regression for Radiometric Normalization of Cross-Sensor Satellite Imagery. *IEEE J. Sel. Top. Appl. Earth Obs. Remote Sens.* 13, 976–986. <https://doi.org/10.1109/JSTARS.2020.2971857>
- Drusch, M., Del Bello, U., Carlier, S., Colin, O., Fernandez, V., Gascon, F., Hoersch, B., Isola, C., Laberinti, P., Martimort, P., Meygret, A., Spoto, F., Sy, O., Marchese, F., Bargellini, P., 2012. Sentinel-2: ESA's Optical High-Resolution Mission for GMES Operational Services. *Remote Sens. Environ.* 120, 25–36. <https://doi.org/10.1016/j.rse.2011.11.026>
- Dwyer, J.L., Roy, D.P., Sauer, B., Jenkerson, C.B., Zhang, H.K., Lymburner, L., 2018. Analysis ready data: Enabling analysis of the Landsat archive. *Remote Sens.* 10, 1–19. <https://doi.org/10.3390/rs10091363>

- Ehlers, M., Klonus, S., Tomowski, D., Michel, U., Reinartz, P., 2010. Automated change detection from high-resolution remote sensing images, in: A Special Joint Symposium of ISPRS Technical Commission IV & AutoCarto in Conjunction with ASPRS/CaGIS 2010 Fall Specialty Conference November. Orlando, Florida.
- Elmoataz, A., Lezoray, O., Nouboud, F., Mammass, D. (Eds.), 2008. Image and Signal Processing - 3rd International Conference, ICISP 2008, Cherbourg-Octeville, France, July 1-3, 2008, Proceedings, Lecture Notes in Computer Science. Springer Berlin Heidelberg, Berlin, Heidelberg. <https://doi.org/10.1007/978-3-540-69905-7>
- Emde, C., Buras-Schnell, R., Kylling, A., Mayer, B., Gasteiger, J., Hamann, U., Kylling, J., Richter, B., Pause, C., Dowling, T., Bugliaro, L., 2016. The libRadtran software package for radiative transfer calculations (version 2.0.1). *Geosci. Model Dev.* 9, 1647–1672. <https://doi.org/10.5194/gmd-9-1647-2016>
- ESA, 2015. SENTINEL-2 User Handbook 64. <https://doi.org/GMES-S1OP-EOPG-TN-13-0001>
- ESA - European Space Agency, 2022. Sentinel data product quality report [WWW Document]. URL <https://sentinel.esa.int/web/sentinel/data-product-quality-reports> (accessed 1.20.23).
- ESA - European Space Agency, 2015. Sentinel-2 Processing Baseline [WWW Document]. URL <https://sentinels.copernicus.eu/web/sentinel/technical-guides/sentinel-2-msi/processing-baseline> (accessed 1.20.23).
- Ferrant, S., Selles, A., Le Page, M., Herrault, P.-A., Pelletier, C., Al-Bitar, A., Mermoz, S., Gascoin, S., Bouvet, A., Saqalli, M., Dewandel, B., Caballero, Y., Ahmed, S., Maréchal, J.-C., Kerr, Y., 2017. Detection of Irrigated Crops from Sentinel-1 and Sentinel-2 Data to Estimate Seasonal Groundwater Use in South India. *Remote Sens.* 9. <https://doi.org/10.3390/rs9111119>
- Foga, S., Scaramuzza, P.L., Guo, S., Zhu, Z., Dille, R.D., Beckmann, T., Schmidt, G.L., Dwyer, J.L., Joseph Hughes, M., Laue, B., 2017. Cloud detection algorithm comparison and validation for operational Landsat data products. *Remote Sens. Environ.* 194, 379–390. <https://doi.org/10.1016/j.rse.2017.03.026>
- Gao, B., 1996. NDWI—A normalized difference water index for remote sensing of vegetation liquid water from space. *Remote Sens. Environ.* 58, 257–266. [https://doi.org/https://doi.org/10.1016/S0034-4257\(96\)00067-3](https://doi.org/https://doi.org/10.1016/S0034-4257(96)00067-3)
- Gascon, F., Bouzinac, C., Thépaut, O., Jung, M., Francesconi, B., Louis, J., Lonjou, V., Lafrance, B., Massera, S., Gaudel-Vacaresse, A., Languille, F., Alhammoud, B., Viallefont, F., Pflug, B., Bieniarz, J., Clerc, S., Pessiot, L., Trémas, T., Cadau, E., De Bonis, R., Isola, C., Martimort, P., Fernandez, V., 2017. Copernicus Sentinel-2A

- calibration and products validation status. *Remote Sens.* 9. <https://doi.org/10.3390/rs9060584>
- Ghaderpour, E., Vujadinovic, T., 2020. Change Detection within Remotely Sensed Satellite Image Time Series via Spectral Analysis. *Remote Sens.* 12, 4001. <https://doi.org/10.3390/rs12234001>
- Gómez, C., White, J.C., Wulder, M.A., 2016. Optical remotely sensed time series data for land cover classification: A review. *ISPRS J. Photogramm. Remote Sens.* 116, 55–72. <https://doi.org/10.1016/j.isprsjprs.2016.03.008>
- Gorelick, N., Hancher, M., Dixon, M., Ilyushchenko, S., Thau, D., Moore, R., 2017. Google Earth Engine: Planetary-scale geospatial analysis for everyone. *Remote Sens. Environ.* <https://doi.org/10.1016/j.rse.2017.06.031>
- Gross, G., Helder, D., Begeman, C., Leigh, L., Kaewmanee, M., Shah, R., 2022. Initial Cross-Calibration of Landsat 8 and Landsat 9 Using the Simultaneous Underfly Event. *Remote Sens.* 14. <https://doi.org/10.3390/rs14102418>
- Hammer, E., Ur, J., 2019. Near Eastern Landscapes and Declassified U2 Aerial Imagery. *Adv. Archaeol. Pract.* 7, 107–126. <https://doi.org/10.1017/aap.2018.38>
- Harper, W. V., 2016. Reduced Major Axis Regression, in: *Wiley StatsRef: Statistics Reference Online*. Wiley, pp. 1–6. <https://doi.org/10.1002/9781118445112.stat07912>
- Huang, S., Tang, L., Hupy, J.P., Wang, Y., Shao, G., 2021. A commentary review on the use of normalized difference vegetation index (NDVI) in the era of popular remote sensing. *J. For. Res.* 32, 1–6. <https://doi.org/10.1007/s11676-020-01155-1>
- Huete, A., 1988. A soil-adjusted vegetation index (SAVI). *Remote Sens. Environ.* 25, 295–309. [https://doi.org/10.1016/0034-4257\(88\)90106-X](https://doi.org/10.1016/0034-4257(88)90106-X)
- Huete, A., Didan, K., Miura, T., Rodriguez, E., Gao, X., Ferreira, L., 2002. Overview of the radiometric and biophysical performance of the MODIS vegetation indices. *Remote Sens. Environ.* 83, 195–213. [https://doi.org/10.1016/S0034-4257\(02\)00096-2](https://doi.org/10.1016/S0034-4257(02)00096-2)
- Irons, J.R., Dwyer, J.L., Barsi, J.A., 2012. The next Landsat satellite: The Landsat Data Continuity Mission. *Remote Sens. Environ.* 122, 11–21. <https://doi.org/10.1016/j.rse.2011.08.026>
- Johnson, R.L., Hassett, P.J., 1984. Landsat-5 orbit adjust maneuver report.
- Jutz, S., 2015. Present status of the Copernicus programme. *EGU Gen. Assem.* 2015 17, 14997.

- Jutz, S., Milagro-Pérez, M.P., 2018. Copernicus Program, in: *Comprehensive Remote Sensing*. Elsevier, pp. 150–191. <https://doi.org/10.1016/B978-0-12-409548-9.10317-3>
- Jutz, S.L.G., Milagro-Pérez, M.P., 2016. The copernicus space component: A growing family, in: *Living Planet Symposium 2016, Prague, Czech Republic, 9–13 May 2016*.
- Kaufman, Y.J., Sendra, C., 1988. Algorithm for automatic atmospheric corrections to visible and near-IR satellite imagery. *Int. J. Remote Sens.* 9, 1357–1381. <https://doi.org/10.1080/01431168808954942>
- Koch, A., 2015. COPERNICUS – The European Union Earth Observation Programme - State of play and way ahead, in: *EGU General Assembly 2015*. p. 15742.
- Kondratyev, K., Vassilyev, O., Grigoryev, A., Ivanian, G., 1971. An analysis of the Earth's Resources Satellite (ERTS-1) data. *Remote Sens. Environ.* 2, 273–283. [https://doi.org/10.1016/0034-4257\(71\)90100-3](https://doi.org/10.1016/0034-4257(71)90100-3)
- Kotchenova, S.Y., Vermote, E.F., Matarrese, R., Klemm, Jr., F.J., 2006. Validation of a vector version of the 6S radiative transfer code for atmospheric correction of satellite data Part I: Path radiance. *Appl. Opt.* 45, 6762. <https://doi.org/10.1364/AO.45.006762>
- Kriegler, F.J., Malila, W.A., Nalepka, R.F., Richardson, W., 1969. Preprocessing Transformations and Their Effects on Multispectral Recognition, in: *Remote Sensing of Environment, VI*. p. 97.
- Kruse, F.A., Lefkoff, A.B., Boardman, J.W., Heidebrecht, K.B., Shapiro, A.T., Barloon, P.J., Goetz, A.F.H., 1993. The spectral image processing system (SIPS)-interactive visualization and analysis of imaging spectrometer data, in: *AIP Conference Proceedings*. AIP, pp. 192–201. <https://doi.org/10.1063/1.44433>
- Kuenzer, C., Dech, S., Wagner, W., 2015. *Remote Sensing Time Series, Remote Sensing and Digital Image Processing*.
- Lauer, D.T., Morain, S.A., Salomonson, V. V., 1997. The landsat program: Its origins, evolution, and impacts. *Photogramm. Eng. Remote Sensing* 63, 831–838.
- Li, J., Chen, B., 2020. Global revisit interval analysis of landsat-8-9 and sentinel-2a-2b data for terrestrial monitoring. *Sensors* 20, 1–15. <https://doi.org/10.3390/s20226631>
- Li, J., Roy, D.P., 2017. A global analysis of Sentinel-2a, Sentinel-2b and Landsat-8 data revisit intervals and implications for terrestrial monitoring. *Remote Sens.* 9. <https://doi.org/10.3390/rs9090902>

- Li, P., Jiang, L., Feng, Z., 2013. Cross-Comparison of Vegetation Indices Derived from Landsat-7 Enhanced Thematic Mapper Plus (ETM+) and Landsat-8 Operational Land Imager (OLI) Sensors. *Remote Sens.* 6, 310–329. <https://doi.org/10.3390/rs6010310>
- Li, S., Ganguly, S., Dungan, J.L., Wang, W., Nemani, R.R., 2017. Sentinel-2 MSI Radiometric Characterization and Cross-Calibration with Landsat-8 OLI. *Adv. Remote Sens.* 06, 147–159. <https://doi.org/10.4236/ars.2017.62011>
- Liu, L., Xiao, X., Qin, Y., Wang, J., Xu, X., Hu, Y., Qiao, Z., 2020. Mapping cropping intensity in China using time series Landsat and Sentinel-2 images and Google Earth Engine. *Remote Sens. Environ.* 239, 111624. <https://doi.org/10.1016/J.RSE.2019.111624>
- Louis, J., 2016. Sentinel 2 MSI - Level 2A Product Definition. Eur. Sp. Agency, (Special Publ. ESA SP 49).
- Louis, J., Charantonis, A., Berthelot, B., Lacoste-Francis, H., 2010. Cloud Detection for Sentinel-2, in: *Living Planet Symposium Proceedings*. ESA Communications,, Noordwijk, p. 499.
- Loveland, T.R., Dwyer, J.L., 2012. Landsat: Building a strong future. *Remote Sens. Environ.* 122, 22–29. <https://doi.org/10.1016/j.rse.2011.09.022>
- Loveland, T.R., Irons, J.R., 2016. Landsat 8: The plans, the reality, and the legacy. *Remote Sens. Environ.* 185, 1–6. <https://doi.org/10.1016/j.rse.2016.07.033>
- Lymburner, L., Botha, E., Hestir, E., Anstee, J., Sagar, S., Dekker, A., Malthus, T., 2016. Landsat 8: Providing continuity and increased precision for measuring multi-decadal time series of total suspended matter. *Remote Sens. Environ.* 185, 108–118. <https://doi.org/10.1016/j.rse.2016.04.011>
- Main-Knorn, M., Pflug, B., Louis, J., Debaecker, V., Müller-Wilm, U., Gascon, F., 2017. Sen2Cor for Sentinel-2, in: Bruzzone, L., Bovolo, F., Benediktsson, J.A. (Eds.), *Image and Signal Processing for Remote Sensing XXIII*. SPIE, p. 3. <https://doi.org/10.1117/12.2278218>
- Malenovský, Z., Rott, H., Cihlar, J., Schaepman, M.E., García-Santos, G., Fernandes, R., Berger, M., 2012. Sentinels for science: Potential of Sentinel-1, -2, and -3 missions for scientific observations of ocean, cryosphere, and land. *Remote Sens. Environ.* 120, 91–101. <https://doi.org/10.1016/j.rse.2011.09.026>
- Mancino, G., Ferrara, A., Padula, A., Nolè, A., 2020. Cross-Comparison between Landsat 8 (OLI) and Landsat 7 (ETM+) Derived Vegetation Indices in a

- Mediterranean Environment. Remote Sens. 12, 291.
<https://doi.org/10.3390/rs12020291>
- Mandanici, E., Bitelli, G., 2016. Preliminary Comparison of Sentinel-2 and Landsat 8 Imagery for a Combined Use. Remote Sens. 8, 1014.
<https://doi.org/10.3390/rs8121014>
- Markham, B., McCorkel, J., Montanaro, M., Morland, E., Pearlman, A., Pedelty, J., Wenny, B., Barsi, J., Donley, E., Efremova, B., Hair, J., Jenstrom, D., Kaita, E., Knight, E., Kvaran, G., 2019. Landsat 9: Mission Status and Prelaunch Instrument Performance Characterization and Calibration, in: IGARSS 2019 - 2019 IEEE International Geoscience and Remote Sensing Symposium. IEEE, pp. 5788–5791.
<https://doi.org/10.1109/IGARSS.2019.8898362>
- Mas, J.-F., 1999. Monitoring land-cover changes: A comparison of change detection techniques. Int. J. Remote Sens. 20, 139–152.
<https://doi.org/10.1080/014311699213659>
- Masek, J.G., Vermote, E.F., Saleous, N.E., Wolfe, R., Hall, F.G., Huemmrich, K.F., Gao, F., Kutler, J., Lim, T., 2006. A Landsat Surface Reflectance Dataset for North America, 1990–2000. IEEE Geosci. Remote Sens. Lett. 3, 68–72.
- Masek, J.G., Wulder, M.A., Markham, B., McCorkel, J., Crawford, C.J., Storey, J., Jenstrom, D.T., 2020. Landsat 9: Empowering open science and applications through continuity. Remote Sens. Environ. 248, 111968.
<https://doi.org/10.1016/j.rse.2020.111968>
- Mayer, B., Kylling, A., 2005. Technical note: The libRadtran software package for radiative transfer calculations - description and examples of use. Atmos. Chem. Phys. 5, 1855–1877. <https://doi.org/10.5194/acp-5-1855-2005>
- McDonald, R.A., 1995. Corona: Success for space reconnaissance, a look into the Cold War, and a revolution for intelligence. Photogramm. Eng. Remote Sens. LCI.
- Nagy, A., Szabó, A., Adeniyi, O.D., Tamás, J., 2021. Wheat Yield Forecasting for the Tisza River Catchment Using Landsat 8 NDVI and SAVI Time Series and Reported Crop Statistics. Agronomy 11, 652. <https://doi.org/10.3390/agronomy11040652>
- NASA, 2023. Landsat science [WWW Document]. URL <https://landsat.gsfc.nasa.gov/> (accessed 1.20.23).
- National Oceanic and Atmospheric Administration (NOAA), 1995a. Landsat 6 failure attributed to ruptured manifold.
- National Oceanic and Atmospheric Administration (NOAA), 1995b. Landsat 6 failure investigation final report summary.

- Pecora, W.T., 1972. Remote Sensing of Earth Resources: Users, Prospects and Plans, NASA's Long-Range Earth Resources Survey Program, Thirteenth Meeting, Panel on Science and Technology, in: Panel on Science and Technology, Committee on Science and Astronautics, U.S. House of Representatives, 25 January. U.S. Government Printing Office, Washington, D.C., p. 8.
- Phiri, D., Simwanda, M., Salekin, S., Nyirenda, V., Murayama, Y., Ranagalage, M., 2020. Sentinel-2 Data for Land Cover/Use Mapping: A Review. *Remote Sens.* 12, 2291. <https://doi.org/10.3390/rs12142291>
- Poursanidis, D., Chrysoulakis, N., 2017. Remote Sensing, natural hazards and the contribution of ESA Sentinels missions. *Remote Sens. Appl. Soc. Environ.* 6, 25–38. <https://doi.org/10.1016/j.rsase.2017.02.001>
- Qiu, S., Zhu, Z., Shang, R., Crawford, C.J., 2021. Can Landsat 7 preserve its science capability with a drifting orbit? *Sci. Remote Sens.* 4, 100026. <https://doi.org/10.1016/j.srs.2021.100026>
- Richards, J.A., 2022. Remote Sensing Digital Image Analysis. Springer International Publishing, Cham. <https://doi.org/10.1007/978-3-030-82327-6>
- Roitberg, E., Malgeac, I., Weil-Zattelman, S., Kizel, F., 2022. BRDF laboratory measurements using a camera-aided spectroradiometer. *Int. Arch. Photogramm. Remote Sens. Spat. Inf. Sci.* XLIII-B3-2, 417–422. <https://doi.org/10.5194/isprs-archives-XLIII-B3-2022-417-2022>
- Roy, D.P., Kovalskyy, V., Zhang, H.K., Vermote, E.F., Yan, L., Kumar, S.S., Egorov, A., 2016. Characterization of Landsat-7 to Landsat-8 reflective wavelength and normalized difference vegetation index continuity. *Remote Sens. Environ.* 185, 57–70. <https://doi.org/10.1016/j.rse.2015.12.024>
- Roy, D.P., Li, Z., Zhang, H.K., Huang, H., 2020. A conterminous United States analysis of the impact of Landsat 5 orbit drift on the temporal consistency of Landsat 5 Thematic Mapper data. *Remote Sens. Environ.* 240, 111701. <https://doi.org/10.1016/j.rse.2020.111701>
- Roy, D.P., Wulder, M.A., Loveland, T.R., C.E., W., Allen, R.G., Anderson, M.C., Helder, D., Irons, J.R., Johnson, D.M., Kennedy, R., Scambos, T.A., Schaaf, C.B., Schott, J.R., Sheng, Y., Vermote, E.F., Belward, A.S., Bindschadler, R., Cohen, W.B., Gao, F., Hipple, J.D., Hostert, P., Huntington, J., Justice, C.O., Kilic, A., Kovalskyy, V., Lee, Z.P., Lymburner, L., Masek, J.G., McCorkel, J., Shuai, Y., Trezza, R., Vogelmann, J., Wynne, R.H., Zhu, Z., 2014. Landsat-8: Science and product vision for terrestrial global change research. *Remote Sens. Environ.* 145, 154–172. <https://doi.org/10.1016/j.rse.2014.02.001>

- Roy, D.P., Yan, L., 2020. Robust Landsat-based crop time series modelling. *Remote Sens. Environ.* 238, 110810. <https://doi.org/10.1016/j.rse.2018.06.038>
- Schläpfer, D., Borel, C.C., Keller, J., Itten, K.I., 1998. Atmospheric Precorrected Differential Absorption Technique to Retrieve Columnar Water Vapor. *Remote Sens. Environ.* 65, 353–366. [https://doi.org/10.1016/S0034-4257\(98\)00044-3](https://doi.org/10.1016/S0034-4257(98)00044-3)
- Schott, J.R., Gerace, A., Woodcock, C.E., Wang, S., Zhu, Z., Wynne, R.H., Blinn, C.E., 2016. The impact of improved signal-to-noise ratios on algorithm performance: Case studies for Landsat class instruments. *Remote Sens. Environ.* 185, 37–45. <https://doi.org/10.1016/j.rse.2016.04.015>
- Simonett, D.S., 1969. Editor's preface. *Remote Sens. Environ.* 1, v. [https://doi.org/10.1016/S0034-4257\(69\)90011-X](https://doi.org/10.1016/S0034-4257(69)90011-X)
- Singh, A., 1989. Review Article Digital change detection techniques using remotely-sensed data. *Int. J. Remote Sens.* 10, 989–1003. <https://doi.org/10.1080/01431168908903939>
- Spectra Vista Corporation - SVC, 2019. Field Spectroscopy Guide with SVC i-series Spectroradiometers.
- Teixeira Pinto, C., Jing, X., Leigh, L., 2020. Evaluation Analysis of Landsat Level-1 and Level-2 Data Products Using In Situ Measurements. *Remote Sens.* 12, 2597. <https://doi.org/10.3390/rs12162597>
- The European parliament, The European council, 2021. REGULATION (EU) 2021/696 OF THE EUROPEAN PARLIAMENT AND OF THE COUNCIL of 28 April 2021, Communities.
- The European parliament, The European council, 2014. Regulation (EU) 377/2014 establishing the Copernicus Programme and repealing Regulation (EU) No 911/2010.
- The White House - National Science and Technology Council, 1996. National space policy (Fact sheet).
- Thuillier, G., Hersé, M., Labs, D., Foujols, T., Peetermans, W., Gillotay, D., Simon, P.C., Mandel, H., 2003. The Solar Spectral Irradiance from 200 to 2400 nm as Measured by the SOLSPEC Spectrometer from the Atlas and Eureka Missions. *Sol. Phys.* 214, 1–22. <https://doi.org/10.1023/A:1024048429145>
- Tomowski, D., Klonus, S., Ehlers, M., Michel, U., Reinartz, P., 2010. Change Visualization through a Texture-Based Analysis Approach for Disaster Applications. *ISPRS Proc.* 1–6.

- Toulemont, A., Oliver, M., Clerc, S., Bellouard, R., Reina, F., Gascon, F., Luce, J.-F., Mavrocordatos, C., Boccia, V., 2021. Copernicus Sentinel-2C/D Multi Spectral Instrument full field of view spectral characterization, in: Neeck, S.P., Kimura, T., Babu, S.R., Hélière, A. (Eds.), *Sensors, Systems, and Next-Generation Satellites XXV*. SPIE, p. 26. <https://doi.org/10.1117/12.2593729>
- Tsatsaris, A., Kalogeropoulos, K., Stathopoulos, N., Louka, P., Tsanakas, K., Tsesmelis, D.E., Krassanakis, V., Petropoulos, G.P., Pappas, V., Chalkias, C., 2021. Geoinformation technologies in support of environmental hazards monitoring under climate change: An extensive review. *ISPRS Int. J. Geo-Information* 10. <https://doi.org/10.3390/ijgi10020094>
- U.S. Geological Survey, 2022a. Landsat 9 Data Users Handbook.
- U.S. Geological Survey, 2022b. Landsat 8-9 Level 2 Science Product (L2SP) (Guide v. 4.0).
- U.S. Geological Survey, 2021a. Landsat Collection 2 (ver. 1.1, January 15, 2021): U.S. Geological Survey Fact Sheet 2021–3002. <https://doi.org/10.3133/fs20213002>
- U.S. Geological Survey, 2021b. Landsat collection 2, Fact Sheet. Reston, VA. <https://doi.org/10.3133/fs20213002>
- U.S. Geological Survey, 2021c. Landsat Surface Reflectance-derived Spectral Indices [WWW Document]. URL <https://www.usgs.gov/landsat-missions/landsat-surface-reflectance-derived-spectral-indices>
- U.S. Geological Survey, 2021d. Landsat missions [WWW Document]. URL <https://www.usgs.gov/landsat-missions/>
- U.S. Geological Survey, 2019a. Landsat 7 Data Users Handbook.
- U.S. Geological Survey, 2019b. Landsat 8 Data Users Handbook.
- Vermote, E., Justice, C., Claverie, M., Franch, B., 2016a. Preliminary analysis of the performance of the Landsat 8/OLI land surface reflectance product. *Remote Sens. Environ.* 185, 46–56. <https://doi.org/10.1016/j.rse.2016.04.008>
- Vermote, E., Justice, C., Claverie, M., Franch, B., 2016b. Preliminary analysis of the performance of the Landsat 8/OLI land surface reflectance product. *Remote Sens. Environ.* 185, 46–56. <https://doi.org/10.1016/j.rse.2016.04.008>
- Vermote, E.F., Tanré, D., Deuzé, J.L., Herman, M., Morcrette, J.J., 1997. Second simulation of the satellite signal in the solar spectrum, 6s: an overview. *IEEE Trans. Geosci. Remote Sens.* 35, 675–686. <https://doi.org/10.1109/36.581987>

- Waldrop, M.M., 1982. Imaging the Earth (I): The Troubled First Decade of Landsat. *Science* (80-.). 215, 1600–1603. <https://doi.org/10.1126/science.215.4540.1600>
- Wang, C., Li, J., Liu, Q., Zhong, B., Wu, S., Xia, C., 2017. Analysis of Differences in Phenology Extracted from the Enhanced Vegetation Index and the Leaf Area Index. *Sensors* 17, 1982. <https://doi.org/10.3390/s17091982>
- West, H., Quinn, N., Horswell, M., 2019. Remote sensing for drought monitoring & impact assessment: Progress, past challenges and future opportunities. *Remote Sens. Environ.* 232, 111291. <https://doi.org/10.1016/j.rse.2019.111291>
- Woodcock, C.E., Allen, R., Anderson, M., Belward, A., Bindschadler, R., Cohen, W., Gao, F., Goward, S.N., Helder, D., Helmer, E., Nemani, R., Oreopoulos, L., Schott, J., Thenkabail, P.S., Vermote, E.F., Vogelmann, J., Wulder, M.A., Wynne, R., 2008. Free Access to Landsat Imagery. *Science* (80-.). 320, 1011–1011. <https://doi.org/10.1126/science.320.5879.1011a>
- Wu, Z., Snyder, G., Vadnais, C., Arora, R., Babcock, M., Stensaas, G., Doucette, P., Newman, T., 2019. User needs for future Landsat missions. *Remote Sens. Environ.* 231, 111214. <https://doi.org/10.1016/j.rse.2019.111214>
- Wulder, M.A., Loveland, T.R., Roy, D.P., Crawford, C.J., Masek, J.G., Woodcock, C.E., Allen, R.G., Anderson, M.C., Belward, A.S., Cohen, W.B., Dwyer, J., Erb, A., Gao, F., Griffiths, P., Helder, D., Hermosilla, T., Hipple, J.D., Hostert, P., Hughes, M.J., Huntington, J., Johnson, D.M., Kennedy, R., Kilic, A., Li, Z., Lymburner, L., McCorkel, J., Pahlevan, N., Scambos, T.A., Schaaf, C., Schott, J.R., Sheng, Y., Storey, J., Vermote, E., Vogelmann, J., White, J.C., Wynne, R.H., Zhu, Z., 2019. Current status of Landsat program, science, and applications. *Remote Sens. Environ.* 225, 127–147. <https://doi.org/10.1016/j.rse.2019.02.015>
- Wulder, M.A., Roy, D.P., Radeloff, V.C., Loveland, T.R., Anderson, M.C., Johnson, D.M., Healey, S., Zhu, Z., Scambos, T.A., Pahlevan, N., Hansen, M., Gorelick, N., Crawford, C.J., Masek, J.G., Hermosilla, T., White, J.C., Belward, A.S., Schaaf, C., Woodcock, C.E., Huntington, J.L., Lymburner, L., Hostert, P., Gao, F., Lyapustin, A., Pekel, J.F., Strobl, P., Cook, B.D., 2022. Fifty years of Landsat science and impacts. *Remote Sens. Environ.* 280, 113195. <https://doi.org/10.1016/j.rse.2022.113195>
- Xie, S., Sun, L., Liu, L., Liu, X., 2022. Global Cross-Sensor Transformation Functions for Landsat-8 and Sentinel-2 Top of Atmosphere and Surface Reflectance Products Within Google Earth Engine. *IEEE Trans. Geosci. Remote Sens.* 60, 1–9. <https://doi.org/10.1109/TGRS.2022.3170338>
- Xue, J., Su, B., 2017. Significant Remote Sensing Vegetation Indices : A Review of Developments and Applications 2017.

- Xue, Z., Du, P., Feng, L., 2014. Phenology-Driven Land Cover Classification and Trend Analysis Based on Long-term Remote Sensing Image Series. *IEEE J. Sel. Top. Appl. Earth Obs. Remote Sens.* 7, 1142–1156. <https://doi.org/10.1109/JSTARS.2013.2294956>
- Yao, X., Li, G., Xia, J., Ben, J., Cao, Q., Zhao, L., Ma, Y., Zhang, L., Zhu, D., 2019. Enabling the Big Earth Observation Data via Cloud Computing and DGGS: Opportunities and Challenges. *Remote Sens.* 12, 62. <https://doi.org/10.3390/rs12010062>
- Zeng, L., Wardlow, B.D., Xiang, D., Hu, S., Li, D., 2020. A review of vegetation phenological metrics extraction using time-series, multispectral satellite data. *Remote Sens. Environ.* 237, 111511. <https://doi.org/10.1016/j.rse.2019.111511>
- Zhang, H.K., Roy, D.P., 2016. Landsat 5 Thematic Mapper reflectance and NDVI 27-year time series inconsistencies due to satellite orbit change. *Remote Sens. Environ.* 186, 217–233. <https://doi.org/10.1016/j.rse.2016.08.022>
- Zhao, K., Wulder, M. A., Hu, T., Bright, R., Wu, Q., Qin, H., Li, Y., Toman, E., Mallick, B., Zhang, X., & Brown, M. (2019). Detecting change-point, trend, and seasonality in satellite time series data to track abrupt changes and nonlinear dynamics: A Bayesian ensemble algorithm. *Remote Sensing of Environment*, 232, 111181. <https://doi.org/10.1016/j.rse.2019.04.034>
- Zhong, L., Hu, L., Zhou, H., 2019. Deep learning based multi-temporal crop classification. *Remote Sens. Environ.* 221, 430–443. <https://doi.org/10.1016/j.rse.2018.11.032>
- Zhu, Z., 2017. Change detection using landsat time series: A review of frequencies, preprocessing, algorithms, and applications. *ISPRS J. Photogramm. Remote Sens.* 130, 370–384. <https://doi.org/10.1016/j.isprsjprs.2017.06.013>
- Zhu, Z., Woodcock, C.E., 2012. Object-based cloud and cloud shadow detection in Landsat imagery. *Remote Sens. Environ.* 118, 83–94. <https://doi.org/https://doi.org/10.1016/j.rse.2011.10.028>